NUREG/CR-1183

Laboratory Simulation of Steady Tornadic Wind Loads on Structures

Prepared by M. C. Jischke, B. D. Light

University of Oklahoma

1746 001

Prepared for
U. S. Nuclear Regulatory
Commission

Available from

GPO Sales Program
Division of Technical Information and Document Control
U. S. Nuclear Regulatory Commission
Washington, D. C. 20555

and

National Technical Information Service
Springfield, Virginia 22161

NUREG/CR-1183
RB, R6

Laboratory Simulation of Steady Tornadic Wind Loads on Structures

Manuscript Completed: November 1979
Date Published: December 1979

Prepared by
M. C. Jischke, B. D. Light

School of Aerospace, Mechanical and Nuclear Engineering
University of Oklahoma

Prepared for
Division of Reactor Safety Research
Office of Nuclear Regulatory Research
U.S. Nuclear Regulatory Commission
Washington, D.C. 20555
NRC FIN No. B6241
NRC-04-78-207

PREFACE

This investigation was sponsored by the United States Nuclear Regulatory Commission under Contract No. NRC-04-78-207. This work was conducted by Professor Martin C. Jischke and Bruce D. Light; School of Aerospace, Mechanical and Nuclear Engineering, University of Oklahoma; Norman, Oklahoma 73019. Dr. Robert Abbey, NRC, served as the cognizant program monitor.

This report is taken, in part, from the thesis of Bruce D. Light, "Laboratory Simulation of Tornadic Wind Loads on Structures", submitted to the University of Oklahoma.

Martin C. Jischke

Martin C. Jischke
Principal Investigator
October 15, 1979

1746 004

ABSTRACT

Ward's tornado simulator has been modified to study the interaction of tornadic flowfields with structures. Measurements with and without swirl have been made of the pressure on the surface of a cylindrical model and a rectangular model placed in the simulator. The cylindrical model, intended to represent the containment building of a nuclear reactor, is a circular cylinder 17.1 cm high and 11.4 cm in diameter with a hemispherical roof. The rectangular model, intended to represent the turbine building of a nuclear power plant, is a rectangular prism 12.7 cm high with a planform 14.6 cm by 25.4 cm.

Results are presented for the surface pressure coefficient and the total force and moments coefficients for imposed swirl angles of 0° and 45°, with the models placed at three locations within the simulator: 1) the convergent zone, 2) the boundary of the convergent zone and convection zone, 3) the convection zone.

The measurements on the cylindrical model show that in the swirling flow case, the nonuniform flow due to the tornado-like vortex induces a side-force, reckoned with respect to the local wind direction, that increases as the distance between the model and vortex decreases. The magnitude of the force coefficient on the structure increases with swirl, especially as the vortex and model come closer together. The horizontal force coefficient has a value of 1.01 or less under all conditions. The overturning moment coefficient on the model increases with swirl, the maximum value being 0.45 when the model is in the convergent zone. These measurements show that in the convergent zone and outer part of the convection zone, the pressure

1746 005

distribution on the model would tend to cause a structure of this shape to failure by overturning. When the model's inner edge is tangent to the undisturbed position of the vortex, the vortex attaches itself to the model and the pressure coefficient on the model has a more symmetric distribution around the model and has a relatively large negative values. Typical values of the pressure coefficient on the cylindrical portion of the model are as low as -2.78. Because of this high suction pressure force, another mode of failure, referred to as the bursting mode, becomes possible when the vortex attaches itself to the structure.

The data for the rectangular model shows that the effects of the imposed swirl can be dramatic and important. Increases in the horizontal force coefficient and overturning moment coefficient by a factor of four over the zero swirl valuescan occur when the model is at the boundary of the convergent and convection zones. The vertical force on the roof can more than double. In addition, extremely high suction pressure forces can occur locally on the structure. Thus, in addition to the possibility of failure by overturning, the structure can fail by a sequence which involves a local bursting due to the high suction force that then allows the high tornadic winds to tear away major parts of the structure.

These results show that the tornadic wind loads on structures cannot always be accurately estimated from the loads caused by boundary-layer-type winds.

TABLE OF CONTENTS

1746 007

LIST OF TABLES

1746 009

1746 010

LIST OF ILLUSTRATIONS

Figure		Page

1746 013

Figure		Page

NOMENCLATURE

a	cylinder radius
A	reference area
$\vec{C}_f$	force coefficient
$\vec{C}_M$	moment coefficient
C_p	pressure coefficient
d	cylinder diameter
f	force per unit length
$\vec{F}$	force
h	height of convergent zone
l	total height of cylindrical or rectangular model
L	length scale
$\vec{M}$	moment
$\hat{n}$	outward unit normal
p	pressure
q	volumetric flow rate per unit length
Q	volumetric flow rate
r,η,z	cylindrical polar coordinates
u,v	velocity components in r,η directions, respectively
V	velocity
W	complex potential
x,y,z	cartesian coordinates
z_r	roughness height

Greek Letters

α	inverse of exponent in power law variation of velocity with height

γ,Γ	circulation
ζ	complex variable
θ	model orientation angle
ν	kinematic viscosity
ρ	density
$\overset{=}{\tau}$	viscous stress tensor
ϕ	imposed swirl angle
Φ	velocity potential
Ψ	streamfunction

Subscripts

c	core
max	maximum vlaue
model	model value
o	evaluated at $\zeta_o = r_o e^{i\eta_o}$
ref	reference value
s	screen
u	updraft radius

1746 016

LABORATORY SIMULATION OF STEADY TORNADIC WIND LOADS ON STRUCTURES

INTRODUCTION

Motivation

A growing concern for structural efficiency and safety has led engineers and architects to devote increasing attention to the interaction of the wind with structures. The resulting study of wind engineering includes the disciplines of fluid dynamics, meteorology, aerodynamics, and structural mechanics and is becoming an increasingly important part of the design of vital structures. Structures housing nuclear reactors, for example, must be able to withstand the forces of the most extreme wind conditions and be impervious to the impact of wind-generated missiles.

The preponderance of research in this growing field of wind engineering has been focused on the interaction of ordinary boundary-layer-type winds with structures. Limited measurements on full-scale systems in the field [see e.g. 1,2] along with more extensive measurements on scaled models in meteorological wind tunnels [see e.g. 3,4] provide most of the reliable data in wind engineering. While many problems remain, particularly in the development of analytical methods for calculating wind loads on realistic structure much progress has been made in understanding the effects of boundary-layer-type winds and their interaction with structures.

However, examination of the range of possible wind conditions that occur in the atmosphere quickly leads one to conclude that the most extreme wind conditions are those associated with tornadoes [5]. Indeed tornadic wind speeds approaching 400 kph have been reported in the literature [6].

In contrast to the usual boundary-layer-type flows where the ambient vorticity is largely horizontal, tornadic winds contain significant vertical as well as horizontal vorticity and thereby exhibit a greater complexity and richness. In spite of their importance, little information is available on the interaction of tornadic flows with structures. Estimates of tornadic wind loads are usually derived from boundary-layer-type wind results, completely ignoring the vortical nature of tornadic flows.

Earlier Work

Much of the existing information on naturally occurring tornadoes is derived from meteorological field data and laboratory simulations in which the focus of interest is on the tornado and the tornado-spawning storm system rather than the interaction of the tornado with structures. Except for the data given by Hoecker [7,8] on the 1957 Dallas tornado--which we shall discuss in more detail in Chapter II--the meteorological data available is either of a qualitative nature or is on a scale that does not resolve the structure of the tornadic windfield. Typical of the former are photographs of the funnel and clouds accompanying the tornado-generating parent storm system [9] and narratives by observers [10] while the latter includes rawinsonde data or radar-derived circulation for the parent storm system [11]. These data make clear that many tornadoes result from the low-level convergence of ambient circulations as a consequence of atmospheric instabilities. Other mechanisms for converging ambient vorticity surely exist, although supporting data for them is scarce. In addition, the details of the early stages of tornado genesis and the final stages of tornado decay remain enigmatic.

The apparent randomness of tornado occurrence in time and space as well as the difficulty and danger associated with field measurements of tornadic winds have led several investigators to attempt laboratory simulations [12,13]. These simulations have improved our understanding of the nature of tornadic windfields and many of the observed features of naturally-occurring tornadoes. A discussion of the laboratory simulation of tornadoes will be covered in more detail in Chapter II.

Except for the work of Chang [14], the study of tornadic wind loads on structures has involved field observations of structures that have been damaged by tornadoes [15]. By estimating the wind loads required to cause the observed damage, one can infer the magnitude of the windspeeds that accompany tornadoes and also determine mechanisms for structural failure [16]. These analyses suggest windspeeds from 190 kph to 350 kph and imply that most buildings are destroyed as a consequence of the large dynamic pressure forces that accompany the high tornadic windspeeds rather than the internal overpressure due to the rapid decrease in the ambient pressure that occurs with tornadoes. The limitations of these damage surveys are well known. Uncertainity results from the assumptions that must be made about the structural integrity of a building before it was damaged. Also, the damage sequence must be inferred from the remaining debris. While providing valuable information on tornadic winds, damage surveys are too uncertain to be used to determine tornadic wind loads on vital structures.

Chang [14] has measured the surface pressure forces on a cubical model in a laboratory simulation in which the model was rotated about a vortex in order to simulate the relative motion between the structure and the tornado. As the relative motion between tornadoes and structures is a translational one and not rotational, tne utility of these results is unclear. Also, as we shall discuss in Chapter II, the simulator used in Chang's work does not capture as many of the features of naturally-occurring tornadoes as does the simulator used in the present study.

These brief remarks suggest that the interaction of tornadoes and structures requires further investigation. Systematic studies of the effects of a structure's shape and location must be conducted if our understanding of this aspect of wind engineering is to grow.

The Present Study

This report describes laboratory measurements of the steady wind loads on model structures in the vicinity of a tornado-like vortex. Two different models have been used. One is a circular cylinder with a hemispherical dome roof and is intended to model a typical containment building for a nuclear reactor. The second model is a rectangular prism that models a typical turbine building in a nuclear power plant.

The chapters that follow discuss tornado characteristics and their laboratory simulation, the scaling analysis that was used to design the experiments, the results for the cylindrical model, the results for the rectangular model, and ends with some remarks on the implications of these measurements.

CHAPTER II

TORNADO CHARACTERISTICS AND THEIR LABORATORY SIMULATION

Tornado Characteristics

Tornadoes represent the most violent of nature's small-scale vortices. The lower portions of tornadoes are nearly always visible as funnels pendant from cumulonimbus clouds or occasionally from shallow cloud shelves or flanking lines of cumuli which are extensions of thunderstorm cloud systems [17,18]. Although the flow within the parent cloud is obscured, recent doppler radar data [11] suggests the typical tornado vortex has a vertical extent which is considerably larger than the visible funnel, extending perhaps to the tropopause (about 15 km in midlatitudes), and has a radial extent (e.g. radius of maximum winds) of a fraction of a kilometer. This narrow core of concentrated vorticity exists within an extended background of weaker ambient vorticity. It is likely that the tornado vortex draws upon the vorticity of the larger region (15 to 25 km in radius) for its angular momentum and concentrated vorticity. Reliable estimates of the maximum windspeed in tornadoes do not exceed 400 kph, although unsubstantiated claims of windspeeds in excess of 800 kph can be found. The pressure drop associated with 400 kph winds is approximately 1.2×10^6 N/m^2 and roughly suggests the magnitude of the wind loadings tornadoes place on structures.

Tornado occurrence in the atmosphere requires an ambient source of vorticity and a mechanism to concentrate the associated angular momentum. The vorticity source is believed to be mesoscale circulation of the parent storm system. These storms are thought to derive their circulation from the rotation of the earth implying most of the tornadoes they spawn should be cyclonic. However, there are enough examples of anticyclonic tornadoes to indicate that the earth's rotation is not always the source of the tornado's circulation. The mechanism by which the vorticity is concentrated appears to be the intense, low-level convergence accompanying a strong conditional convective instability that has gone unstable.

The life cycle of tornadoes is usually divided into three distinct stages: genesis, mature stage, and decay -- the latter being the least well understood. Typical tornado lifetimes are a quarter to a half of an hour although examples of tornadoes and tornado-spawning storm systems lasting several hours can be cited. Translational velocities of tornadoes are of the order of 40 kph with some cases up to 125 kph. Damage paths range from a few tens of meters wide and a half kilometer long to such extremes as two kilometers wide and 500 kilometers long (see e.g. ref. 19).

The maximum winds and damage appear to occur during the mature stage of the life cycle. Thus, it is this mature stage that is to be simulated in the laboratory. A schematic sketch of the structure of a mature stage tornado is given in Figure 1 along with estimates of the dimensions of a worst case intense tornado of the Midwest variety. The sketch has been exaggerated for clarity and is not to scale.

The rapidly swirling region is in rough cyclostrophic balance and probabl extends to the tropopause. The winds in this region are primarily aximuthal and vary as r^{-n} $(1/2 \leq n \leq 1)$ with radius r. The updraft region is a region of swirling ascending flow in which air from the surface inflow layer rises, eventually spreading horizontally near a neutrally, stable layer such as the tropopause. Although the net mass flux is upward in this region, the most intense tornadoes show evidence of a downflow along the axis of the

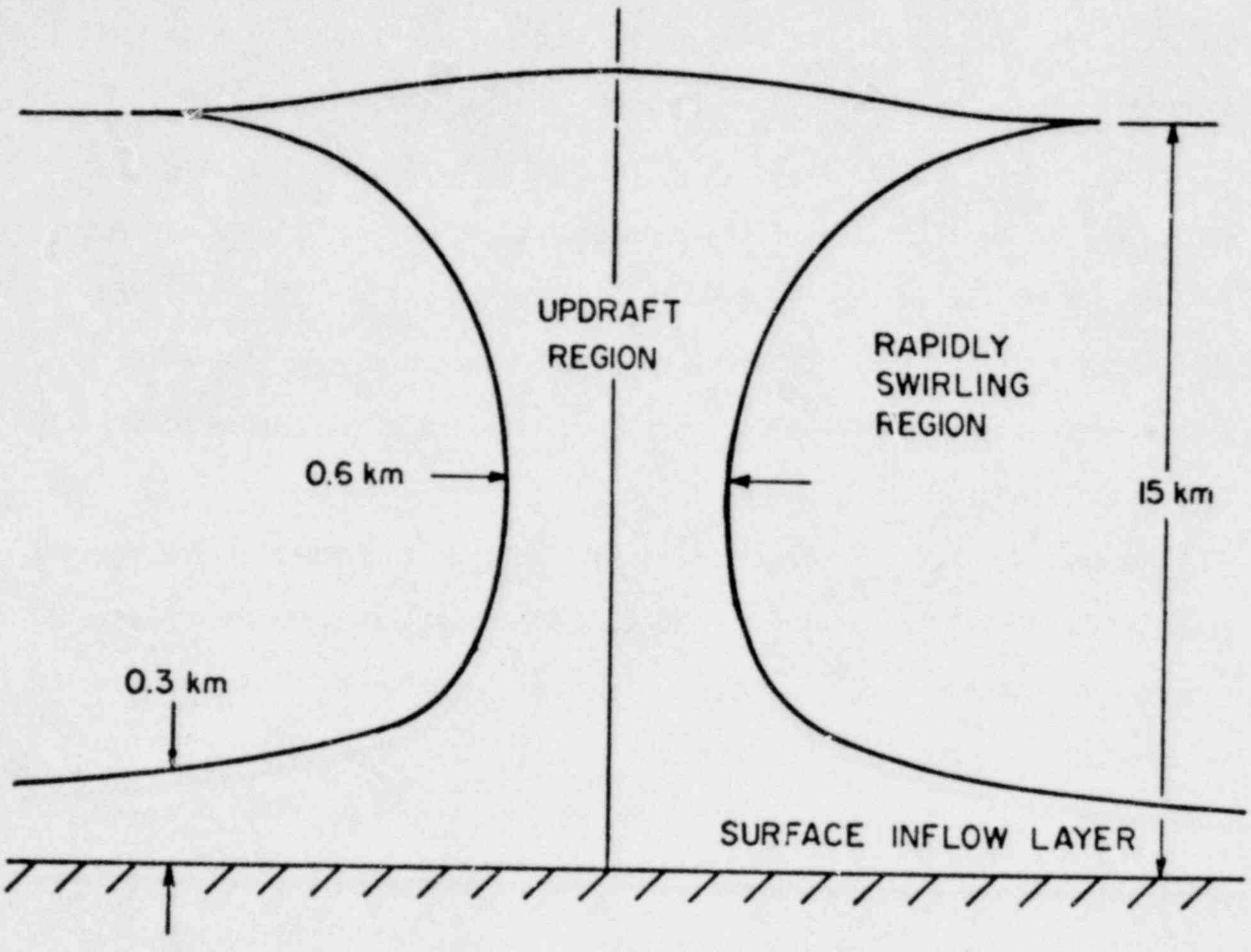

Figure 1. Schematic of mature stage tornadic storm.

1746 023

tornado suggesting a recirculating core which may or may not extend to the ground. The surface of maximum swirling wind lies close to the axis of the tornado. Assuming axisymmetry, the radius of this surface is typically of the order of a hundred meters for intense, mature stage tornadoes.

The surface inflow layer is a region in which the horizontal convergence occurs. The cyclostropic balance in the rapidly swirling region is not valid in this surface layer because of the ground. The inflow layer thickness increases from essentially zero far from the axis to a value of the order of 300 meters in the vicinity of the tornado axis. Most structures are embedded in the surface inflow layer and it is these winds - especially near the core which must be simulated in the laboratory. A sketch of the lower 1 km of the tornadic storm is given in Figure 2 to illustrate the nature of the flow to be simulated.

Remarkably little information is available on the distribution of windspeeds in naturally occurring tornadoes. The exceptions are the results reported by Hoecker [7,8] for the 1957 Dallas tornado and those reported by Goldman [20] for the 1963 Kankakee tornado. Hoecker was able to deduce windspeeds from a movie of this tornado by tracking the motion of tornado-generated debris, which included four by eight foot sheets of plywood that were picked up by the tornadic winds while Goldman used photogammetry to track cloud parcels on a movie of the Kankakee tornado. Figure 3 shows the resulting distribution of tangential windspeeds obtained by Hoecker. The maximum speed of 170 mph (274 kph) occurs at a radius of 130 feet (40 m) and an elevation of 225 feet (69 m). The isotachs have a roughly cylindrical shape as would be expected in a strongly rotating flow. Figure 4 shows the derived vertical velocity distribution. It is interesting to note that the

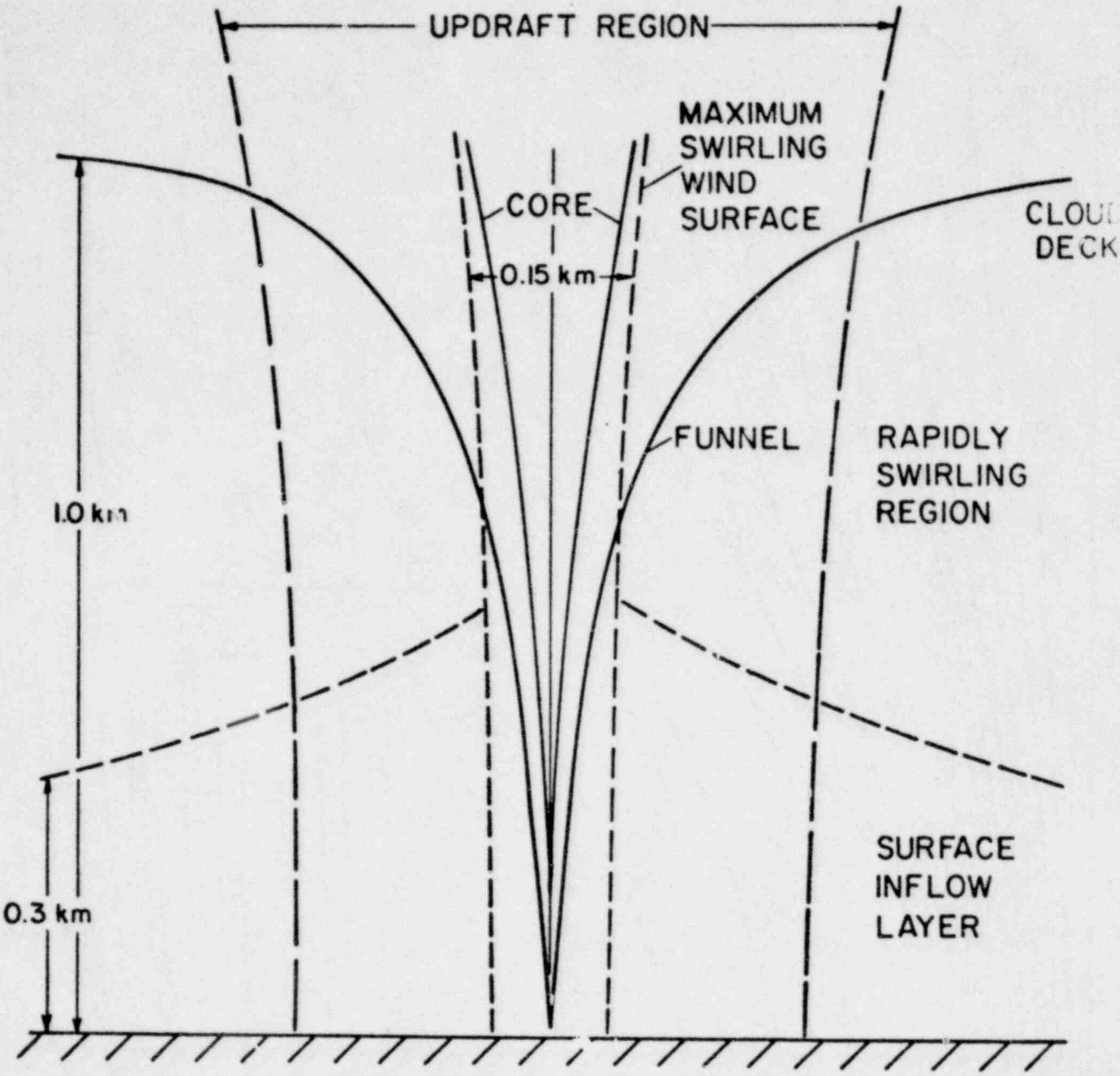

Figure 2. Schematic of lower 1 km. of mature stage tornado flowfield.

1746 025

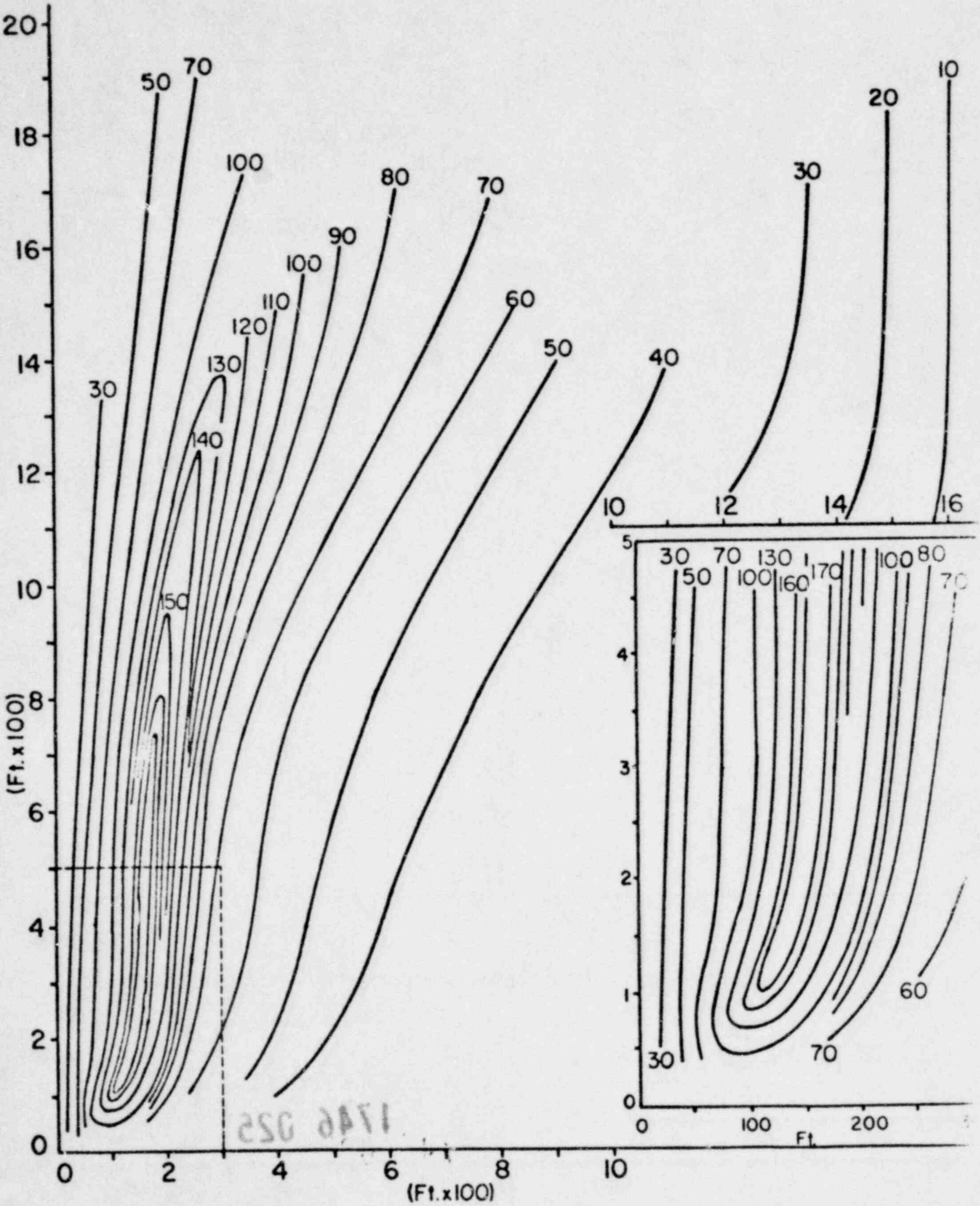

Figure 3. Distribution of derived tangential speed from the center of the tornado to a radius of 2000 ft. and from near the ground to about 1800 ft. in elevation (after Hoecker, ref. 7).

1746 026

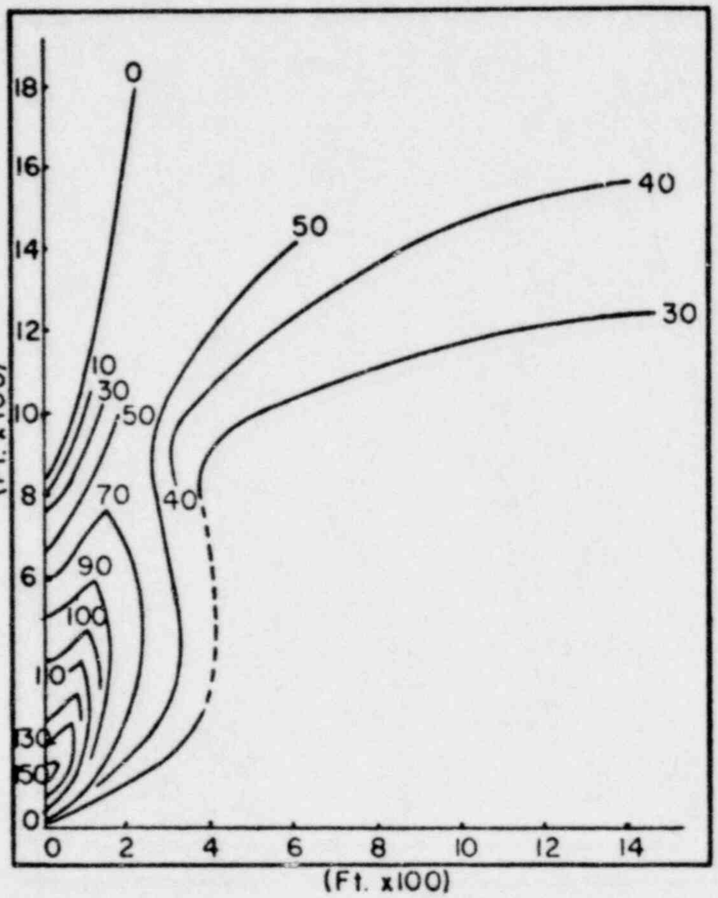

Figure 4a. Distribution of derived upward speed from the center of the tornado to about 1500 ft. in radius and from the ground to about 1700 ft. in elevation (after Hoecker, ref. 7).

1746 027

1746 028

1746 026

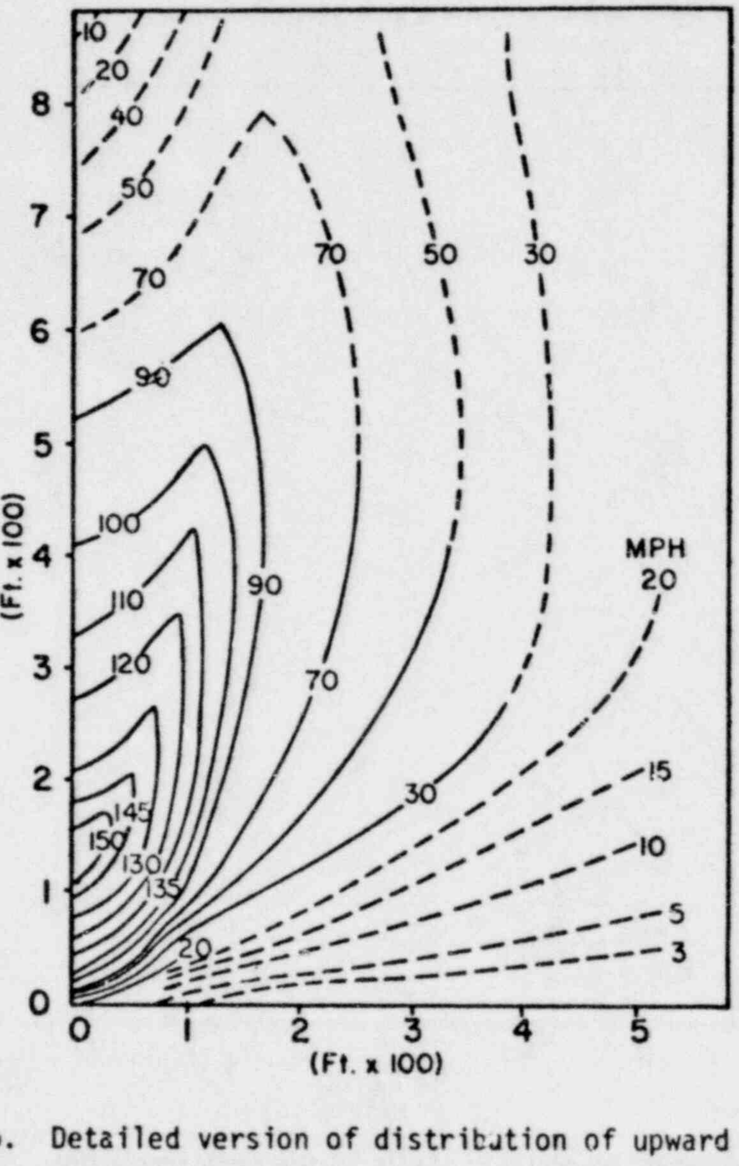

Figure 4b. Detailed version of distribution of upward speeds. Only the lower 900 ft. and the inner 500 ft. are shown (after Hoecker, ref. 7).

1746 027

maximum vertical velocity of 152 mph is comparable to the maximum tangential velocity and occurs at a somewhat smaller radius and height. Also, the observed funnel does not coincide with the surface of maximum windspeed. While some have criticized Hoecker's results as inaccurate and unrepresentative, these results are the most complete directly-obtained velocity data available for tornadic winds.

Laboratory Simulation of Tornadoes

Given the ease with which one can create a vortex in the laboratory, care must be exercised to ensure that the important features of natural tornadoes are reproduced in a simulation if the simulation is to be a useful one. Sources of rotation and convergence will lead to a vortex, although the vortex may not be typical of tornadoes. Among the features believed to be essential to a meaningful simulation are:

1. Independently controlled sources of rotation and convergence,
2. Restriction of the inflow layer to "low-levels",
3. Means of adjusting the core pressure deficit.

In this way, one can accurately model the following important meteorological variables in naturally-occurring tornadoes:

1. The ambient rotation of the tornado-spawning storm system,
2. The low-level convergence that concentrates the ambient vorticity into a vortex and which is driven by the pressure difference between the moist, adiabatic ascension along the core boundary and the ambient pressure profile far from the core,
3. The additional core pressure deficit that arises as a consequence of dry-adiabatic descent along the axis of the vortex for the case of the two-celled tornado vortex.

Additional features of a simulation which may have an effect on the modelling of wind loads on structures are surface roughness and the linear translation of the tornado vortex.

Among the tornado simulators that have been constructed, the design by Ward [12], which was used by Jischke and Parang [21], is unique in its ability to model tornadic winds and capture the essential features of tornado vortices. It, for example, exhibits both vortex breakdown and the unusual "core-splitting" phenomenon observed in naturally-occurring tornadoes. Ground pressure distributions obtained in this simulator reproduce the observed adverse pressure gradient near the edge of the updraft region. Finally, appropriately scaled measurements of the radius of maximum winds obtained with this simulator agree well with that observed by Hoecker for the 1957 Dallas tornado [7]. A sketch of the Ward design, modified for this study, is given in Figure 5.

Briefly, the apparatus consists of a right circular cylinder of radius 122 cm with sides of meshwire which can be independently rotated about the axis of the cylinder. A variable speed exhaust fan above a hole in the top of the apparatus creates an updraft and attendant converging horizontal flow which enters the apparatus through the meshwire. Thus, the radial and tangential components of velocity can be varied independently. This apparatus is distinguished from that of others (e.g. Chang [14]) in that, first, there is a honeycomb baffle which eliminates the direct effect of fan-induced vorticity. Second, the extent of the circular updraft region (roughly half the radius of the apparatus) is much larger than that in other simulators. Third, the aspect ratio of the surface inflow layer convergent zone (typically about 1/8) is smaller than that in other experiments. Fourth, the large convection zone above the converging surface inflow layer reduces the effect of

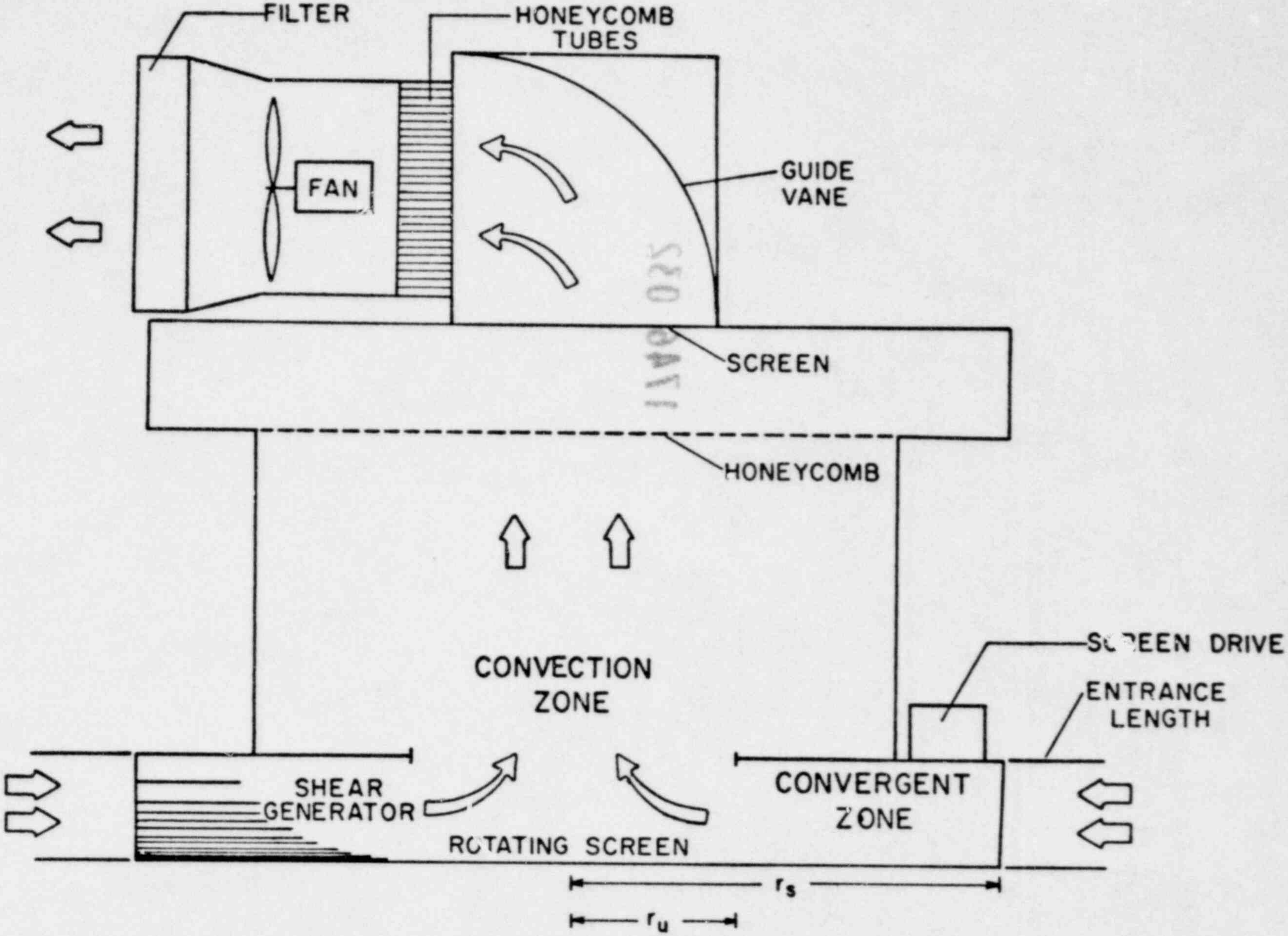

Figure 5. Schematic of tornado simulator.

teacuplike secondary flows observed in other simulators. The simulator has been modified for the present study by attaching a 46 cm entrance length to eliminate corner effects at the rotating screen. In addition, the porosity of the rotating screen has been made nonuniform so as to generate the vertically-sheared velocity profile typical of naturally occurring winds. Except for the simulator constructed by Church, Agee, and Snow [22], which in its essential features is identical to the Ward design, no other simulator reproduces as many of the observed features of naturally occurring tornadoes.

CHAPTER III

SCALING ANALYSIS

Accurate simulation of tornadic wind loads required that the important nondimensional parameters characterizing the laboratory simulation be the same as those characterizing naturally-occurring tornadoes. Requiring equal value of these parameters allows the scaling associated with the simulation to be deduced. To proceed, the important parameters characterizing the tornado flow field must first be determined.

Consider the flow due to a tornado vortex near the planar surface ($z=0$). Also, assume that the tornado vortex is axisymmetric with axis along $r=0$. As suggested by earlier discussion of the nature of tornadic wind fields, consider the tornadic flow to consist of a low-level, converging, swirling inflow region and a central region of updraft which are characterized by the following seven parameters:

Q	volume flow
Γ	imposed circulation far from the tornado axis
h	depth of the inflow layer
r_u	radius of updraft region
r_c	radius of tornado core
r_m	radium of maximum swirling wind
ν	kinematic viscosity

The additional effects of heat transfer and thermodynamics are believed to be unimportant. Also, the effects of relative motion between the tornado and the structure are ignored. The effects of relative motion between the tornado and the structure will be the subject of a subsequent report. In the laboratory simulation of the intense, mature-stage tornado, $r_c = r_m$. Dimensional analysis then implies that there are four nondimensional parameters that characterize the tornadic flow field. These parameters are written as

$$\frac{h}{r_c} \quad , \quad \frac{r_u}{r_c} \quad , \quad \frac{\Gamma h}{Q} \quad , \quad \frac{\Gamma}{\nu} \quad .$$

Note that the core radius r_c is taken to be the important length in characterizing the flow. This is done because the swirling velocity is roughly that of a combined Rankine vortex [22] and thus r_c determines the distance over which the velocity (and therefore the pressure) changes significantly.

Taking advantage of the analyses of Jischke and Parang [21] and Davies-Jones [24], the number of parameters characterizing the flow field can be reduced by one. These analyses show that the ratio r_u/r_c is a function of the single parameter $\Gamma\, r_u/Q$ -- the swirl ratio. Thus, only three parameters are important in characterizing the tornadic flow field; the parameters are written as h/r_u, $\Gamma r_u/Q$, Γ/ν. Typical values of these parameters, derived from the Hoecker data for the 1957 Dallas tornado [7], are shown in Table 1.

Table 1. Typical Parameter Values from 1957 Dallas Tornado [7]

Parameter	h/r_u	$\Gamma r_u/Q$	Γ/ν	r_c/r_u
Value	1.2	.8	2×10^9	0.4

1746 033

The parameter $\Gamma r_u/Q$ is often written in terms of the imposed swirl angle ϕ, which is easily measured in the laboratory. For an axisymmetric flow, the circulation Γ can be evaluated at the inlet screen as $2\pi r_s v_s$. Here v is the azimuthal velocity and the subscript s refers to the screen. The volumetric flow rate Q is similarly given by $Q = 2\pi r_s h u_s$ where u is the radial velocity. Thus,

$$\frac{\Gamma h}{Q} = \frac{v_s}{u_s} \equiv \tan \phi_s$$

Thus, ϕ_s is the imposed swirl angle at the screen. If one assumes axisymmetric inviscid, adiabatic flow in the convergent zone where the vertical velocity w vanishes, then the tangential velocity v is that of a potential vortex, $\Gamma/2\pi r$, and mass conservation requires that the radial velocity u also vary inversely with radius r. The swirl angle then remains constant in the convergent zone. For the value of $\Gamma h/Q$ implied by Table 1, then $\phi_s \simeq 45^0$.

In addition to requiring that the simulation correspond to typical values of the nondimensional parameters given in Table 1, the boundaries and velocity profiles imposed far from the tornado axis must be typical of those experienced in naturally-occuring tornadoes. Simulations involving boundary-layer-type winds have shown that the pressure loads deduced from experiment compare well with field data only if the vertical variations of the imposed velocities are typical of those occurring naturally. The paucity of data on naturally-occurring tornadoes makes it difficult to determine which velocity profiles are most appropriate for the case of tornadic winds. As a consequence, the data presented by Cermak [25] for naturally-occurring, boundary-layer-type, turbulent wind profiles for surface roughnesses typical of grasslands and forest-type topographies (e.g. roughness heights of the order of 1 to 10 meters) will be relied on. The associated turbulent velocity profile is assumed to have a power law variation in the vertical direction,

$$\frac{V}{V_{max}} = \left[\frac{z}{z_{max}}\right]^{1/\alpha} \qquad (1)$$

with α ranging from 3 to 7. In view of the small size of our simulator, it has been necessary to tailor the imposed velocity profile at the rotating screen to match this assumed form. The vertical shear of the imposed velocity at the rotating screen has been achieved by varying the porosity of the screen with height, according to the empirical result developed by Cockrell and Lee [26]. The variable porosity is obtained by affixing thin horizontal strips of masking tape to the rotating screen. The vertical spacing between the strips is varied so as to yield various power ($1/\alpha$) in the power-law velocity variation given by Eq. (1). Figure 6 shows a typical experimental result for which $\alpha \cong 5.9$. This screen was used in the measurements to be described subsequently.

The surface roughness scale has been chosen to represent that of grassland and forest-type topographies. Thus if z_r denotes the roughness height, it is required that

$$\left[\frac{z_r}{r_c}\right]_{model} = \left[\frac{z_r}{r_c}\right]_{tornado} \qquad (2)$$

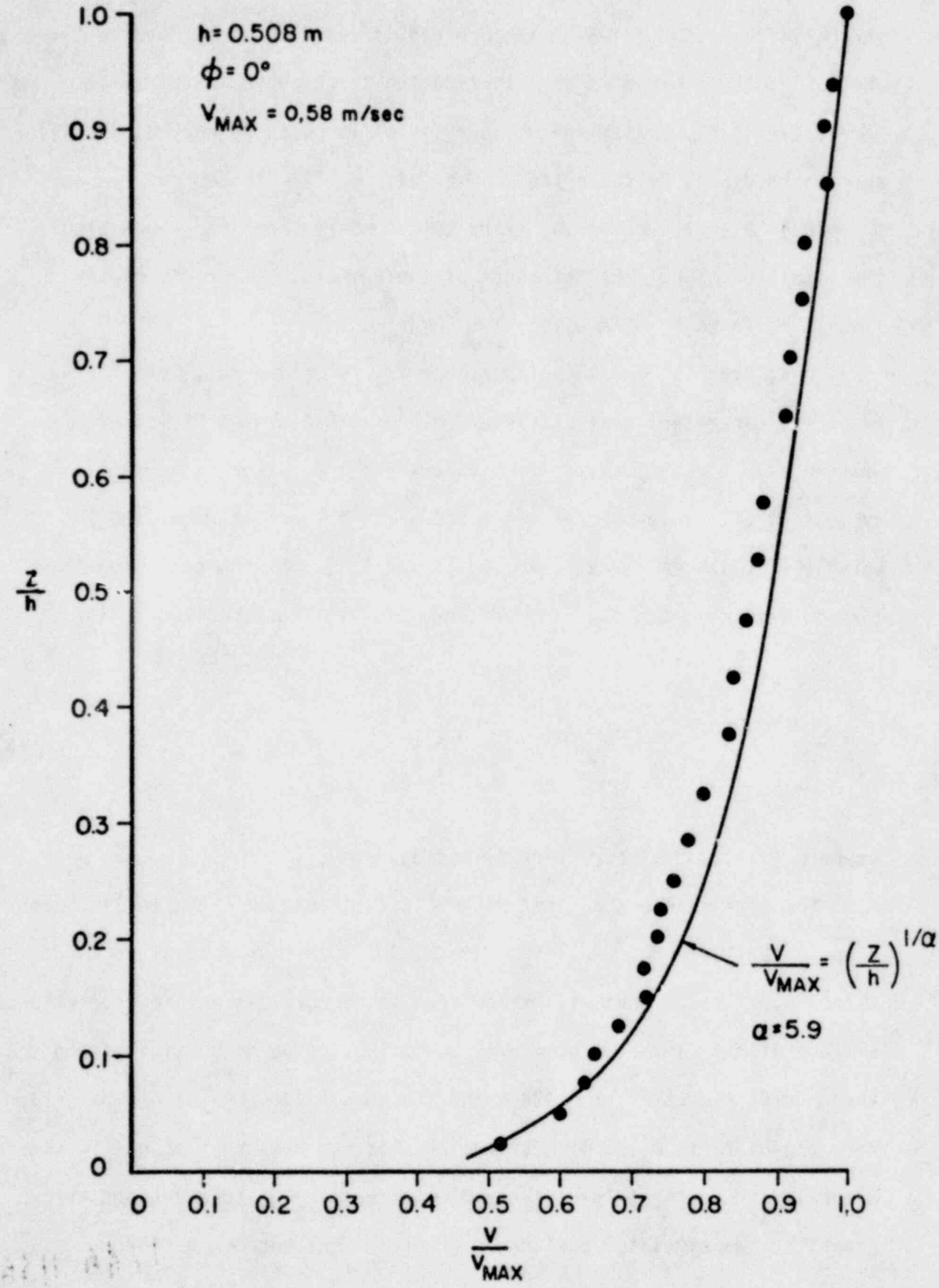

Figure 6. Sheared velocity profile (rough surface).

The roughness height typical of grassland topographies is 1 meter. In the Dallas tornado of 1957 the core [illegible] deduced by Hoecker to be about 50 meters. Thus (z_r/r_c) is expected to be approximately 0.02. For forest-type topographies for wh[illegible] $_r$ is as large as 10 meters, (z_r/r_c) approaches 0.2. By tailoring the velocity profile to represent that of a typical naturally-occurring turbulent boundary layer and roughening the simulator floor, the influence of the Reynolds number Γ/ν on the flow is believed to be small.

Thus, ignoring the Reyonlds number Γ/ν as unimportant, the four essential parameters that characterize the tornadic wind fields are written as: h/r_u, ϕ_s, α, z_r/r_c. Values for these four parameters typical of naturally-occurring tornadoes can be duplicated in the University of Oklahoma tornado simulation facility. Having evaluated the tornado flowfield scaling, the scaling for the structure then follows from

$$\left[\frac{L}{r_c}\right]_{\text{model}} = \left[\frac{L}{r_c}\right]_{\text{tornado}} \tag{3}$$

where L is a typical structure dimension.

The size of the simulator restricts the depth h of the inflow layer than can be achieved. An inflow depth of 0.508 m was chosen so as to obtain model sizes that will allow adequate visualization and resolution without significant flow blockage. With this value of h, it is found that the updraft radius r_u is 0.424 m and the smooth floor value of the vortex core radius r_c is 0.170 m. Taking the relative roughness height for the naturally occurring tornado to be 0.02 corresponding to grassland topographies, the simulator surface roughness height becomes 0.0034 m.

These results then define the geometry of the simulator.

CHAPTER IV

CYLINDRICAL MODEL

The model used in these experiments is a circular cylinder with a hemispherical dome roof. This geometry is typical of containment buildings used to house nuclear reactors. A typical containment building is 34 meters in diameter and 65 meters high. With a typical tornado core radius of 50 meters corresponding to the simulated vortex radius, the dimensions of the scaled containment building model then become 0.229 m high and 0.114 m in diameter. A drawing of the model is shown in Figure 7. The location of the 63 pressure ports on the surface of the model are also shown in Figure 7. The numbering scheme used to locate the ports is shown in Figure 8.

The 63 surface pressure ports are connected to a single pressure transducer by means of a Scanivalve switching system. The dynamic pressures to be measured are of the order of a torr or less and thus require a sensitive pressure transducer. A Datametrics 570 D 10 T-2A1-V3 capacitance type pressure sensor and 1174-A4A-5A1-A78 electronic manometer with resolution of 10^{-4} torr has been employed for this purpose. Because of the turbulent fluctuations in the flow, the output signal from the manometer is electronically averaged to give the time-averaged surface pressure. The resulting data are presented in the form of a pressure coefficient, C_p, where

$$C_p = \frac{P - P_{ref}}{\frac{1}{2}\,\rho V^2{}_{ref}} \qquad (4)$$

Here P_{ref} is the pressure that would be measured on the ground (z=0) at the center of the model, in the absence of the model. The reference velocity V_{ref} is the vertically averaged velocity that would occur with purely

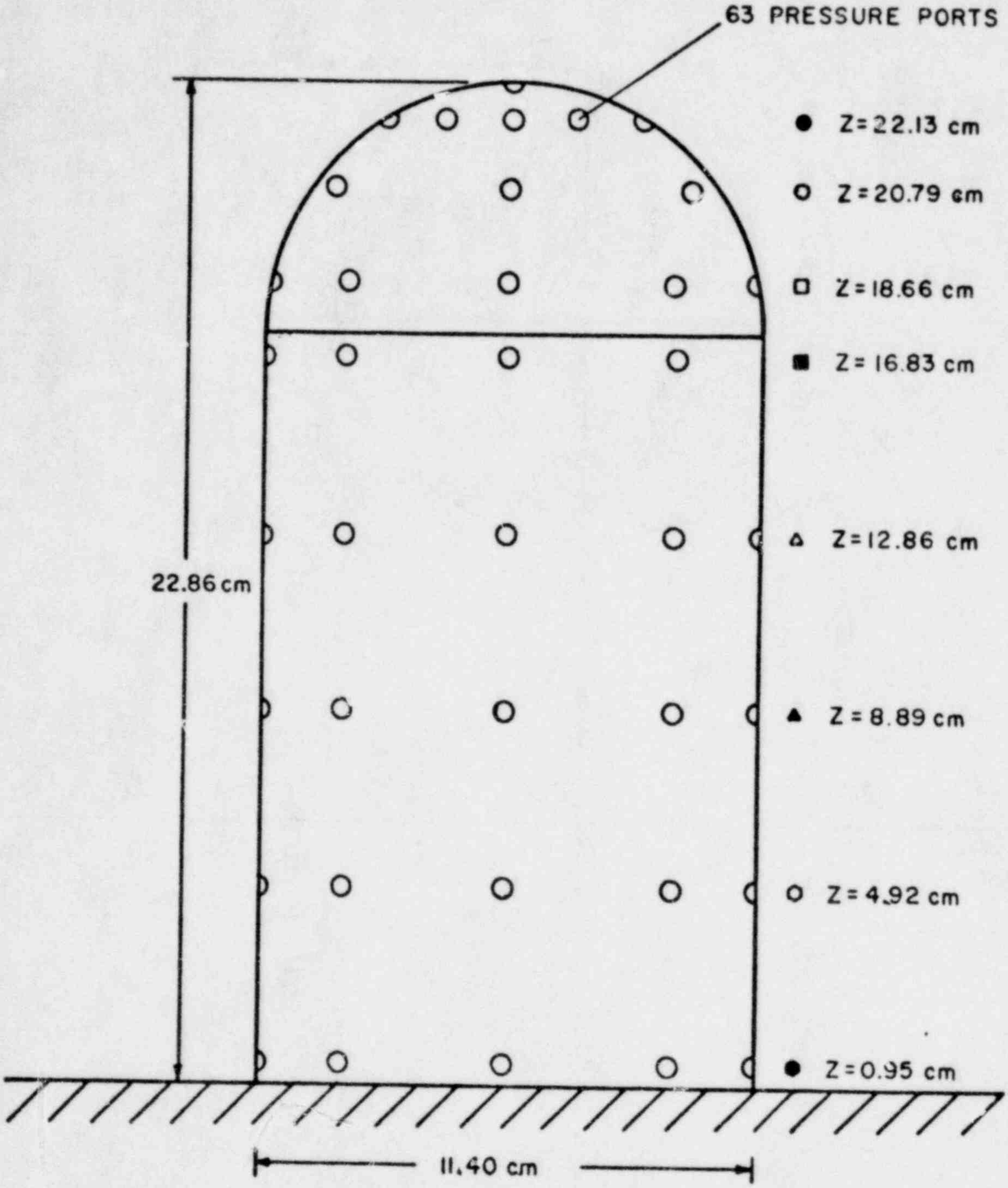

Figure 7. Schematic of the cylindrical model with pressure port locations.

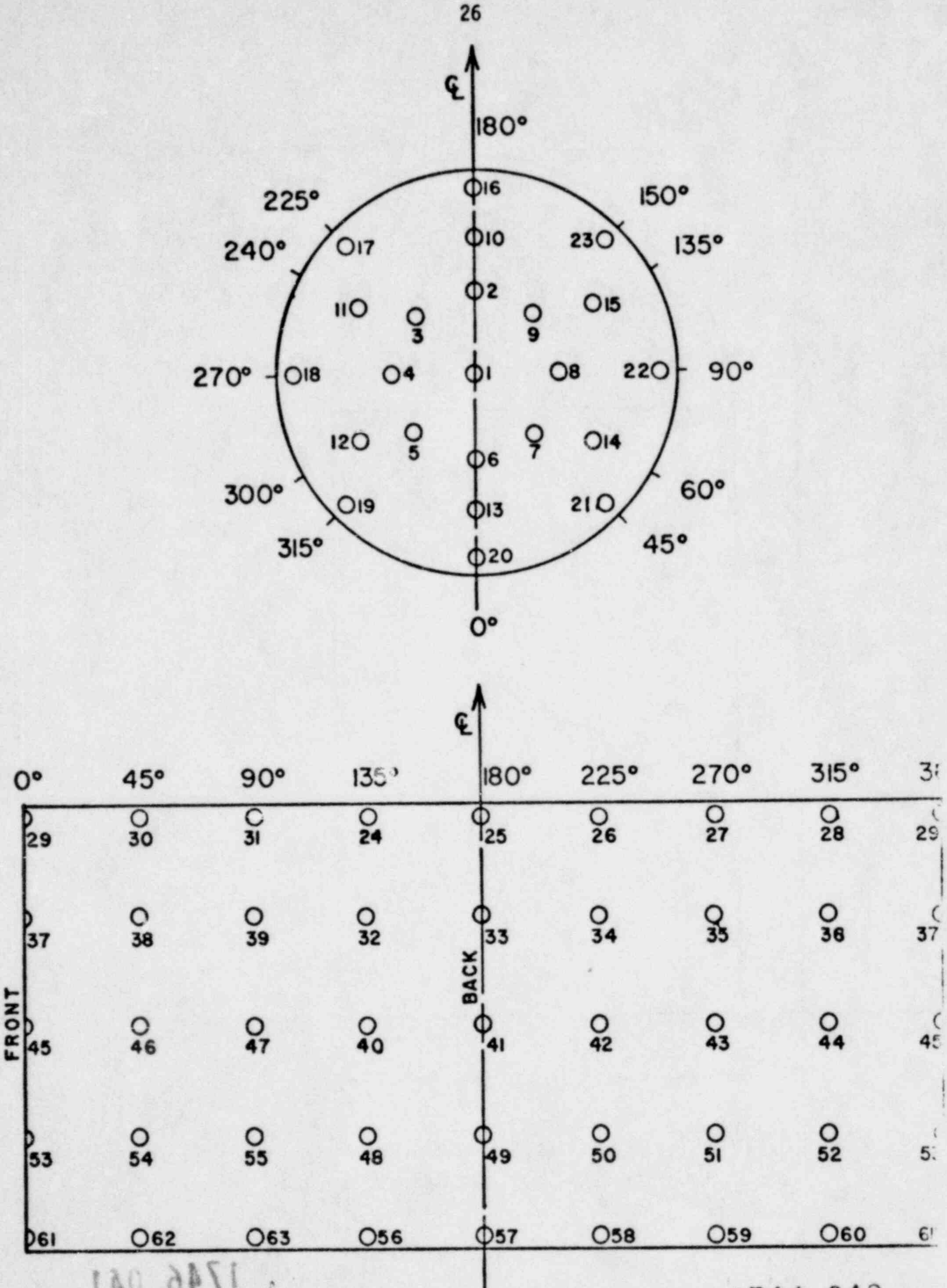

1746 042

Figure 8. Numbering scheme to identify pressure ports on cylindrical model.

horizontal flow at the center of the model, in the absence of the model, and is given at any station r in terms of the volume flow rate Q by $V_{ref} = Q \sec \phi / 2\pi rh$.

Measurements of the surface pressure have been made for three model locations (r = 0.114 m, 0.457 m, and 0.762 m) and two different swirl angles (ϕ = 0, 45°). The three locations correspond to the convection zone (0.114 m), the boundary between the convection zone and the convergent zone (0.457 m), and the convergent zone (0.762 m). The data is presented graphically in Figures 9-11 and in tabular form in Tables 2-4. These data and those that follow have an uncertainty of the order of ten percent or less.

Pressure Coefficient

Figure 9a and Table 2a show the surface pressure coefficient with zero imposed swirl and the model in the convergent zone where the vertical velocity is zero. The measured pressure coefficient is symmetrical with respect to the flow direction. The variation of C_p with angle θ on the circular cylinder portion of the model are quite like those for an infinite circular cylinder in a uniform flow. The imposed vertical shear does cause a slight vertical variation in the pressure coefficient along the line $\theta = 0°$ suggesting a stagnation point near z = 0.162 m.

Figure 9b and Table 2b show the effect of swirl on the surface pressure coefficient when the model is in the convergent zone. The pressure distribution is highly asymmetric with respect to the local flow direction. As a consequence, the force on the model has both drag and side force components, reckoned with respect to the local wind direction. The maximum pressure coefficient ($C_{p_{max}}$ = 1.05) does not change significantly with swirl in this case. However, the pressure coefficient on the hemispherical roof is considerably reduced with swirl. The observed asymmetry in the pressure distribution is due to the nonuniform velocity induced around the cylindrical model by the tornado-like vortex at the center of the apparatus. It is a direct consequence of the circulation present in the tornado-like vortical flow.

Figure 10 and Table 3 give the surface pressure coefficient for $\phi=0°$ and $\phi=45°$ when the model is placed at 0.457 m from the center. The vertical velocity in the convection zone has begun to substantially alter the pressure coefficient and its variation with height z and angle θ. The maximum pressure coefficient for purely radial flow is reduced to 0.40 while the maximum pressure coefficient with swirl, 0.92, is rather close to the corresponding value in the convergent zone. The effect of the imposed swirl ϕ remains similar to that in the convergent zone in that the accelerating flow causes an asymmetry (with respect to the undisturbed flow direction) in the distribution of C_p with angle θ.

The pressure distribution in the zero swirl case is quite sensitive to the distribution of vertical velocity imposed by the exhaust system. This is particularly true near the base of the model where separation is occurring because of the imposed vertical velocity. Slight variations in the vertical velocity with position will have a large effect on the location of separation and will thereby cause significant asymmetries in the surface pressure distribution.

Results for the surface pressure coefficient when the model is in the convection zone are given in Figure 11 and Table 4. Figure 11a shows the pressure coefficient when the imposed swirl angle ϕ is 0°. Note that the values plotted in Figure 11a. are ten times the measured C_p. Thus, the

Table 2a. Surface Pressure Coefficient on the Cylindrical Model in the Convergent Zone (r = 0.762 m) with Imposed Swirl Angle of 0°

Port	1	2	3	4	5	6	7	8	9
C_p	-1.09	-0.90	-0.89	-1.07	-1.16	-0.93	-1.16	-1.14	-0.90
Port	10	11	12	13	14	15	16	17	18
C_p	-0.89	-0.92	-1.00	-0.07	-0.97	-0.91	-0.91	-0.88	-1.23
Port	19	20	21	22	23	24	25	26	27
C_p	-0.39	0.60	-0.36	-1.19	-0.88	-0.88	-0.91	-0.86	-1.16
Port	28	29	30	31	32	33	34	35	36
C_p	-0.18	0.89	-0.12	-1.16	-0.91	-0.90	-0.92	-1.13	-0.20
Port	37	38	39	40	41	42	43	44	45
C_p	0.95	-0.23	-1.15	-0.91	-0.89	-0.91	-1.16	-0.18	0.90
Port	46	47	48	49	50	51	52	53	54
C_p	-0.20	-1.17	-0.92	-0.87	-0.88	-1.09	-0.21	0.95	-0.20
Port	55	56	57	58	59	60	61	62	63
	-1.08	-0.89	-0.83	-0.88	-0.93	-0.13	-0.93	-0.14	-0.94

Table 2b. Surface Pressure Coefficient on the Clyindrical Model in the Convergent Zone (r = 0.762) with Imposed Swirl Angle of 45°

Port	1	2	3	4	5	6	7	8	9
C_p	-1.02	-0.79	-0.91	-1.02	-0.85	-1.00	-1.11	-0.87	-0.85
Port	10	11	12	13	14	15	16	17	18
C_p	-0.81	-1.18	-0.12	-0.64	-0.97	-0.82	-0.84	-1.07	-0.15
Port	19	20	21	22	23	24	25	26	27
C_p	0.76	-0.33	-1.11	-0.83	-0.89	-0.90	-0.87	-1.12	0.17
Port	28	29	30	31	32	33	34	35	36
C_p	0.98	-0.30	-1.02	-0.86	-0.88	-0.90	-1.15	0.30	1.05
Port	37	38	39	40	41	42	43	44	45
C_p	-0.50	-0.86	-0.84	-0.79	-0.80	-1.06	0.43	0.97	-0.59
Port	46	47	48	49	50	51	52	53	54
C_p	-0.80	-0.81	-0.74	-0.75	-1.02	0.38	0.87	-0.55	-0.75
Port	55	56	57	58	59	60	61	62	63
C_p	-0.74	-0.70	-0.72	-0.80	0.39	0.65	-0.43	-0.75	-0.73

Table 3a. Surface Pressure Coefficient in the Cylindrical Model at the Boundary of the Convergent and Convection Zones (r = 0.457 m) with Imposed Swirl Angle of 0°

Port	1	2	3	4	5	6	7	8	9
C_p	-0.77	-1.01	-0.82	-0.79	-0.87	-0.98	-0.89	-0.78	-0.79
Port	10	11	12	13	14	15	16	17	18
C_p	-1.09	-1.02	-0.95	-0.69	-0.90	-0.82	-1.09	-0.89	-0.81
Port	19	20	21	22	23	24	25	26	27
C_p	-0.58	-0.13	-0.47	-0.84	-0.87	-0.69	-0.98	-0.71	-0.73
Port	28	29	30	31	32	33	34	35	36
C_p	-0.28	0.20	-0.30	-0.76	-0.78	-0.90	-0.76	-0.55	-0.24
Port	37	38	39	40	41	42	43	44	45
C_p	0.33	-0.15	-0.64	-0.54	-0.58	-0.45	-0.32	-0.10	0.35
Port	46	47	48	49	50	51	52	53	54
C_p	-0.03	-0.34	-0.67	-0.45	-0.51	-0.54	-0.19	0.40	-0.19
Port	55	56	57	58	59	60	61	62	63
	[illegible]	-0.22	-0.19	-0.21	-0.24	0.01	0.35	0.01	-0.25

Table 3b. Surface Pressure Coefficient on the Cylindrical Model at the Boundary of the Convergent and Convection Zones (r = 0.457 m) with Imposed Swirl Angle of 45°

Port	1	2	3	4	5	6	7	8	9
C_p	-0.80	-0.79	-0.80	-0.99	-1.05	-1.04	-0.84	-0.82	-0.86
Port	10	11	12	13	14	15	16	17	18
C_p	-0.83	-1.13	-0.61	-1.01	-0.85	-0.89	-0.87	-1.13	-0.01
Port	19	20	21	22	23	24	25	26	27
C_p	0.13	-0.84	-0.90	-0.90	-0.94	-0.88	-0.86	-1.00	0.60
Port	28	29	30	31	32	33	34	35	36
C_p	0.41	-0.83	-0.88	-0.91	-0.83	-0.82	-0.81	0.89	0.36
Port	37	38	39	40	41	42	43	44	45
C_p	-0.99	-0.83	-0.86	-0.78	-0.78	-0.67	0.92	0.30	-0.98
Port	46	47	48	49	50	51	52	53	54
C_p	-0.83	-0.88	-0.86	-0.84	-0.74	0.90	0.36	-1.04	-0.86
Port	55	56	57	58	59	60	61	62	63
	[illegible]	[illegible]	[illegible]	[illegible]	0.74	0.56	-0.72	[illegible]	-0.90

Table 4a. Surface Pressure Coefficient on the Cylindrical Model in the Convection Zone (r = 0.114 m) with Imposed Swirl Angle of 0°

Port	1	2	3	4	5	6	7	8	9
C_p	-0.08	-0.07	-0.07	-0.07	-0.06	-0.07	-0.07	-0.07	-0.07
Port	10	11	12	13	14	15	16	17	18
C_p	-0.07	-0.07	-0.07	-0.07	-0.07	-0.06	-0.05	-0.06	-0.07
Port	19	20	21	22	23	24	25	26	27
C_p	-0.06	-0.06	-0.06	-0.06	-0.05	-0.03	-0.03	-0.04	-0.04
Port	28	29	30	31	32	33	34	35	36
C_p	-0.02	-0.02	-0.03	-0.04	-0.02	-0.02	-0.02	-0.01	-0.00
Port	37	38	39	40	41	42	43	44	45
C_p	0.00	-0.01	-0.02	-0.01	-0.01	-0.01	-0.00	0.01	0.01
Port	46	47	48	49	50	51	52	53	54
C_p	0.00	-0.01	-0.00	-0.01	-0.01	0.00	0.01	0.01	0.00
Port	55	56	57	58	59	60	61	62	63
C_p	-0.00	-0.00	-0.00	-0.00	0.00	0.01	0.01	0.00	0.00

Table 4b. Surface Pressure Coefficient on the Cylindrical Model in the Convection Zone (r = 0.114 m) with Imposed Swirl Angle of 45°

Port	1	2	3	4	5	6	7	8	9
C_p	-2.08	-2.61	-2.78	-2.15	-1.95	-1.85	-1.82	-1.83	-2.09
Port	10	11	12	13	14	15	16	17	18
C_p	-2.45	-2.32	-1.97	-1.52	-1.74	-1.86	-1.89	-2.11	-2.18
Port	19	20	21	22	23	24	25	26	27
C_p	-1.33	-1.29	-1.39	-1.74	-1.94	-1.85	-1.79	-1.61	-1.69
Port	28	29	30	31	32	33	34	35	36
C_p	-0.74	-0.83	-1.12	-1.66	-1.83	-1.48	-1.55	-1.22	-0.48
Port	37	38	39	40	41	42	43	44	45
C_p	-0.64	-1.15	-1.67	-1.63	-1.62	-1.50	-0.78	-0.37	-0.66
Port	46	47	48	49	50	51	52	53	54
C_p	-1.21	-1.63	-1.72	-1.64	-1.23	-0.21	-0.11	-0.51	-1.15
Port	55	56	57	58	59	60	61	62	63
C_p	-1.52	-1.03	-0.45	-0.01	0.32	0.29	-0.15	-0.61	-0.92

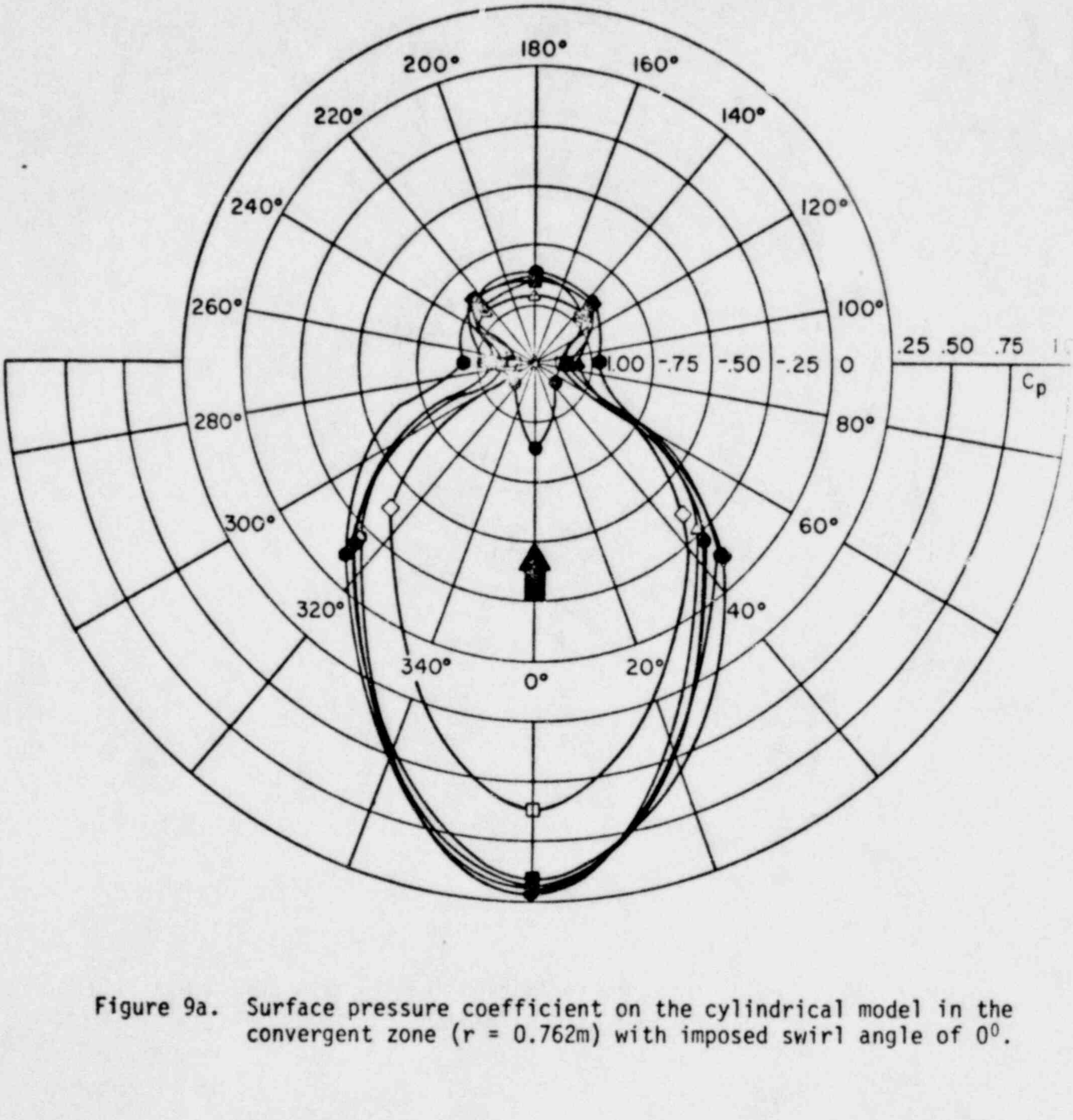

Figure 9a. Surface pressure coefficient on the cylindrical model in the convergent zone (r = 0.762m) with imposed swirl angle of 0^0.

1746 051

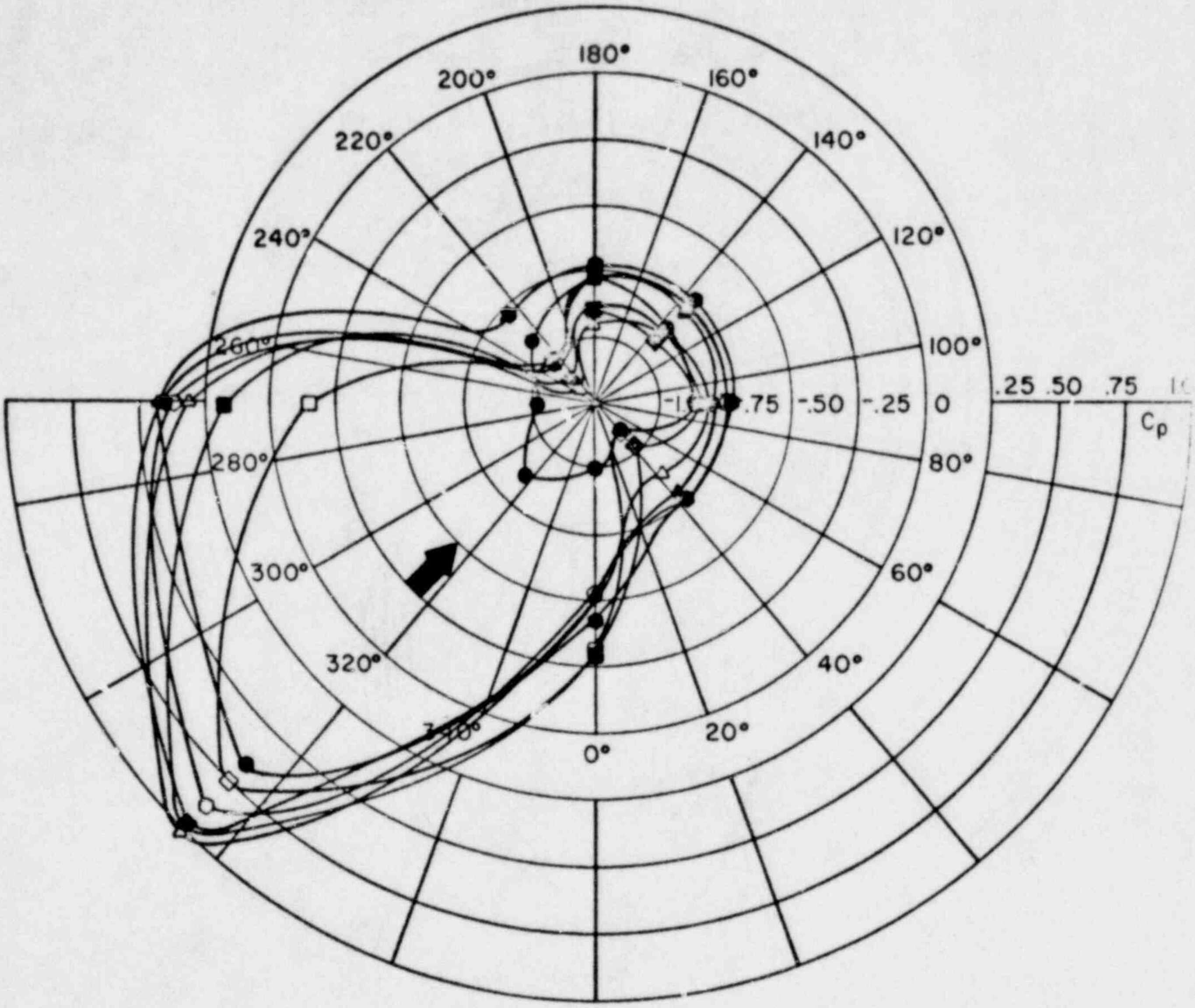

Figure 9b. Surface pressure coefficient on the cylindrical model in the convergent zone (r = 0.762m) with imposed swirl angle of 45^0.

1746 052

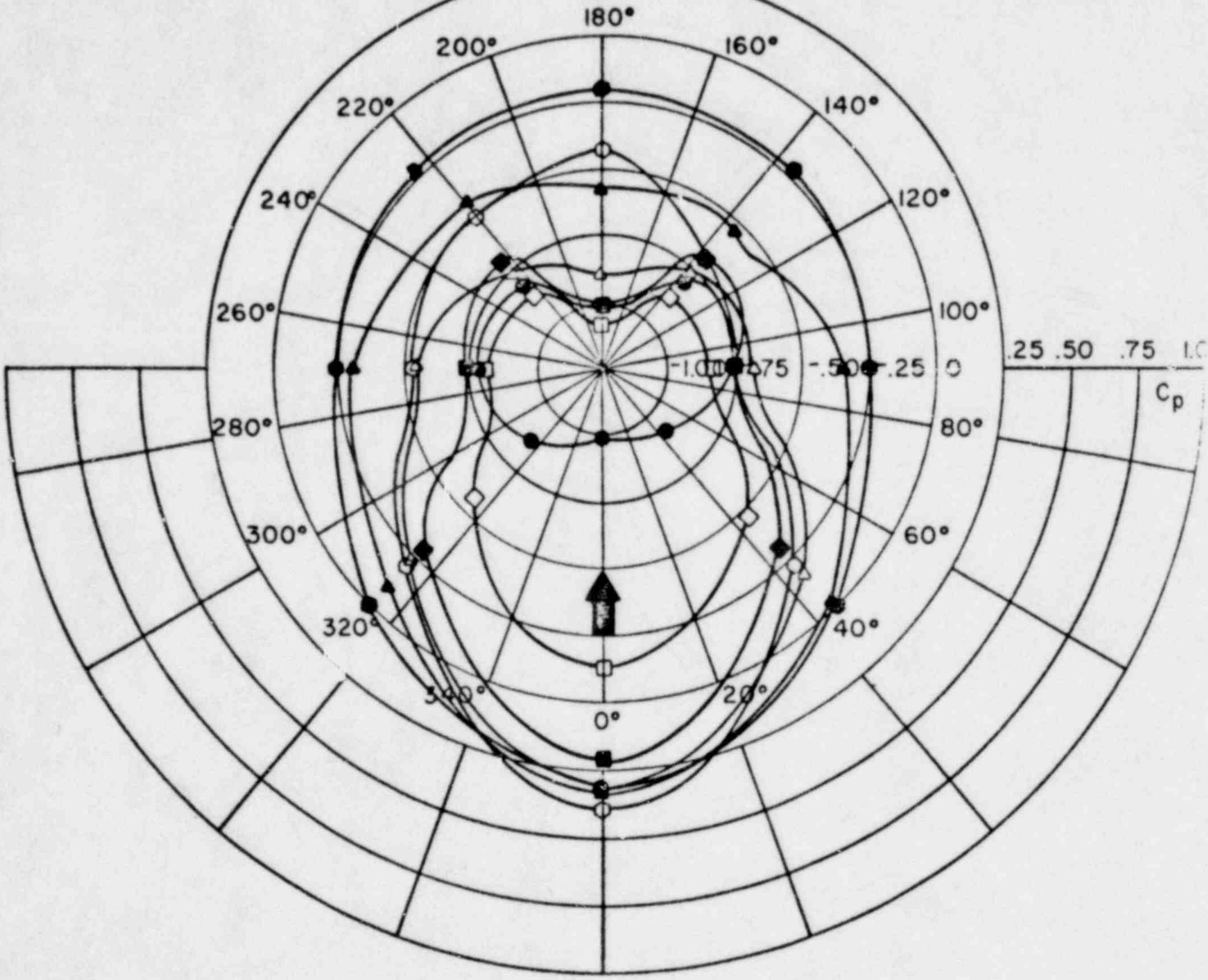

Figure 10a. Surface pressure coefficient on the cylindrical model at the boundary of the convergent and convection zones (r = 0.457m) with imposed swirl angle of 0^0.

1746 053

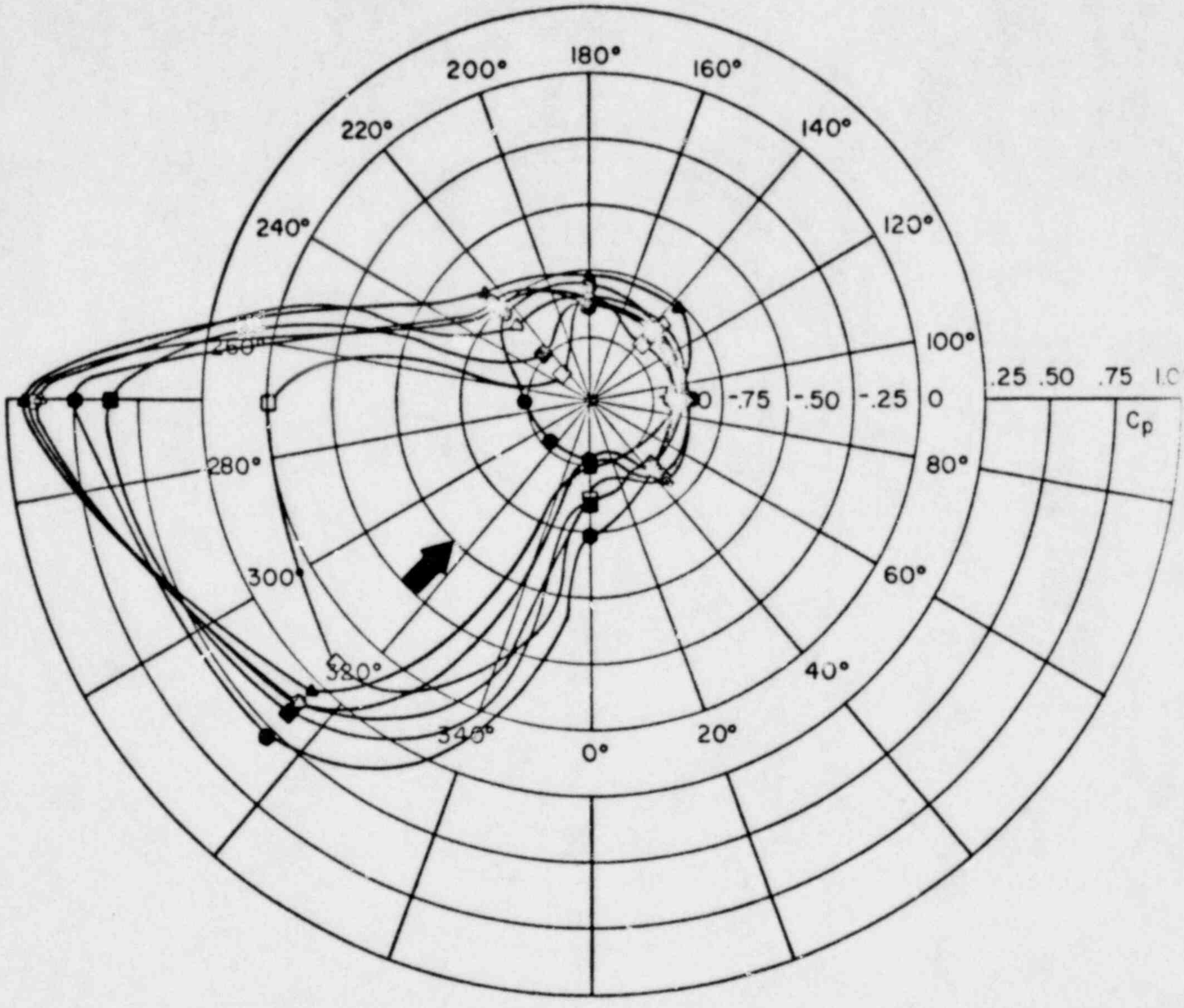

Figure 10b. Surface pressure coefficient on the cylindrical model at the boundary of the convergent and convection zones (r = o.457m) with imposed swirl angle of 45^0.

1746 054

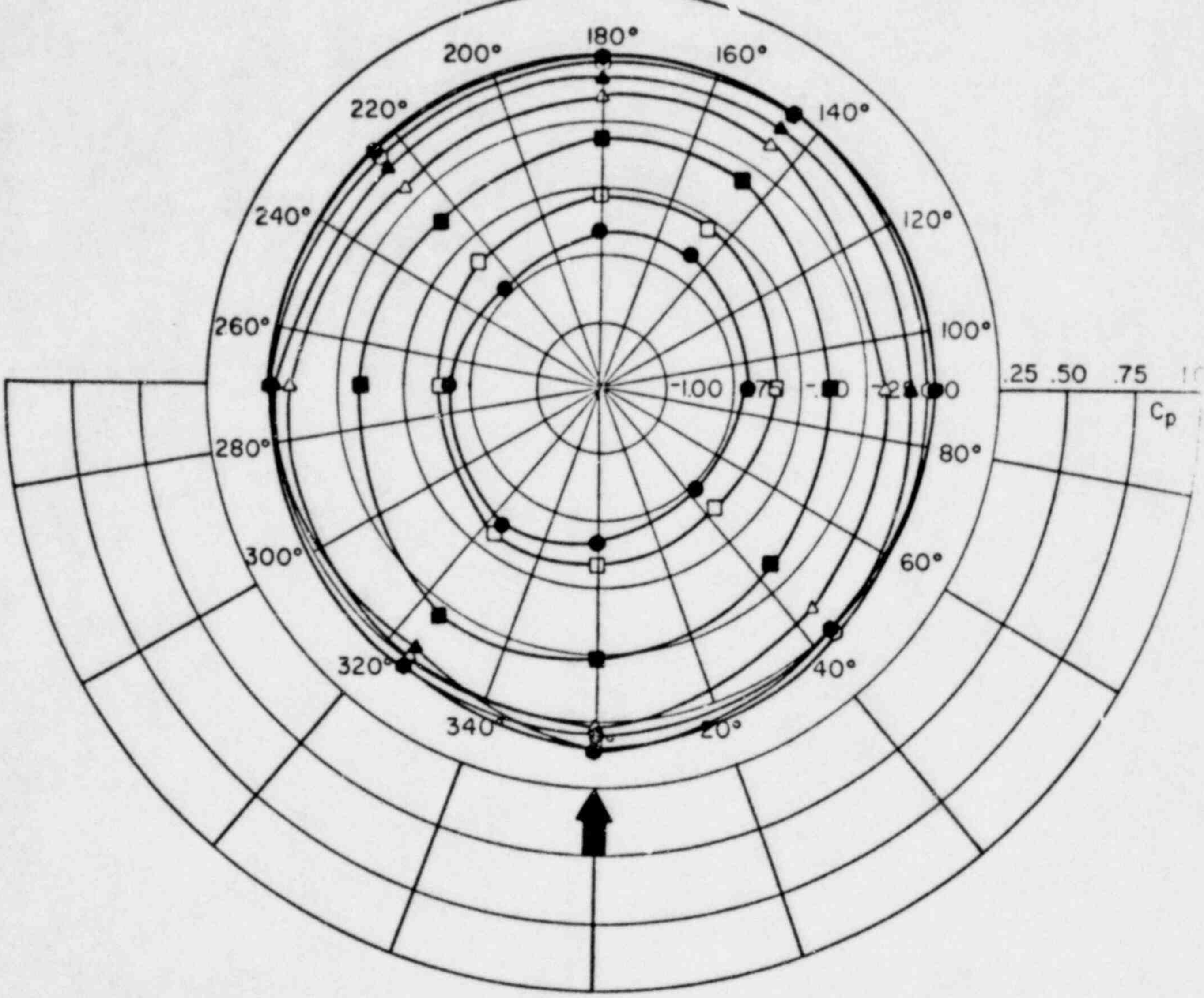

Figure 11a. Surface pressure coefficient on the cylindrical model in the convection zone (r = 0.114m) with imposed swirl angle of 0^0 (C_p x 10).

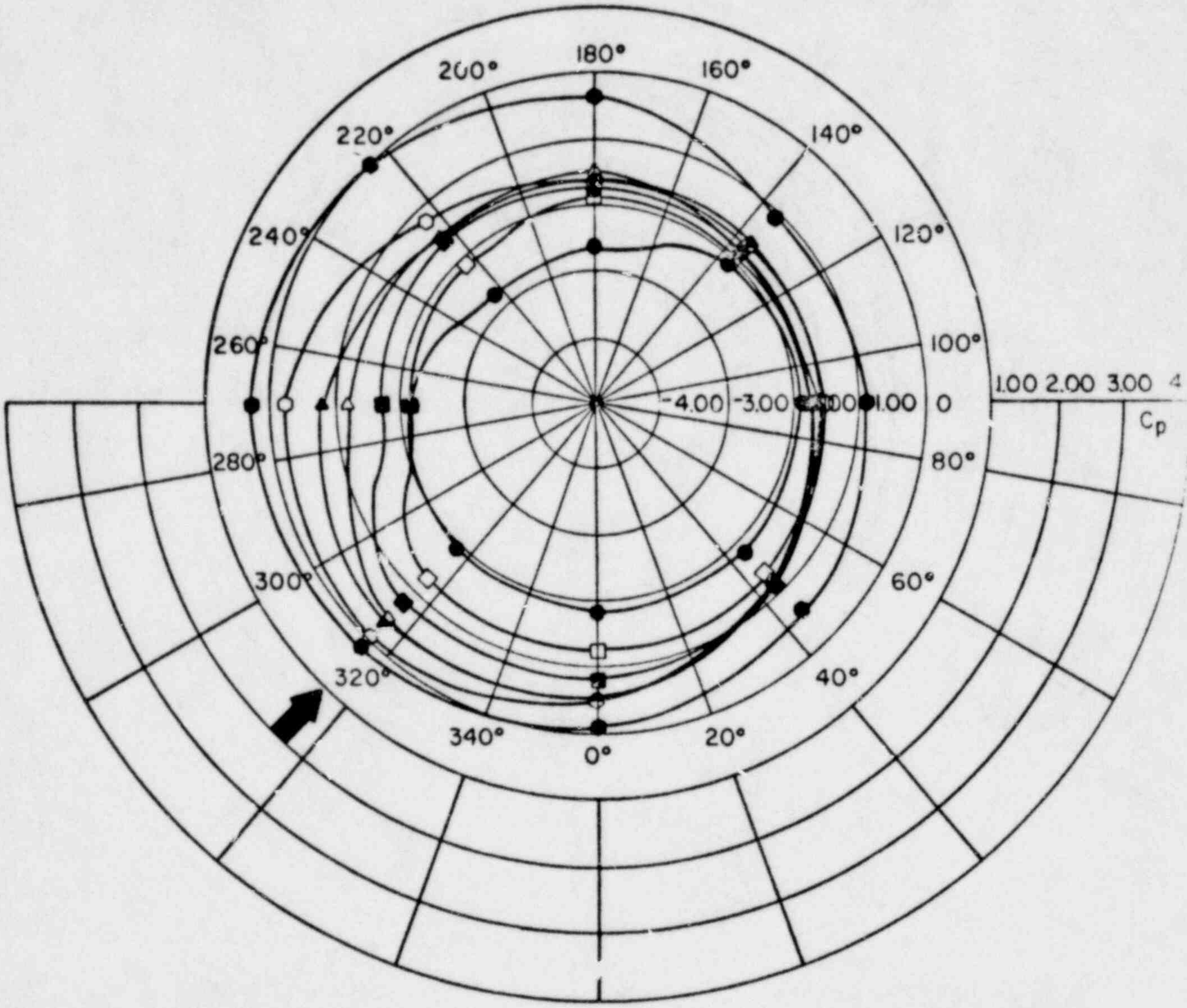

Figure 11b. Surface pressure coefficient on the cylindrical model in the convection zone (r = 0.114m) with imposed swirl angle of 45^0.

actual values of C_p are rather small. This occurs in the nonswirling case because the flow near the ground plane in the convection zone is separated and the velocities are rather low. However, with swirl, as shown in Figure 11b , the flow in the convection zone is not separated and the magnitude of the pressure coefficient is relatively large, with absolute values as large as 2.78. Also, in contrast to the results in the convergent zone and at the boundary of the convergent and convection zones, the pressure distribution in the convection zone is rather symmetric when there is an imposed swirl.

Flow visualization studies show that this symmetric pressure distribution occurs because the vortex has attached itself to the model. That is, as the model moves toward the vortex, a point is reached where the vortex itself moves away from the center of the apparatus toward the model and attaches itself to the model. The pressure distribution on the model then becomes more symmetric than it was prior to attachment Flow visualization studies show that vortex attachment occurs when the center of the model is at $r \doteq 0.17$ m, corresponding to a radial location equal to about twice the vortex radius -- e.g. the inner edge of the model is at the outer edge of the vortex core.

Force and Moment Coefficients

These results for the pressure coefficient allow the total force $\vec{F}$ and moment $\vec{M}$ to be estimated. The total force $\vec{F}$ and moment $\vec{M}$ are given by

$$\vec{F} = -\oiint_S p\,\hat{n}\,dS + \oiint_S \hat{n} \cdot \vec{\vec{\tau}}\,dS \tag{5}$$

$$\vec{M} = -\oiint_S p\vec{r} \times \hat{n}\,dS + \oiint_S \vec{r} \times (\hat{n}\cdot\vec{\vec{\tau}})\,dS \tag{6}$$

where $\overleftrightarrow{\tau}$ is the viscous stress tensor, S refers to the surface area of the model, and $\hat{n}$ is the outward unit normal to the surface S. For blunt bodies such as the cylindrical structure considered here, the viscous stress constribution is negligible.

We define the force and moment coefficients as

$$\vec{C}_F = \frac{\vec{F}}{\frac{1}{2}\rho V_{ref}^2 A} \qquad (7)$$

$$\vec{C}_M = \frac{\vec{M}}{\frac{1}{2}\rho V_{ref}^2 A l} \qquad (8)$$

where here A is the frontal area of the structure ($A = dh + \pi d^2/8$ where d is the diameter of the cylinder and h is the cylinder height) and l is the total height of the structure ($l = h + d/2$). Equations (5) and (6) allow us to write expressions for the force and moment coefficients as

$$\vec{C}_F = -\frac{1}{A}\iint C_p \, \hat{n} \, dS \qquad (9)$$

$$\vec{C}_M = -\frac{1}{A}\iint C_p \left(\frac{\vec{r}}{l}\right) \times \hat{n} \, dS \qquad (10)$$

These integrals have been evaluated numerically using the experimentally determined values of C_p. The results are shown in Table 5 where we have written the components of $\vec{C}_F$ and $\vec{C}_M$, referred to a right-handed cartesian coordinate system (x,y,z) where x and y are horizontal -- with x in the direction of the local flow and thus at an angle ϕ to the radius vector -- and z is vertical (see Figure 12). The values of the drag coefficient (C_{F_x}) in the convergent zone are quite comparable to those observed in boundary-layer-type winds. For example, Sachs [27] reports a

Table 5. Force and Moment Coefficients for the Cylindrical Model

Location (r)	Swirl Angle	C_{F_x}	C_{F_y}	C_{F_z}	C_{M_x}	C_{M_y}	C_{M_z}
0.762 m	0^0	1.00	0.00	0.35	0.00	0.42	0
	45^0	1.00	-0.11	0.32	0.04	0.45	0
0.457 m	0^0	0.60	-0.05	0.35	0.01	0.28	0
	45^0	0.82	-0.46	0.35	0.18	0.34	0
0.114 m	0^0	0.01	0.00	0.03	0.00	0.00	0
	45^0	0.90	0.20	0.82	-0.15	0.33	0

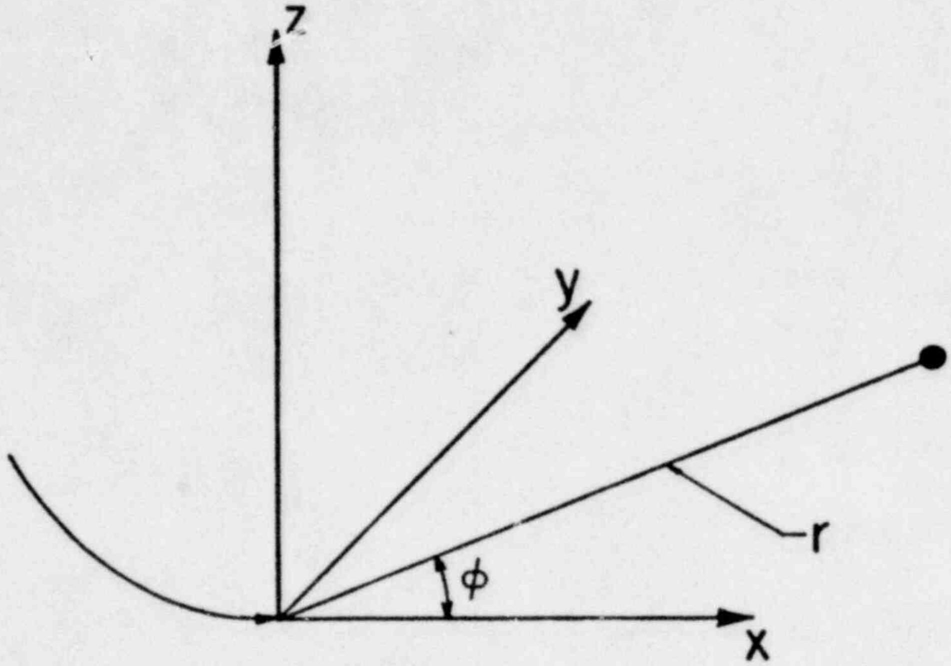

Figure 12. Coordinate system used to calculate force and moment coefficients.

drag coefficient of 1.2 for an infinite circular cylinder in a uniform stream. The measured drag coefficient for the cylindrical portion of the present model is 1.1 which compares quite favorably with Sachs' result. The fact that the present measurements are carried out in a shear flow is a likely explanation for the slightly lower value of the drag coefficient. Also, the present results suggest that the side-force coefficient (C_{F_y}) increases as the radial location of the model r decreases until vortex attachment occurs. Also, as r decreases, the vertical force coefficient (C_{F_z}) increases while the overturning moment decreases.

These results suggest that the likely mode of structural failure changes as the vortex moves closer to the model. Away from the convection zone, the tornadic winds exert a net horizontal force and an overturning moment that would cause an overturning, or "blown-over", mode of failure. However, if the vortex is sufficiently close to the structure that vortex attachment occcurs, the net force and moment on the structure remain approximately the same. However, the local suction pressure forces become rather large when vortex attachment occurs. This suction force could cause the structure to fail in a "bursting" mode as a consequence of the large pressure difference across the wall of the structure. The transition from the overturning mode to the bursting mode should occur when vortex attachment takes place, that is, when the cylindrical structure is at the edge of the vortex core.

A Potential Flow Model

The origins of the side force on the cylindrical model can be better understood with a simple potential flow model. To this end, consider the two-dimensional, inviscid, incompressible, irrotational flow past a circular cylinder of radius a as a consequence of a potential vortex/sink at the origin (see Figure 13). Let the complex location of the circular cylinder be given by ζ_o (= $r_o e^{i\eta_o}$). Then the complex potential W for this flow is given by

$$W = \left(\frac{q}{2\pi} + \frac{i\gamma}{2\pi}\right)\ln \zeta + \left(\frac{q}{2\pi} - \frac{i\gamma}{2\pi}\right)\ln \left(\frac{a^2}{\zeta_o - \zeta} - \zeta_o^{\star}\right) \tag{11}$$

where here q and γ are the strengths of the sink and vortex, respectively. The complex variable $\zeta = re^{i\eta}$ and the notation $()^{\star}$ refers to the complex conjugate. The complex potential W is related to the velocity potential Φ and streamfunction Ψ by

$$W = \Phi + i\Psi \tag{12}$$

We can rewrite Eq. (12), omitting an irrelevant constant,

$$W = \left(\frac{q}{2\pi} + \frac{i\gamma}{2\pi}\right)\ln \zeta + \left(\frac{q}{2\pi} - \frac{i\gamma}{2\pi}\right)\ln \left(\zeta - \zeta_o + \frac{a^2}{\zeta_o^{\star}}\right) - \left(\frac{q}{2\pi} - \frac{i\gamma}{2\pi}\right)\ln (\zeta - \zeta_o) \tag{13}$$

This shows that the vortex of strength γ at the origin induces a vortex of strength $-\gamma$ at the point $(\zeta_o - a^2/\zeta_o^{\star})$ -- the inverse point of the origin in the cylinder -- and a vortex of strength γ at the center of the cylinder.

Taking the real or imaginary part of the expression for W and differentiating, we can calculate the velocity field and, using the Bernoulli equation, the pressure. Figure 13 shows the resulting surface pressure coefficient for the case $a/r_o = 0.075$, corresponding to the cylinder being in the convergent zone, and two values of the swirl angle ϕ (0°,45°). While the experimental results in the leeward separated flow region are not accurately reproduced by this ideal flow model, the forward region including the asymmetry due to the nonuniform flow are reasonably reproduced by this simple model.

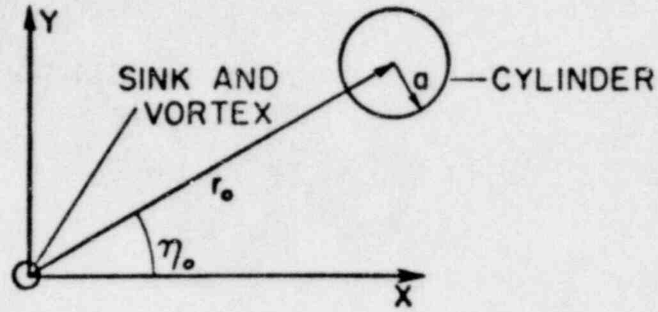

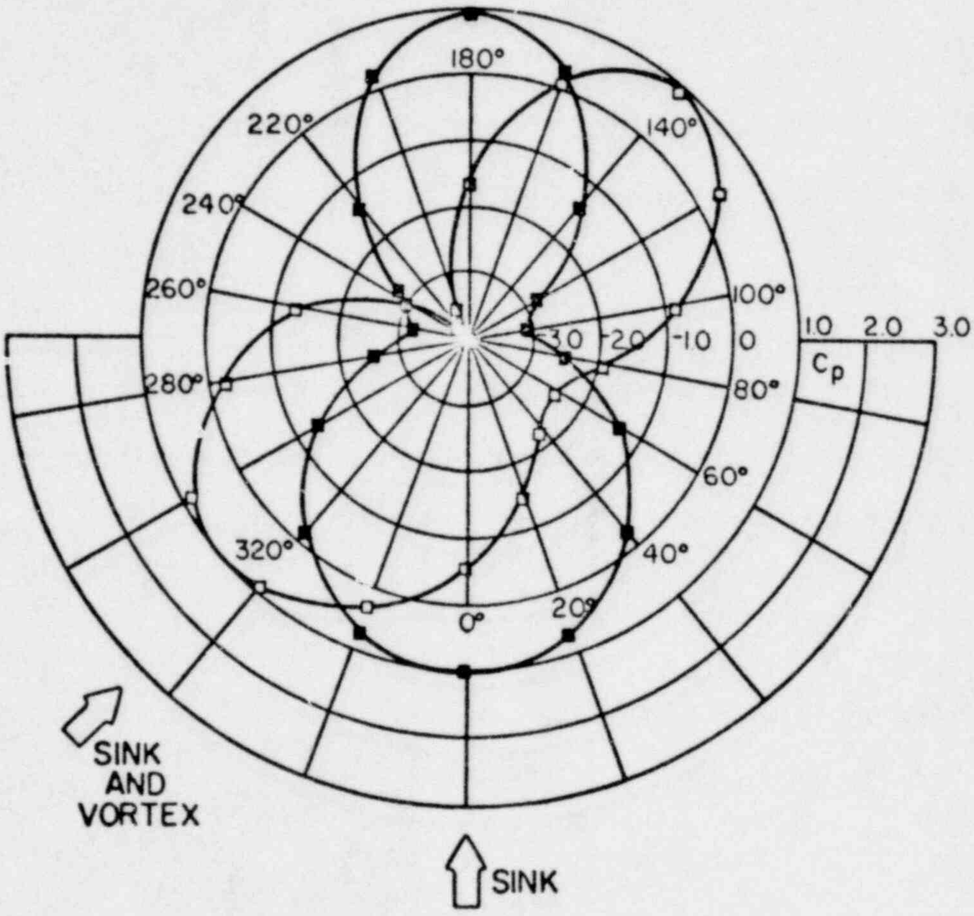

Figure 13. Surface pressure coefficient for ideal flow past an infinite circular cylinder due to a combined sink and vortex at the origin (■ , $\phi=0^0$; □ , ϕ=45 ; a/r_o=0.075).

The methods of potential flow theory can be used to calculate the force per unit length f on the cylinder. Blausius' theorem gives

$$f_x - if_y = \frac{i}{2} \rho \oint_C \left(\frac{dW}{d\zeta}\right)^2 d\zeta \tag{14}$$

where f_x and f_y are the force per unit length in the x and y direction, respectively. Substituting Eq. (11) for W and using residue theory, we obtain the following result for the complex force per unit length

$$f_x - if_y = 2\pi \rho V_o^2 \frac{a^2 r_o}{r_o^2 - a^2} e^{i(\pi - \eta_o)} \tag{15}$$

where V_o is the total velocity at the center of the cylinder, in the absence of the cylinder. The total force per unit length is thus given by

$$f = 2\pi \rho V_o^2 \frac{a^2 r_o}{r_o^2 - a^2} e^{i(\pi + \eta_o)} \tag{16}$$

and, as this result shows, is always directed toward the origin. Consequently, we obtain a side force, f reckoned with respect to the local flow direction ϕ at the cylinder, which is given by

$$f = 2\pi \rho V_o^2 \frac{a^2 r_o}{r_o^2 - a^2} \sin \phi \tag{17}$$

The side force coefficient then is

$$C_f = \frac{f}{\rho V_o^2 a} \tag{18}$$

$$= 2\pi \frac{a\, r_o}{r_o^2 - a^2} \sin \phi \tag{19}$$

which takes on the value 0.34 when $a/r_o = 0.075$ and $\phi = 45°$ corresponding to experimental conditions in the convergent zone. This is to be compared with an experimental value of 0.11. When a/r_0 = .125 and ϕ = 45°, the theoretical value of 0.56 is to be compared with an experimental value of 0.46. While the numerical comparison is not particularly good, largely because the actual flow is a separated one*, the trend of increasing side force coefficient with increasing a/r_0 is reproduced by the theory. More importantly, this calculation shows that the side force arises from the nonuniform pressure distribution on the cylinder which is a consequence of the nonuniform velocity field induced by the sink/vortex at the origin.

* It would be possible to change the strength of the image vortex at the center of the cylinder in such a way as to force agreement between experiment and theory and still have a potential flow which satisfies the inviscid boundary conditions. However, this empiricism would add little to one's basic understanding of the flow.

CHAPTER V

RECTANGULAR MODEL

The model used for these experiments is a rectangular prism -- the geometry typically used to house the power generating turbines employed in nuclear power plants. A typical turbine building is 74 meters long, 42 meters wide, and 37 meters high. Again using a tornado core radius of approximately 50 meters as a basis for the scaling, the dimensions of the scaled turbine building model are 0.254 m long, .146 m wide, and .127 m high. A drawing of the model is shown in Figure 14 along with the location of the 60 surface pressure ports. The numbering scheme used to locate the ports is shown in Figure 15.

Measurements of the time-averaged surface pressure have been made for three model locations and two imposed swirl angles ($\phi=0°,45°$). With zero imposed swirl, three different orientations ($\theta=0°,45°,90°$) of the model with respect to the ambient velocity direction were examined. Figure 16 illustrates the various orientations. When the imposed swirl angle is 45°, four different orientations ($\theta=0°,45°,90°,135°$) of the model were used as illustrated in Figure 16. As a consequence, there are twenty-one different cases depending upon model location, model orientation and imposed swirl. To simplify the presentation of the data, these cases have been numbered 1-21. Table 6 gives the conditions associated with each case. The pressure coefficient data is presented graphically in Figures 17-37 and in tabular form in Tables 7-12.

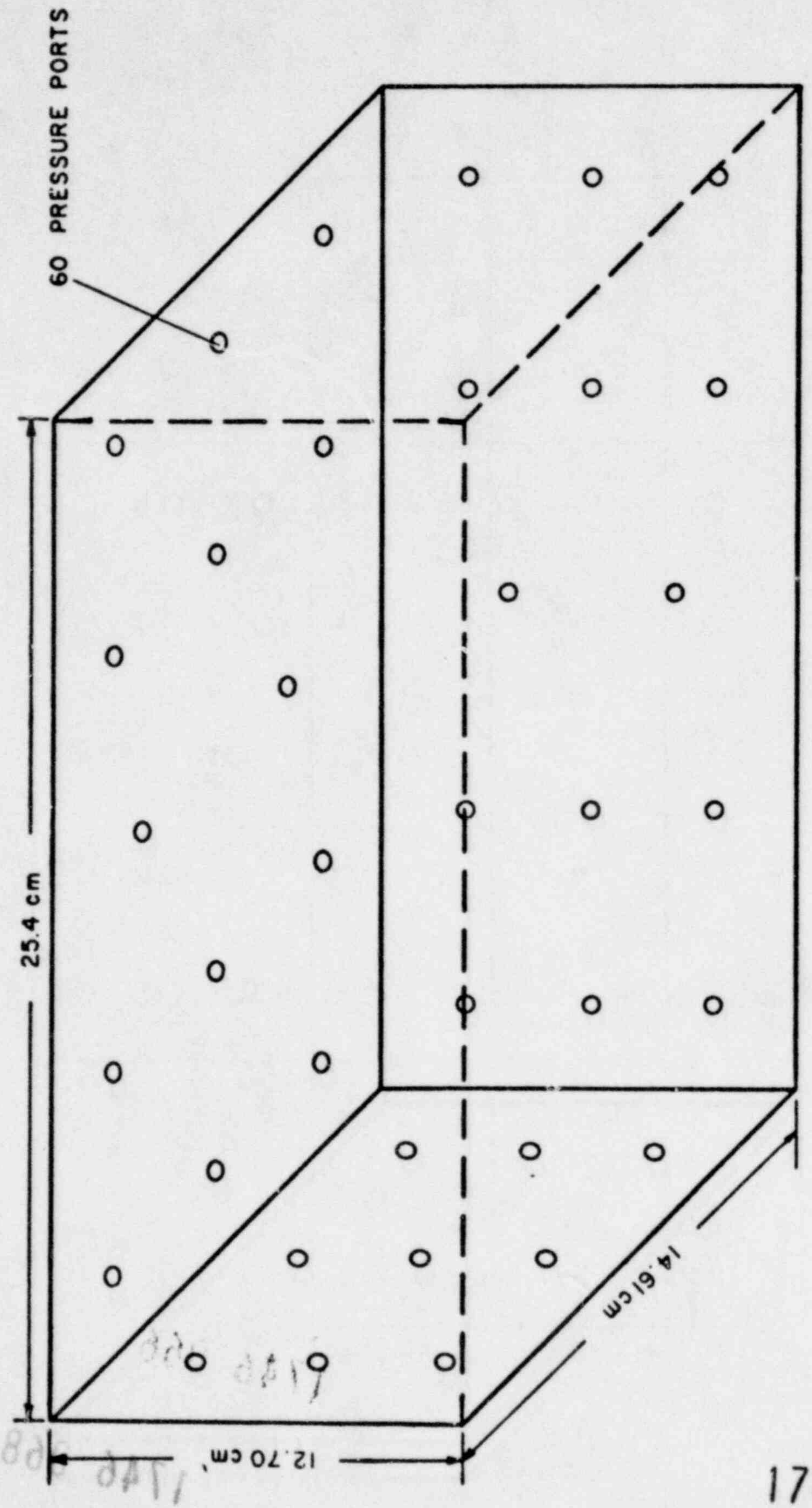

Figure 14. Schematic of rectangular model with pressure port locations.

1746 067

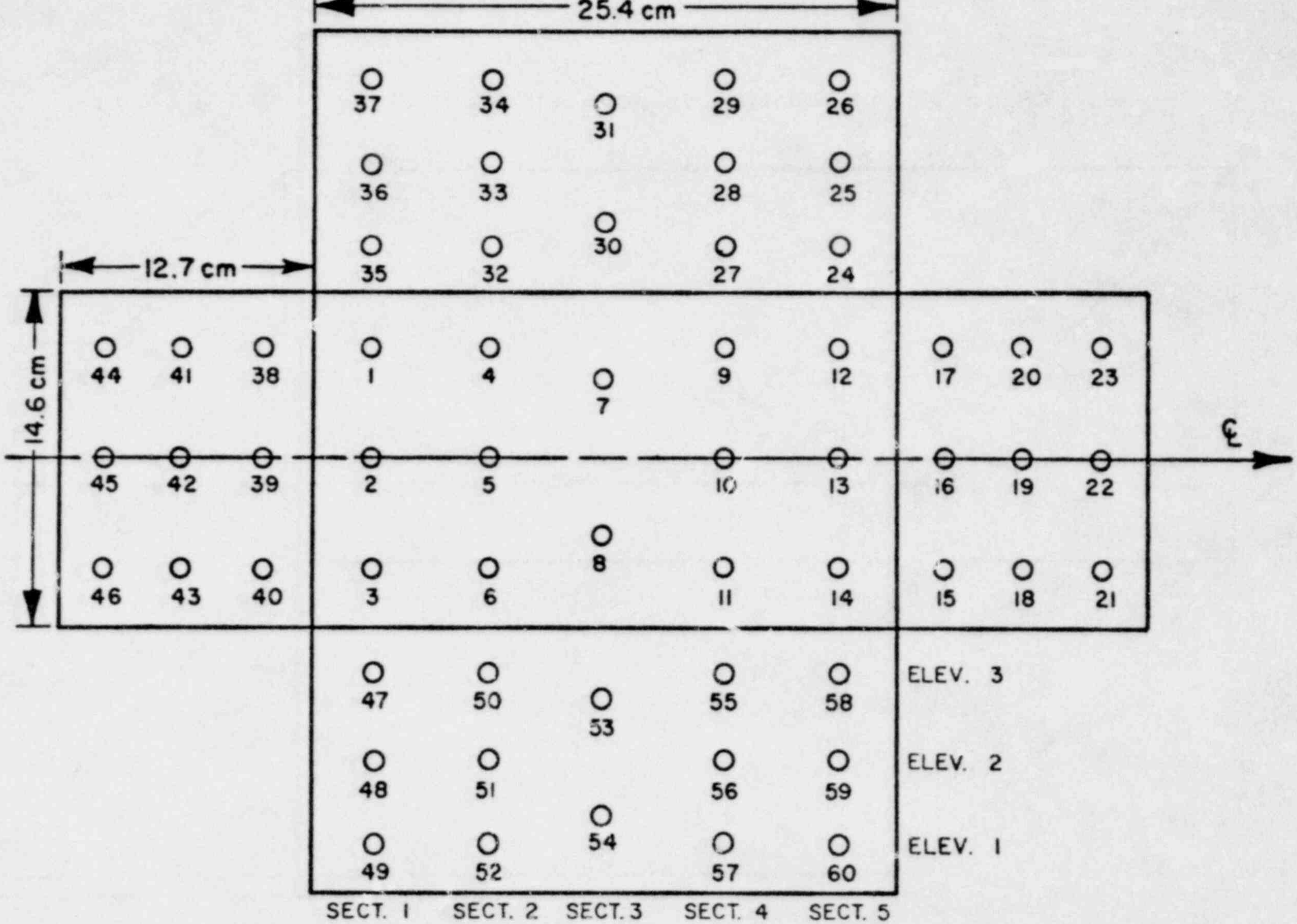

Figure 15. Numbering scheme to identify pressure ports on rectangular model.

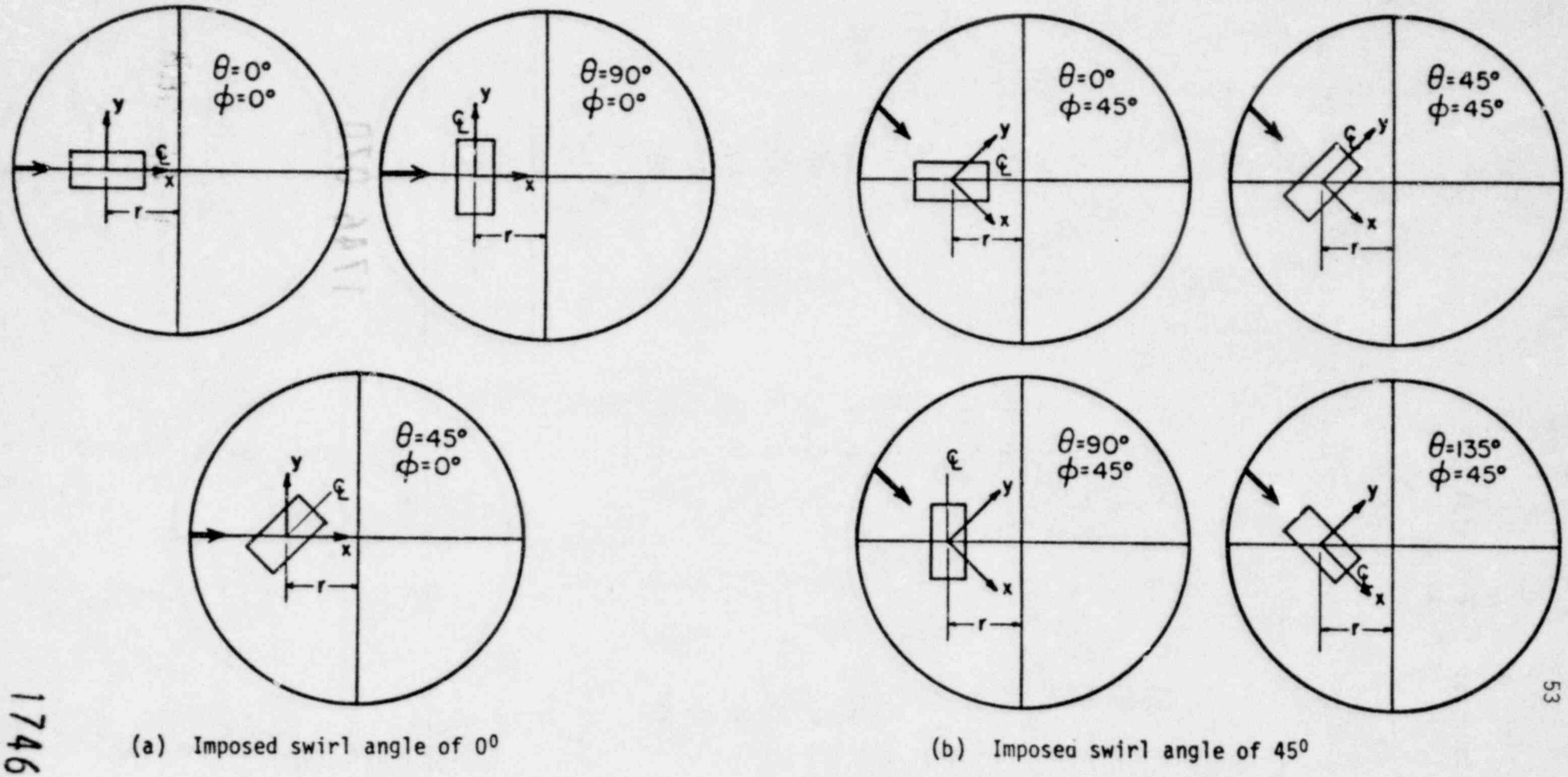

Figure 16. Various rectangular model orientations.

Table 6. Experimental conditions for rectangular model measurement cases 1-21

Case	Imposed Swirl Angle ϕ	Model Location (m)	Model Orientation θ
1	0°	0.762	0°
2	0°	0.762	45°
3	0°	0.762	90°
4	0°	0.457	0°
5	0°	0.457	45°
6	0°	0.457	90°
7	0°	0.114	0°
8	0°	0.114	45°
9	0°	0.114	90°
10	45°	0.762	0°
11	45°	0.762	45°
12	45°	0.762	90°
13	45°	0.762	135°
14	45°	0.457	0°
15	45°	0.457	45°
16	45°	0.457	90°
17	45°	0.457	135°
18	45°	0.114	0°
19	45°	0.114	45°
20	45°	0.114	90°
21	45°	0.114	135°

1746 070

Pressure Coefficient

Figure 17a and Table 7a show the pressure coefficient results for zero imposed swirl (ϕ=0°) in the convergent zone with the model oriented parallel to the flow (θ=0°) In this and the other figures that follow, the experimental data, denoted by circles, have been joined by straight lines to emphasize the distribution of the surface pressure. Also, these data are presented for five vertical planes along the model (x/l=.10,.30, .50,.70, and .90) and three horizontal planes (z/h=.167,.50, and .833). The results in Figure 17 show good symmetry with respect to the flow direction. Relatively high pressures are obtained on the upwind face. The lowest pressures are achieved just downstream of the corners (see e.g. ports 1,2,3; 35,36,37; 47,48,49; 15,16,17; 18,19,20; 21,22,23). These results are not unlike those obtained in the usual boundary-layer-type winds. Although the flow past the model is accelerating, the gross features of the pressure distribution on the model is determined largely by the separation that takes place at the sharp corners of the model.

Figure 17b and Table 7b give results for zero imposed swirl (ϕ=0°)in the convergent zone with the model oriented at 45° to the local radial direction. This quartering wind produces rather low pressures near the windward corner of the roof. The pressure coefficient at port 4 is -1.85. Also, relatively low pressures are obtained on the leeward side of the model (ports 47-52).

The effect of orienting the model at right angles to the radial direction (θ=90°) with zero imposed swirl (ϕ=0°)in the convergent zone is shown in Figure 17c and Table 7c The measured pressure distribution is reasonably symmetric and not unlike that obtained with θ=0°. The pressure coeffici just downstream of the windward corners is somewhat lower in the present case than in case 1 (e.g. at port 41, C_p = - 0.97 for case 3 while C_p = - 0.78 at port 47 for case 1).

Moving the model to the boundary of the convergent and convection zones (r = 0.457 m) does not radically change the shape of the pressure coefficient distribution for the case of no imposed swirl. As Figures 18a -18c and Tables 8a -8c show, however, the magnitude of the pressure coefficient decreases as one moves from the convergent zone (r = 0.762 m) to the boundary of the convergent and convection zones (r = 0.457 m). The updraft imposed on the flow in the convection zone is largely responsible for this change.

Placing the model in the convection zone (r = 0.114 m) where,with zero imposed swirl, it is then embedded in a separated flow region, reduces the pressure coefficient further while the shape of the pressure distribution remains similar to that in the convergent zone and at the boundary of the convergent and convection zones. Figures 19a -19c and Tables 9a -9c show the data for the cases of zero imposed swirl in the convection zone with the model oriented at 0°,45°, and 90° to the radial direction, respectively.

Figures 20-23 and Tables 10-12 show the effects of swirl on the surface pressure coefficient - in all cases, the imposed swirl angle ϕ is 45°. Figure 20a and Table 10a show the data obtained for case 10 when the model is in the convergent zone (r = 0.762 m) and is parallel to the local radial direction (θ=0°). These results for θ=0°and ϕ=45° are rather similar to thos obtained in case 2 where θ=45° and ϕ=0°. However, the base pressure in case 10 is lower than in case 2. Also, the pressure on the shorter windward face, which includes ports 38-46, is less in the swirling flow (case 10) than the non-swirling flow (case 2). Finally, in the swirling flow case, there is evidence of flow reattachment and a pressure recovery on the leeward face (see port 57). Smoke visualization studies also suggest that the streamline curvature in the swirling flows can cause reattachment downstream of a sharp corner.

Pressure coefficient data for the case where there is imposed swirl (ϕ=45°) and the model is oriented at 45° to the radial direction is shown in Figure 20b and Table 10b Here the effects of swirl become more pronounced. Comparing Figure 17c (case 3, θ=90°, ϕ=0°) and Figure 20b (case 11, θ=45°, ϕ=45°), where in both cases the model is normal to the flow, we see that the imposed swirl causes significant asymmetries. The leeward face (ports 47-60) has a much lower pressure in the swirling flow case thereby inducing a higher drag force reckoned with respect to the local wind direction. Also, the lower pressure on the leeward short face (ports 35-46) causes a side force. The relatively low pressure coefficients just downstream of the upstream corner of this face (see e.g. port 38) make this location a likely point at which the cladding of a structure can come loose.

Figure 20c and Table 10c show data for case 12 in which the imposed swirl angle ϕ is 45° and the model is oriented at 90° to the local radial direction. The results are quite similar to those obtained for case 10 (ϕ=45°, θ=0°) except that the pressure on the windward short face is somewhat higher in case 12.

Figure 20d and Table 10d show the results obtained in case 13 with the model oriented at 135° relative to the radial direction and the imposed swirl angle ϕ equal to 45°. These results are to be compared with those in Figure 17a in which the model is similarly aligned with the flow (case 1; θ=0°, ϕ=0°). This comparison shows the results to be rather similar although the windward face has a somewhat higher pressure coefficient in case 13 than in case 1 while the base pressure is lower in case 13 than in case 1. As a consequence, the drag force in case 13 is higher than that in case 1 by about 25%. Also, the imposed swirl in case 13 introduces a slight asymmetry in the pressure distribution which leads to a small side force.

Figures 21a 21d and Tables 11a 11d give the pressure coefficient distributions with the model at the boundary between the convergent and convection zones ($r = 0.457$ m) and with the imposed swirl ϕ set at 45°.

The results for case 14 ($\phi=45°$, $\theta=0°$) are shown in Figure 21a and Table 11a Comparing these results with those obtained under the same conditions in the convergent zone (case 10, Figure 20a) shows that, with three exceptions, the pressure distributions are rather similar. First, the pressure coefficients obtained at ports 38, 41, and 44 in case 14 are negative whereas in case 10 they are positive. We believe this is due to the intensification of the vorticity created at the sharp corner upstream of these ports in case 14 as a consequence of the imposed vertical velocity at the edge of the updraft region. Second, the base pressure in case 14 (see ports 15-23) is lower than in case 10 by almost forty percent. Finally, the minimum pressure coefficient on the roof of the model is -3.47 at port 4 in case 14 while the minimum value in case 10, which also occurs at port 4, is -2.69. This is a twenty-nine percent decrease in the pressure coefficient and suggests that a very strong suction force occurs around port 4. In this quartering wind condition, the pair of counter-rotating vortices which are shed off the windward corner of the building are further intensified by the vertical velocity imposed in the updraft region. This vortex stretching mechanism intensifies the corner vortices and, while present in the convergent radius vector. These results are similar to those obtained in case 10 ($\theta=0°,\phi=45°$) except that the magnitude of the suction on pressures obtained on the roof and on the leeward sides of the model are lower in case 16 than in case 10.

Surface pressure coefficients for case 17 ($\theta=135°$, $\phi=45°$) are given in Figure 21d and Table 11d. Except for the slight asymmetry due to the imposed swirl and the somewhat lower base pressure, these results are quite like those of case 4 ($\phi=0°,\theta=0°$).

Figure 22a-22d and Tables 12a-12d give the data obtained in the convection zone (r = 0.114 m) with swirl ($\phi=45$). The effect of swirl in these cases is rather dramatic. The model is no longer embedded in a low velocity, separated flow region but is in a swirling, higher speed flow region. Consequently, the magnitude of the surface pressure coefficient increases substantially, although the maximum values are still well below those experienced at the boundary between the convection and convergent zones. Figures 22a-22d and Tables 12a-12d give results for $\phi=45°$ and $\theta=0°,45°$, $90°$, and $135°$, respectively. The pressure distributions shown in these figures are not unusual or dramatic and thus we shall not discuss them in detail.

Force and Moment Coefficients

The force and moment coefficients for the twenty-one cases have been computed using Eqs. (9) and (10). In this case, the reference area A has been taken to be the frontal area when $\theta=\phi=0°$(e.g. the area of the smallest vertical face). The reference length is taken to be the height of the model.

Table 13 gives the force and moment coefficients calculated from the zone, is enhanced as the model is moved into the convection zone. This is another manifestation of the differences between the usual boundary-layer-type wind results and results obtained in a vortical, tornado-like flowfield.

Figure 21b and Table 11b give results for case 15 corresponding to θ=45°, ϕ=45° at the boundary of the convergent and convection zones. The corresponding case in the convergent zone is case 11. As these results show, the pressure distribution is rather different. In particular, the peak suction pressures which occur on the leeward face are extremely low. The pressure coefficient at port 53 in case 15 is -6.00, which is almost a factor of three lower than the minimum pressure coefficient of -2.20 in case 11 (which occurs at port 48). Thus, extremely low suction pressures occur in this case on the leeward side of the model. In fact, the value -6.00 at port 53 is the most extreme condition we have observed in our steady-state measurements. Other relatively high suction pressures also occur at ports 13 (-2.89), 47 (-3.58), 48 (-3.35), and 55 (-3.71). Thus, a structure placed near the edge of the updraft of a tornadic storm will experience local suction pressure forces which could cause a wall or roof to come loose and, once loosened, the high tornadic winds would then tend to tear the wall or roof loose from the structure. As these measurements show, the vortical nature of the tornadic winds makes the initiating phenomenon for this failure mode more intense than it would be in a non-vortical flow. These results also imply that a tornado's capacity for damage is characterized by more than the maximum windspeed. Location with respect to the tornado vortex and orientation are also important factors.

Figure 21c and Table 11c give results for case 16 in which the imposed swirl angle is 45° and the model orientation is 90° with respect to the local

Table 13, Force and moment coefficients for rectangular model

CASE	C_{Fx}	C_{Fy}	C_{Fz}	C_{Mx}	C_{My}	C_{Mz}
1	1.54	0.02	0.95	0.00	0.80	0.02
2	3.19	-1.08	2.00	0.61	1.65	0.35
3	2.53	0.00	1.93	-0.01	1.40	0.03
4	0.59	0.01	0.93	-0.01	0.42	0.01
5	1.32	-0.45	1.48	0.23	0.74	0.22
6	1.46	-0.01	1.51	0.00	0.77	0.00
7	0.01	0.00	0.08	0.00	0.01	0.00
8	0.03	-0.02	0.10	0.01	0.02	0.01
9	0.03	0.00	0.09	0.00	0.02	0.00
10	3.55	-1.30	2.37	1.14	1.79	0.42
11	4.08	-0.93	2.40	0.53	2.40	0.32
12	3.44	0.48	1.40	-0.20	1.73	0.10
13	1.91	-0.26	0.95	0.16	1.11	0.27
14	3.85	-1.26	3.31	1.39	1.88	0.29
15	5.90	-1.33	3.65	0.93	3.45	0.60
16	3.04	0.36	1.81	0.05	1.67	0.01
17	1.96	-0.53	1.36	0.41	0.99	0.47
18	0.75	0.18	1.03	0.42	0.06	0.30
19	1.02	1.35	1.15	0.55	0.52	0.37
20	0.85	0.25	1.10	0.10	0.45	0.55
21	0.87	0.14	1.02	0.15	0.01	0.50

1746 077

measured pressure coefficients. The axes to which these coefficients refer are shown in Figure 16. Briefly, the x-axis is in the direction of the oncoming flow and thus C_{F_x} gives the drag force. The y-axis is normal to this direction and parallel to the ground; C_{F_y} is thus the side force. The z-axis is normal to the ground and C_{F_z} gives the vertical force on the roof.

The results for cases 1-3, in the convergent zone without swirl, can be compared with other published values. Table 14 gives a comparison of the results presented by Sachs [27] for ordinary boundary-layer-type winds.

Table 14. Comparison of the present results with Sachs (ref. 27)

	Case 1 ($\theta=0°,\phi=0°$)	Case 2 ($\theta=45°,\phi=0°$)	Case 3 ($\theta=90°,\phi=0°$)
C_{F_x} (Present)	1.54	3.19	2.53
C_{F_x} (ref. 27)	.90	1.68	2.52
C_{F_y} (Present)	.02	1.08	0
C_{F_y} (ref. 27)	0	.84	0

The comparison of the present results with those reported by Sachs are remarkably good when $\theta=90°$ corresponding to the case where the long side of the rectangular prism is normal to the flow. However, when the orientation angle is decreased to 45° or 0°, the comparison becomes rather poor, with the present measurements giving values for the drag coefficient (C_{F_x}) that are high by 71% for $\theta=0°$ and 90% for $\theta=45°$. These differences are likely to be due to the nonuniformity of the flow in which the model is embedded. That is, in the absence of the model, the velocity in the convergent zone is inversely proportional to distance. Thus, in contrast to the uniform flow conditions in the measurements reported by Sachs [27], the flow in the present measurements is lower on the windward face and higher on the leeward face, relative to the value that occurs at the center of the model, in the absence of the model. The lowered velocity on the windward face will increase the pressure there whereas the higher velocity on the leeward face will decrease the pressure. Consequently, the nonuniform flow conditions should act to increase the drag, as has been observed, and should become more important as the orientation of the model is decreased from 90°. As the orientation of the model decreases from 90°, the effect of the nonuniform velocity field in the convergent zone should be most pronounced when the diagonal of the rectangular planform is in the radial direction (here when $\theta = \tan^{-1}(.146/.254) = 30°$) corresponding to the case where the radial distance from the closest to the furthest point on the model is a maximum. This would explain why the differences between the present results and those of Sachs are largest when $\theta=45°$.

Comparing the present results for the force coefficients in cases 1-3 with those in cases 10-13 shows that the effect of swirl in the convergent zone is to increase all three components of the force. For example, looking at cases 1 and 13, we see an increase in the drag coefficient of twenty-four percent. The horizontal force coefficient for case 2 is 3.19 while that for case 10 is 3.55, an increase of eleven percent. The horizontal force coefficient for case 3 is 2.53 while that for case 11 is 4.18, a sixty-five percent increase. Clearly, the effect of swirl is to make the net force on the structure larger. Similarly, the effect of swirl is to increase the moment coefficients. Comparing cases 3 and 10, we see that the horizontal overturning moment increases by fifty-two percent.

A similar, but more striking, trend occurs at the boundary of the convergent and convection zones. Cases 4-6 give the zero swirl results while cases 12-15 give the force and moment coefficients with swirl. For example, comparing case 15, for which the drag coefficient has its largest value of 5.90, with case 6, we see that the horizontal force coefficient increases by a factor of 4.04 while the overturning moment coefficient C_{M_y} increases by a factor of 4.48. The vertical force coefficient increases from 1.51 to 3.65, a factor of 2.42,with the addition of swirl. Also, the effect of swirl is to increase the vertical twisting moment, although in no case was this moment the largest acting on the structure. Clearly, the effect of swirl is to significantly alter the pressure distribution on the model and thereby dramatically increasing the forces and moments on the structure.

This trend of increased force and moment coefficient with swirl also occurs in the convection zone (compare cases 7-9 and 18-21). However, the resulting coefficients are all smaller than those at the boundary of the convergent and convection zones.

Table 7a. Surface pressure coefficient on the rectangular model in the convergent zone ($r = 0.762m$) with imposed swirl angle of 0^0 (Case 1, orientation angle of 0^0).

Port	1	2	3	4	5	6	7	8	9	10
C_p	-0.84	-0.81	-0.81	-0.25	-0.38	-0.30	-0.20	-0.23	-0.44	-0.38
Port	11	12	13	14	15	16	17	18	19	20
C_p	-0.42	-0.65	-0.58	-0.64	-0.75	-0.74	-0.75	-0.77	-0.74	-0.78
Port	21	22	23	24	25	26	27	28	29	30
C_p	-0.76	-0.78	-0.78	-0.48	-0.42	-0.44	-0.28	-0.23	-0.24	-0.13
Port	31	32	33	34	35	36	37	38	39	40
C_p	-0.08	-0.22	-0.23	-0.32	-0.71	-0.68	-0.67	0.73	0.77	0.72
Port	41	42	43	44	45	46	47	48	49	50
C_p	0.78	0.83	0.80	0.81	0.82	0.78	-0.78	-0.71	-0.70	-0.20
Port	51	52	53	54	55	56	57	58	59	60
C_p	-0.22	-0.24	-0.14	-0.08	-0.22	-0.20	-0.17	-0.42	-0.44	-0.40

Table 7b. Surface pressure coefficient on the rectangular model in the convergent zone (r = 0.762m) with imposed swirl angle of 0^0 (Case 2, orientation angle of 45^0).

Port	1	2	3	4	5	6	7	8	9	10
C_p	-0.38	-1.16	-1.48	-1.85	-0.44	-0.63	-1.45	-0.60	-1.18	-1.15
Port	11	12	13	14	15	16	17	18	19	20
C_p	-0.68	-1.07	-0.97	-0.88	-0.95	-0.88	-0.87	-1.02	-0.94	-0.89
Port	21	22	23	24	25	26	27	28	29	30
C_p	-1.06	-0.87	-0.83	0.15	0.25	0.16	0.41	0.52	0.50	0.61
Port	31	32	33	34	35	36	37	38	39	40
C_p	0.77	0.62	0.75	0.83	0.77	0.93	0.98	0.69	0.51	0.25
Port	41	42	43	44	45	46	47	48	49	50
C_p	0.83	0.67	0.38	0.89	0.71	0.32	-1.30	-1.33	-1.30	-1.34
Port	51	52	53	54	55	56	57	58	59	60
C_p	-1.29	-1.29	-1.27	-1.15	-1.19	-1.18	-0.76	-1.02	-1.04	-0.68

1746 082

Table 7c. Surface pressure coefficient on the rectangular model in the convergent zone ($r = 0.762m$) with imposed swirl angle of 0^0 (Case 3, orientation angle of 90^0).

Port	1	2	3	4	5	6	7	8	9	10
C_p	-1.38	-0.73	-0.51	-1.27	-1.15	-0.69	-1.19	-0.90	-1.27	-1.08
Port	11	12	13	14	15	16	17	18	19	20
C_p	-0.67	-1.30	-0.68	-0.57	-0.37	-0.30	-0.95	-0.39	-0.65	-0.91
Port	21	22	23	24	25	26	27	28	29	30
C_p	-0.42	-0.55	-0.75	0.64	0.84	0.67	0.65	0.92	0.89	0.84
Port	31	32	33	34	35	36	37	38	39	40
C_p	0.94	0.67	0.93	0.90	0.71	0.79	0.74	-0.99	-0.30	-0.33
Port	41	42	43	44	45	46	47	48	49	50
C_p	-0.97	-0.59	-0.36	-0.84	-0.53	-0.37	-0.66	-0.68	-0.68	-0.67
Port	51	52	53	54	55	56	57	58	59	60
C_p	-0.68	-0.66	-0.69	-0.62	-0.68	-0.66	-0.63	-0.65	-0.69	-0.70

Table 8c. Surface pressure coefficient on the rectangular model at the boundary of the convergent and convection zones (r = 0.457m) with imposed swirl angle of 0^0 (Case 4, orientation angle of 0^0).

Port	1	2	3	4	5	6	7	8	9	10
C_p	-0.61	-0.64	-0.64	-0.58	-0.56	-0.57	-0.40	-0.39	-0.46	-0.28
Port	11	12	13	14	15	16	17	18	19	20
C_p	-0.45	-0.33	-0.27	-0.34	-0.30	-0.24	-0.30	-0.28	-0.22	-0.28
Port	21	22	23	24	25	26	27	28	29	30
C_p	-0.34	-0.15	-0.30	-0.15	-0.09	-0.10	-0.13	-0.05	-0.03	-0.08
Port	31	32	33	34	35	36	37	38	39	40
C_p	-0.01	-0.17	-0.12	-0.07	-0.52	-0.42	-0.43	0.28	0.28	0.28
Port	41	42	43	44	45	46	47	48	49	50
C_p	0.34	0.38	0.34	0.33	0.36	0.32	-0.51	-0.42	-0.41	-0.17
Port	51	52	53	54	55	56	57	58	59	60
C_p	-0.14	-0.09	-0.07	-0.02	-0.12	-0.04	-0.02	-0.12	-0.09	-0.08

Table 8b. Surface pressure coefficient on the rectangular model at the boundary of the convergent and convection zones (r = 0.457m) with imposed swirl angle of 0^0 (Case 5, orientation angle of 45^0).

Port	1	2	3	4	5	6	7	8	9	10
C_p	-0.68	-0.99	-0.81	-1.12	-0.52	-0.65	-0.88	-0.53	-0.78	-0.71
Port	11	12	13	14	15	16	17	18	19	20
C_p	-0.51	-0.79	-0.74	-0.72	-0.67	-0.53	-0.44	-0.59	-0.41	-0.39
Port	21	22	23	24	25	26	27	28	29	30
C_p	-0.46	-0.37	-0.43	0.03	0.13	0.08	0.11	0.23	0.20	0.20
Port	31	32	33	34	35	36	37	38	39	40
C_p	0.28	0.15	0.29	0.31	0.21	0.34	0.34	0.19	0.11	0.02
Port	41	42	43	44	45	46	47	48	49	50
C_p	0.26	0.18	0.06	0.26	0.20	0.02	-0.65	-0.61	-0.63	-0.73
Port	51	52	53	54	55	56	57	58	59	60
C_p	-0.70	-0.68	-0.64	-0.63	-0.57	-0.43	-0.37	-0.37	-0.22	-0.02

Table 8c. Surface pressure coefficient on the rectangular model at the boundary of the convergent and convection zones ($r = 0.457m$) with imposed swirl angle of 0^0 (Case 6, orientation angle of 90^0).

Port	1	2	3	4	5	6	7	8	9	10
C_p	-0.88	-0.67	-0.63	-0.86	-0.78	-0.63	-0.84	-0.77	-0.87	-0.79
Port	11	12	13	14	15	16	17	18	19	20
C_p	-0.62	-0.90	-0.66	-0.61	-0.26	-0.19	0.60	-0.14	-0.15	-0.55
Port	21	22	23	24	25	26	27	28	29	30
C_p	-0.21	-0.23	-0.49	0.26	0.38	0.34	0.30	0.39	0.43	0.42
Port	31	32	33	34	35	36	37	38	39	40
C_p	0.47	0.31	0.43	0.39	0.26	0.36	0.30	-0.62	-0.21	-0.26
Port	41	42	43	44	45	46	47	48	49	50
C_p	-0.49	-0.16	-0.17	-0.52	-0.26	-0.21	-0.51	-0.71	-0.65	-0.46
Port	51	52	53	54	55	56	57	58	59	60
C_p	-0.54	-0.36	-0.39	-0.26	-0.45	-0.50	-0.38	-0.51	-0.69	-0.64

Table 9a. Surface pressure coefficient on the rectangular model in the convection zone (r = 0.114m) with imposed swirl angle of 0^0 (Case 7, orientation angle of 0^0).

Port	1	2	3	4	5	6	7	8	9	10
C_p	-0.04	-0.04	-0.04	-0.04	-0.05	-0.04	-0.04	-0.05	-0.04	-0.04
Port	11	12	13	14	15	16	17	18	19	20
C_p	-0.05	-0.04	-0.04	-0.03	-0.01	-0.01	-0.01	-0.01	-0.01	-0.01
Port	21	22	23	24	25	26	27	28	29	30
C_p	-0.01	-0.01	-0.01	0.00	0.00	-0.00	0.00	0.00	0.00	0.00
Port	31	32	33	34	35	36	37	38	39	40
C_p	0.00	-0.00	0.00	0.00	-0.01	-0.00	0.00	0.01	0.01	0.00
Port	41	42	43	44	45	46	47	48	49	50
C_p	0.01	0.01	0.01	0.00	0.01	0.00	-0.02	-0.01	-0.01	-0.01
Port	51	52	53	54	55	56	57	58	59	60
C_p	-0.00	0.00	0.00	0.00	-0.00	0.00	0.00	-0.00	0.00	0.00

Table 9b. Surface pressure coefficient on the rectangular model in the convection zone (r = 0.114m) with imposed swirl angle of 0^0 (Case 8, orientation angle of 45^0).

Port	1	2	3	4	5	6	7	8	9	10
C_p	-0.05	-0.05	-0.05	-0.05	-0.06	-0.06	-0.06	-0.07	-0.05	-0.04
Port	11	12	13	14	15	16	17	18	19	20
C_p	-0.06	-0.05	-0.05	-0.03	-0.00	-0.01	-0.01	-0.00	-0.00	-0.01
Port	21	22	23	24	25	26	27	28	29	30
C_p	-0.00	-0.01	-0.01	0.00	0.00	-0.00	-0.00	-0.00	0.00	0.00
Port	31	32	33	34	35	36	37	38	39	40
C_p	0.00	0.00	0.01	0.00	0.00	0.01	0.00	-0.0[illegible]	-0.01	-0.00
Port	41	42	43	44	45	46	47	48	49	50
C_p	0.00	0.00	-0.00	0.00	-0.00	-0.00	-0.04	-0.04	-0.03	-0.05
Port	51	52	53	54	55	56	57	58	59	60
C_p	-0.03	-0.03	-0.01	-0.01	-0.01	-0.01	-0.01	-0.01	-0.01	-0.01

Table 9c. Surface pressure coefficient on the rectangular model in the convection zone ($r = 0.114m$) with imposed swirl angle of 0^0 (Case 9, orientation angle of 90^0).

Port	1	2	3	4	5	6	7	8	9	10
C_p	-0.04	-0.05	-0.04	-0.04	-0.04	-0.05	-0.04	-0.05	-0.04	-0.04
Port	11	12	13	14	15	16	17	18	19	20
C_p	-0.05	-0.04	-0.04	-0.05	-0.00	-0.00	-0.01	0.00	0.00	-0.00
Port	21	22	23	24	25	26	27	28	29	30
C_p	-0.00	-0.00	-0.01	0.00	0.01	-0.00	-0.00	0.00	0.00	0.00
Port	31	32	33	34	35	36	37	38	39	40
C_p	0.00	0.00	-0.00	0.00	0.00	0.01	0.00	-0.01	-0.00	-0.00
Port	41	42	43	44	45	46	47	48	49	50
C_p	-0.00	0.00	-0.00	-0.01	-0.00	-0.00	-0.02	-0.02	-0.02	-0.03
Port	51	52	53	54	55	56	57	58	59	60
C_p	-0.02	-0.02	-0.01	-0.01	-0.02	-0.02	-0.01	-0.03	-0.02	-0.02

Table 10a. Surface pressure coefficient on the rectangular model in the convergent zone ($r = 0.762m$) with imposed swirl angle of 45^0 (Case 10, orientation angle of 0^0).

Port	1	2	3	4	5	6	7	8	9	10
C_p	-0.21	-0.21	-0.97	-2.69	-0.34	-0.67	-2.17	-0.52	-1.76	-1.97
Port	11	12	13	14	15	16	17	18	19	20
C_p	-0.71	-1.57	-1.58	-1.08	-1.28	-1.47	-1.44	-1.48	-1.48	-1.45
Port	21	22	23	24	25	26	27	28	29	30
C_p	-1.68	-1.41	-1.47	0.41	0.51	0.23	0.61	0.85	0.68	0.78
Port	31	32	33	34	35	36	37	38	39	40
C_p	0.87	0.80	1.00	0.93	0.96	1.07	1.05	0.16	0.33	0.03
Port	41	42	43	44	45	46	47	48	49	50
C_p	0.13	0.29	-0.09	0.16	0.27	-0.12	-1.47	-1.55	-1.34	-1.61
Port	51	52	53	54	55	56	57	58	59	60
C_p	-1.67	-1.39	-1.63	-0.89	-1.51	-1.53	-0.09	-1.31	-1.37	-0.27

Table 10b. Surface pressure coefficient on the rectangular model in the convergent zone (r = 0.762m) with imposed swirl angle of 45^0 (Case 11, orientation angle of 45^0).

Port	1	2	3	4	5	6	7	8	9	10
C_p	-1.52	-0.87	-0.50	-1.44	-1.25	-1.02	-1.56	-1.14	-1.83	-0.93
Port	11	12	13	14	15	16	17	18	19	20
C_p	-0.66	-2.25	-0.71	-0.87	-0.39	-0.21	-0.42	-0.25	-0.06	-0.25
Port	21	22	23	24	25	26	27	28	29	30
C_p	-0.25	-0.18	-0.43	0.85	1.07	0.95	0.82	1.03	1.01	0.90
Port	31	32	33	34	35	36	37	38	39	40
C_p	0.92	0.78	0.90	0.83	0.64	0.61	0.53	-1.68	-1.01	-0.69
Port	41	42	43	44	45	46	47	48	49	50
C_p	-1.53	-1.41	-0.80	-1.44	-1.35	-1.11	-2.02	-2.20	-1.89	-2.12
Port	51	52	53	54	55	56	57	58	59	60
C_p	-1.46	-1.08	-2.18	-1.28	-1.90	-1.68	-0.82	-0.99	-0.80	-C.64

Table 10c. Surface pressure coefficient on the rectangular model in the convergent zone ($r = 0.762m$) with imposed swirl angle of 45^0 (Case 12, orientation angle of 90^0).

Port	1	2	3	4	5	6	7	8	9	10
C_p	-1.10	-0.59	-0.79	-1.17	-0.31	-0.78	-0.18	-0.52	-0.51	-0.30
Port	11	12	13	14	15	16	17	18	19	20
C_p	-0.77	-0.61	-1.39	-1.09	0.49	0.77	0.91	0.60	0.88	1.04
Port	21	22	23	24	25	26	27	28	29	30
C_p	0.44	0.82	0.96	0.43	0.65	0.64	0.48	0.59	0.57	0.47
Port	31	32	33	34	35	36	37	38	39	40
C_p	0.51	0.37	0.38	0.35	0.09	0.03	0.00	-1.29	-1.45	-1.49
Port	41	42	43	44	45	46	47	48	49	50
C_p	-1.37	-1.51	-1.44	-1.34	-1.41	-0.99	-1.42	-1.51	-1.48	-1.44
Port	51	52	53	54	55	56	57	58	59	60
C_p	-1.42	-1.28	-1.23	-1.18	-1.08	-1.06	-0.99	-0.91	-0.84	-0.95

Table 10d. Surface pressure coefficient on the rectangular model in the convergent zone ($r = 0.762m$) with imposed swirl angle of 45^0 (Case 13, orientation angle of 135^0).

Port	1	2	3	4	5	6	7	8	9	10
C_p	-0.36	-0.46	-0.68	-0.15	-0.19	-0.53	-0.44	-0.18	-0.42	-0.48
Port	11	12	13	14	15	16	17	18	19	20
C_p	-0.28	-0.74	-0.89	-1.05	1.05	0.98	0.85	1.13	1.06	0.82
Port	21	22	23	24	25	26	27	28	29	30
C_p	1.07	1.01	0.73	-0.76	-0.59	-0.54	-0.66	-0.67	-0.58	-0.22
Port	31	32	33	34	35	36	37	38	39	40
C_p	-0.32	-0.10	-0.13	-0.18	-0.40	-0.21	-0.24	-0.97	-0.98	-0.93
Port	41	42	43	44	45	46	47	48	49	50
C_p	-1.03	-1.09	-0.88	-1.04	-1.07	-0.71	-0.58	-0.48	-0.55	-0.36
Port	51	52	53	54	55	56	57	58	59	60
C_p	-0.22	-0.27	-0.15	-0.09	0.01	0.15	0.06	-0.40	-0.30	-0.21

Table 11a. Surface pressure coefficient on the rectangular model at the boundary of the convergent and convection zones ($r = 0.457m$) with imposed swirl angle of 45^0 (Case 14, orientation angle of 0^0).

Port	1	2	3	4	5	6	7	8	9	10
C_p	-0.49	-0.43	-0.99	-3.47	-0.44	-0.73	-3.08	-0.64	-2.33	-2.48
Port	11	12	13	14	15	16	17	18	19	20
C_p	-1.06	-2.30	-2.29	-2.14	-1.97	-2.04	-1.96	-1.77	-2.04	-1.92
Port	21	22	23	24	25	26	27	28	29	30
C_p	-1.87	-1.94	-2.02	0.43	0.50	0.13	0.47	0.75	0.56	0.72
Port	31	32	33	34	35	36	37	38	39	40
C_p	0.76	0.58	0.85	0.81	0.70	0.82	0.81	-0.46	0.15	-0.11
Port	41	42	43	44	45	46	47	48	49	50
C_p	-0.40	0.17	-0.15	-0.24	0.14	-0.15	-1.46	-1.57	-1.40	-1.90
Port	51	52	53	54	55	56	57	58	59	60
C_p	-1.83	-1.58	-2.43	-0.70	-2.17	-1.16	-0.19	-1.90	-1.42	-0.63

Table 11b. Surface pressure coefficient on the rectangular model at the boundary of the convergent and convection zones (r = 0.457m) with imposed swirl angle of 45^0 (Case 15, orientation angle of 45^0).

Port	1	2	3	4	5	6	7	8	9	10
C_p	-2.01	-1.41	-0.99	-1.75	-1.68	-1.51	-2.20	-1.36	-2.58	-1.28
Port	11	12	13	14	15	16	17	18	19	20
C_p	-1.66	-1.66	-2.89	-2.59	-0.73	-0.18	0.11	-0.43	0.03	0.44
Port	21	22	23	24	25	26	27	28	29	30
C_p	-0.53	-0.03	0.27	0.38	0.64	0.76	0.25	0.54	0.65	0.42
Port	31	32	33	34	35	36	37	38	39	40
C_p	0.58	0.30	0.52	0.54	0.18	0.24	0.28	-1.94	-1.27	-0.78
Port	41	42	43	44	45	46	47	48	49	50
C_p	-1.79	-1.75	-1.05	-1.69	-1.64	-1.43	-3.58	-3.35	-2.61	-5.22
Port	51	52	53	54	55	56	57	58	59	60
C_p	-1.84	-2.04	-6.00	-1.94	-3.71	-3.12	-1.50	-2.21	-1.60	-1.10

Table 11c. Surface pressure coefficient on the rectangular model at the boundary of the convergent and convection zones (r = 0.457m) with imposed swirl angle of 45^0 (Case 16, orientation angle of 90^0).

Port	1	2	3	4	5	6	7	8	9	10
C_p	-1.24	-0.45	-0.71	-1.30	-0.46	-0.68	-0.32	-0.51	-0.48	-0.67
Port	11	12	13	14	15	16	17	18	19	20
C_p	-1.51	-1.31	-1.91	-1.57	0.68	0.72	0.75	0.84	0.95	0.88
Port	21	22	23	24	25	26	27	28	29	30
C_p	0.68	0.83	0.88	-0.47	-0.49	0.22	0.33	0.39	0.37	0.27
Port	31	32	33	34	35	36	37	38	39	40
C_p	0.35	0.14	0.24	0.32	-0.04	-0.04	0.06	-1.18	-1.22	-1.21
Port	41	42	43	44	45	46	47	48	49	50
C_p	-1.21	-1.12	-1.09	-1.12	-1.07	-0.80	-1.14	-1.21	-1.25	-1.18
Port	51	52	53	54	55	56	57	58	59	60
C_p	-1.20	-1.04	-1.29	-1.29	-1.26	-1.30	-1.30	-1.38	-1.30	-1.28

Table 11d. Surface pressure coefficient on the rectangular model at the boundary of the convergent and convection zones (r = 0.457m) with imposed swirl angle of 45^0 (Case 17, orientation angle of 135^0).

Port	1	2	3	4	5	6	7	8	9	10
C_p	-0.46	-0.69	-1.28	-0.20	-0.41	-1.46	-0.20	-0.49	-0.52	-0.55
Port	11	12	13	14	15	16	17	18	19	20
C_p	-0.92	-0.70	-0.89	-0.99	0.69	0.60	0.46	0.86	0.74	0.54
Port	21	22	23	24	25	26	27	28	29	30
C_p	0.85	0.79	0.56	-0.63	-0.64	-0.51	-0.64	-0.62	-0.54	-0.28
Port	31	32	33	34	35	36	37	38	39	40
C_p	-0.45	-0.08	-0.10	-0.19	-0.30	-0.25	-0.28	-1.32	-1.42	-1.35
Port	41	42	43	44	45	46	47	48	49	50
C_p	-1.38	-1.40	-1.09	-1.37	-1.49	-0.80	-0.73	-0.61	-0.61	-0.31
Port	51	52	53	54	55	56	57	58	59	60
C_p	-0.24	-0.31	-0.01	0.01	0.08	0.26	0.22	0.29	0.46	0.36

Table 12a. Surface pressure coefficient on the rectangular model in the convection zone (r = 0.114m) with imposed swirl angle of 45^0 (Case 18, orientation angle of 0^0).

Port	1	2	3	4	5	6	7	8	9	10
C_p	0.29	0.31	0.31	-1.05	0.23	0.18	-0.53	-0.13	-1.83	-0.92
Port	11	12	13	14	15	16	17	18	19	20
C_p	-0.45	-1.17	-1.72	-0.89	-0.64	-0.74	0.11	-0.76	-0.30	0.33
Port	21	22	23	24	25	26	27	28	29	30
C_p	-0.84	0.36	0.53	-0.08	0.20	0.45	0.12	0.43	0.54	0.49
Port	31	32	33	34	35	36	37	38	39	40
C_p	0.61	0.52	0.62	0.64	0.57	0.60	0.63	0.35	0.50	0.47
Port	41	42	43	44	45	46	47	48	49	50
C_p	0.29	0.50	0.45	0.45	0.50	0.49	0.20	0.17	0.21	0.16
Port	51	52	53	54	55	56	57	58	59	60
C_p	0.23	0.22	0.30	0.30	0.16	0.31	0.34	0.08	0.14	0.23

Table 12b. Surface pressure coefficient on the rectangular model in the convection zone (r = 0.114m) with imposed swirl angle of 45^0 (Case 19, orientation angle of 45^0).

Port	1	2	3	4	5	6	7	8	9	10
C_p	0.37	0.31	0.19	-0.82	0.18	-0.06	-0.62	-0.45	-0.62	-0.73
Port	11	12	13	14	15	16	17	18	19	20
C_p	-0.91	-0.45	-2.76	-1.74	-0.64	-0.27	0.32	-0.33	0.24	0.55
Port	21	22	23	24	25	26	27	28	29	30
C_p	0.05	0.45	0.63	0.15	0.42	0.50	0.36	0.46	0.54	0.46
Port	31	32	33	34	35	36	37	38	39	40
C_p	0.55	0.46	0.54	0.59	0.49	0.51	0.56	0.17	0.21	0.34
Port	41	42	43	44	45	46	47	48	49	50
C_p	0.19	0.22	0.27	0.20	0.22	0.29	-0.47	-0.25	-0.32	-0.63
Port	51	52	53	54	55	56	57	58	59	60
C_p	-0.07	-0.10	-0.35	0.16	-0.32	0.11	0.36	-0.06	0.16	0.34

Table 12c. Surface pressure coefficient on the rectangular model in the convection zone ($r = 0.114m$) with imposed swirl angle of 45^0 (Case 20, orientation angle of 90^0).

Port	1	2	3	4	5	6	7	8	9	10
C_p	-0.20	-0.14	-0.35	-0.27	-0.39	-0.65	-0.19	-1.07	0.01	-0.31
Port	11	12	13	14	15	16	17	18	19	20
C_p	-1.59	0.07	-1.27	-1.25	0.21	0.33	0.43	0.40	0.48	0.50
Port	21	22	23	24	25	26	27	28	29	30
C_p	0.54	0.56	0.56	0.18	0.10	0.10	0.36	0.42	0.42	0.45
Port	31	32	33	34	35	36	37	38	39	40
C_p	0.51	0.45	0.49	0.54	0.41	0.42	0.45	-0.11	0.10	0.13
Port	41	42	43	44	45	46	47	48	49	50
C_p	-0.04	-0.04	0.11	-0.05	0.01	0.08	-0.69	-0.64	-0.73	-0.93
Port	51	52	53	54	55	56	57	58	59	60
C_p	-0.53	0.07	-0.13	0.38	0.08	0.39	0.49	0.24	0.45	0.57

Table 12d. Surface pressure coefficient on the rectangular model in the convection zone ($r = 0.114m$) with imposed swirl angle of 45^0 (Case 21, orientation angle of 135^0).

Port	1	2	3	4	5	6	7	8	9	10
C_p	-0.32	-0.96	-1.36	-0.10	-0.74	-2.15	-0.03	-0.96	0.24	0.14
Port	11	12	13	14	15	16	17	18	19	20
C_p	-1.16	0.15	0.10	0.11	0.27	0.48	0.46	0.44	0.50	0.46
Port	21	22	23	24	25	26	27	28	29	30
C_p	0.53	0.53	0.51	0.21	0.22	0.22	0.22	0.22	0.23	0.31
Port	31	32	33	34	35	36	37	38	39	40
C_p	0.28	0.34	0.35	0.38	0.24	0.25	0.30	-0.51	-0.72	-0.34
Port	41	42	43	44	45	46	47	48	49	50
C_p	-0.61	-0.52	-0.02	-0.76	-0.38	0.20	-0.58	-0.46	-0.11	-0.63
Port	51	52	53	54	55	56	57	58	59	60
C_p	-0.11	0.01	0.37	0.53	0.44	0.61	0.61	0.54	0.61	0.64

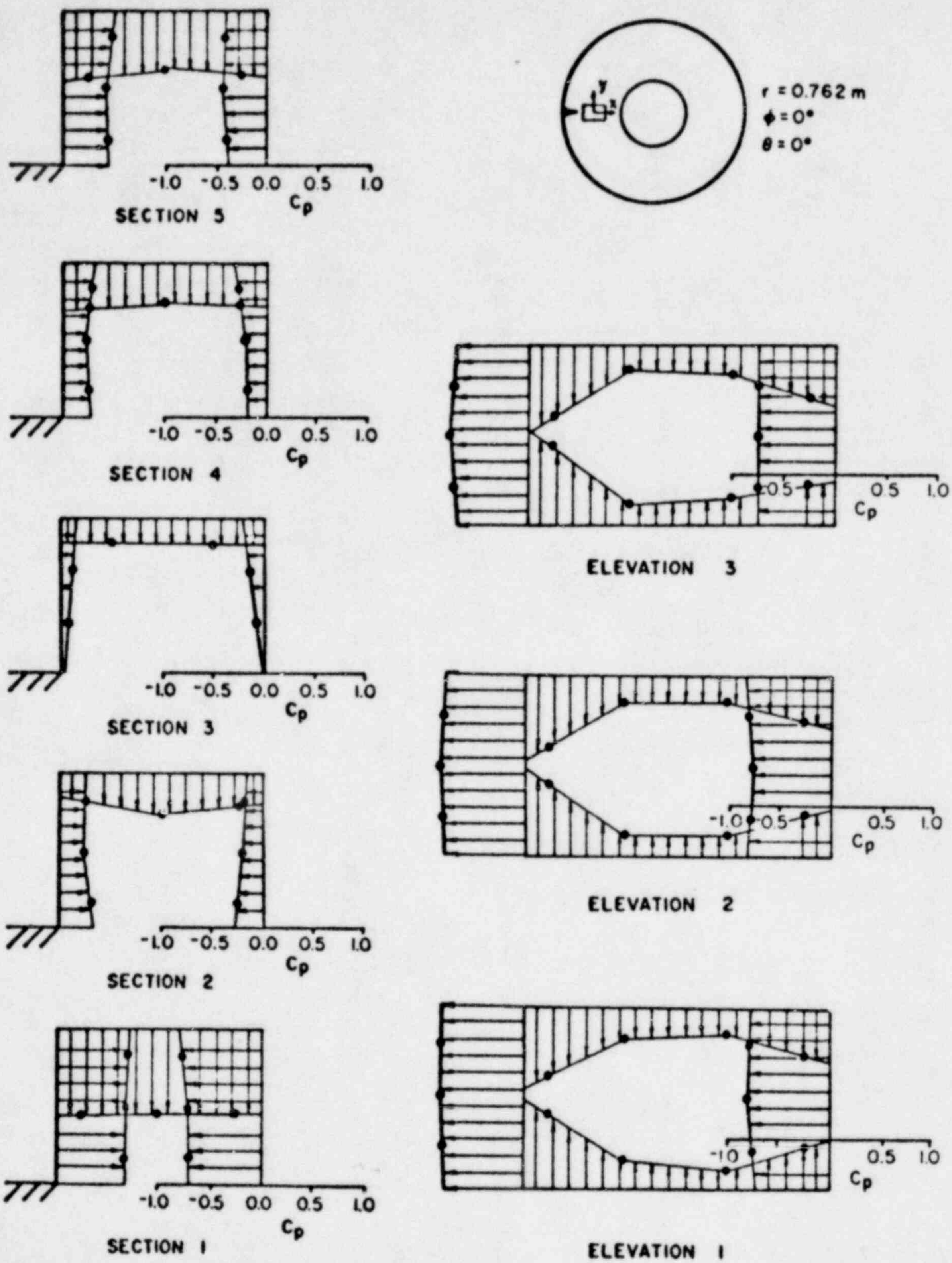

Figure 17a. Surface pressure coefficient on the rectangular model in the convergent zone (r = 0.762m) with imposed swirl angle of 0^0 (Case 1, orientation angle of 0^0).

1746 102

1746 101

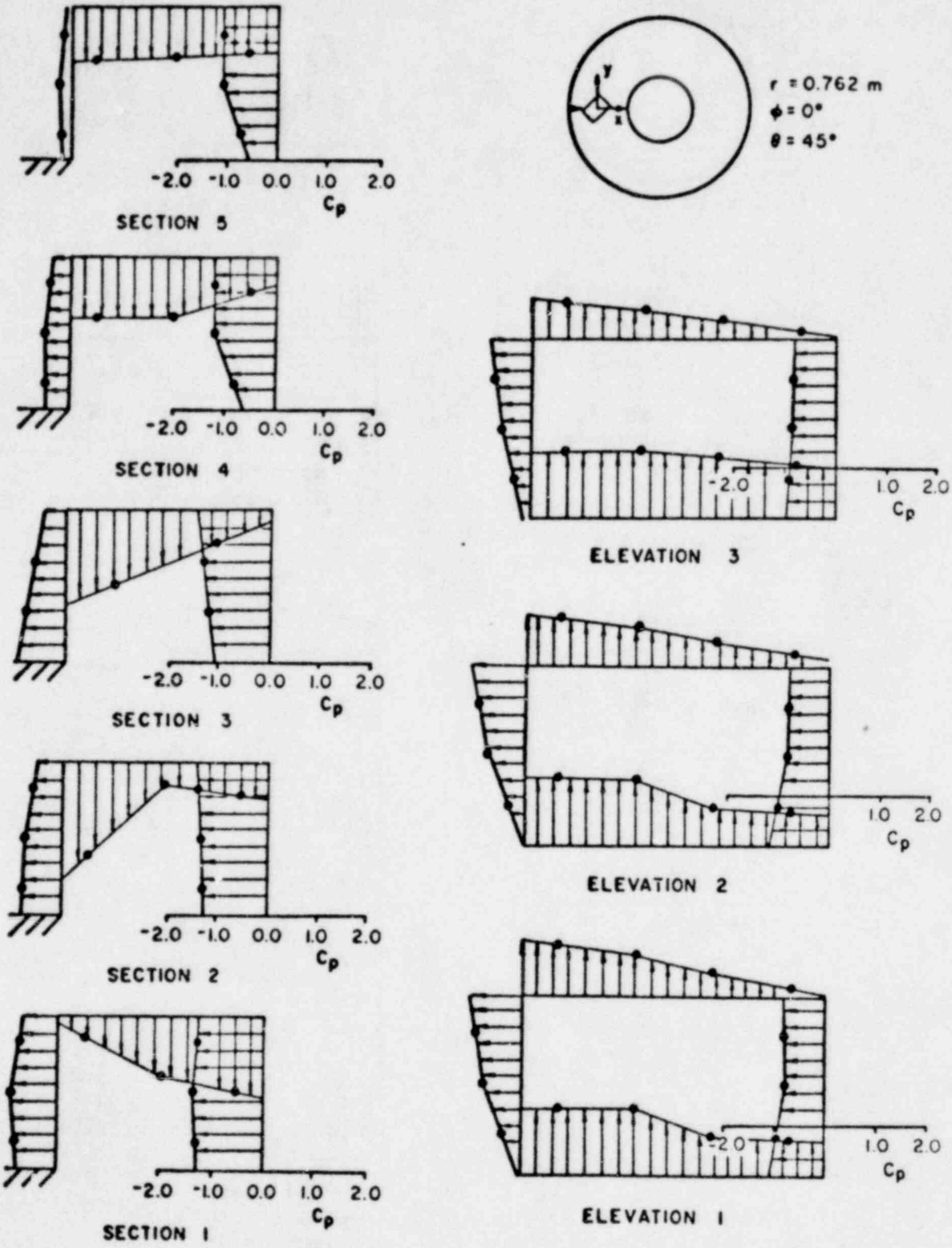

Figure 17b. Surface pressure coefficient on the rectangular model in the convergent zone ($r = 0.762m$) with imposed swirl angle of 0^0 (Case 2, orientation angle of 45^0).

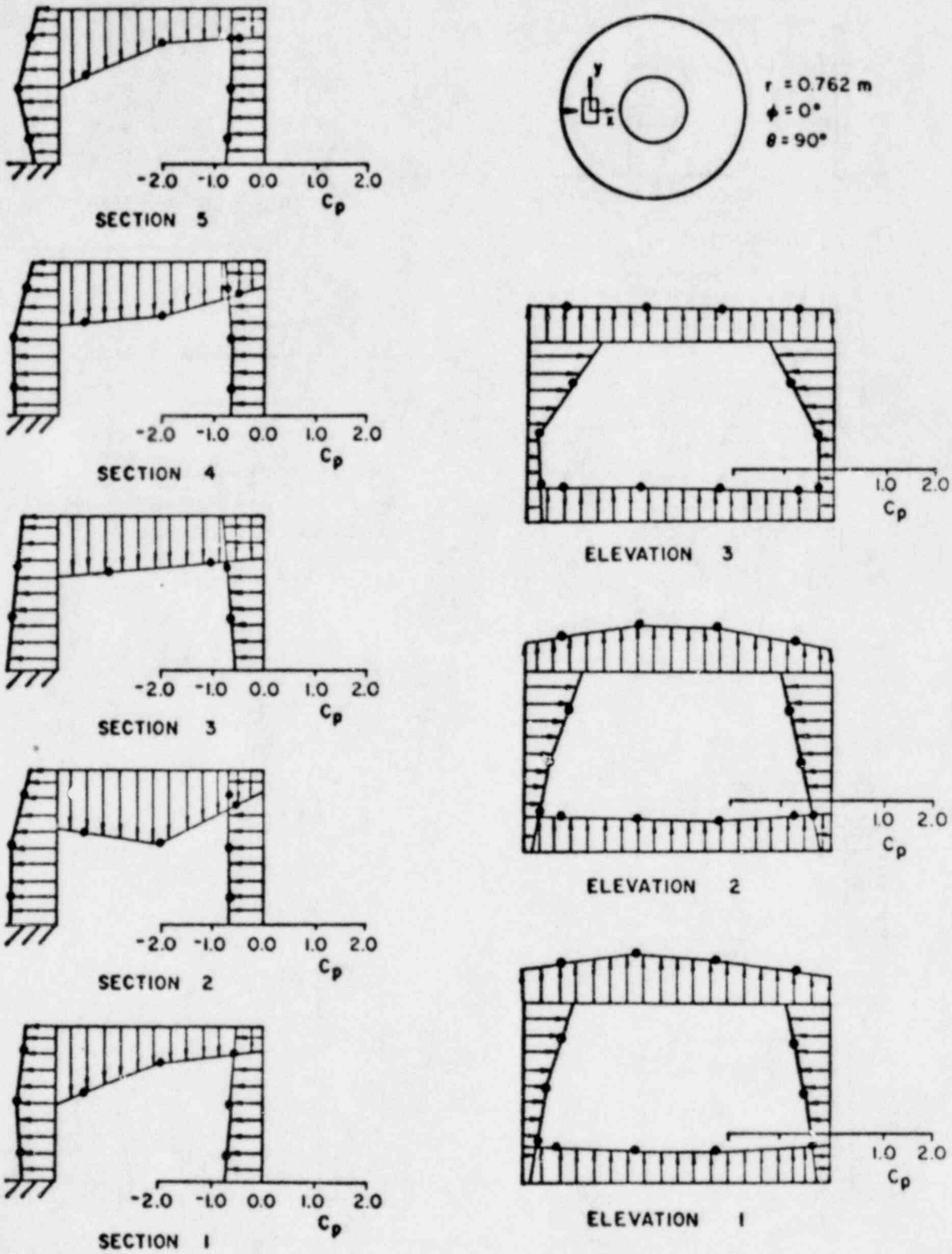

Figure 17c. Surface pressure coefficient on the rectangular model in the convergent zone (r = 0.762m) with imposed swirl angle of 0^0 (Case 3, orientation angle of 90^0).

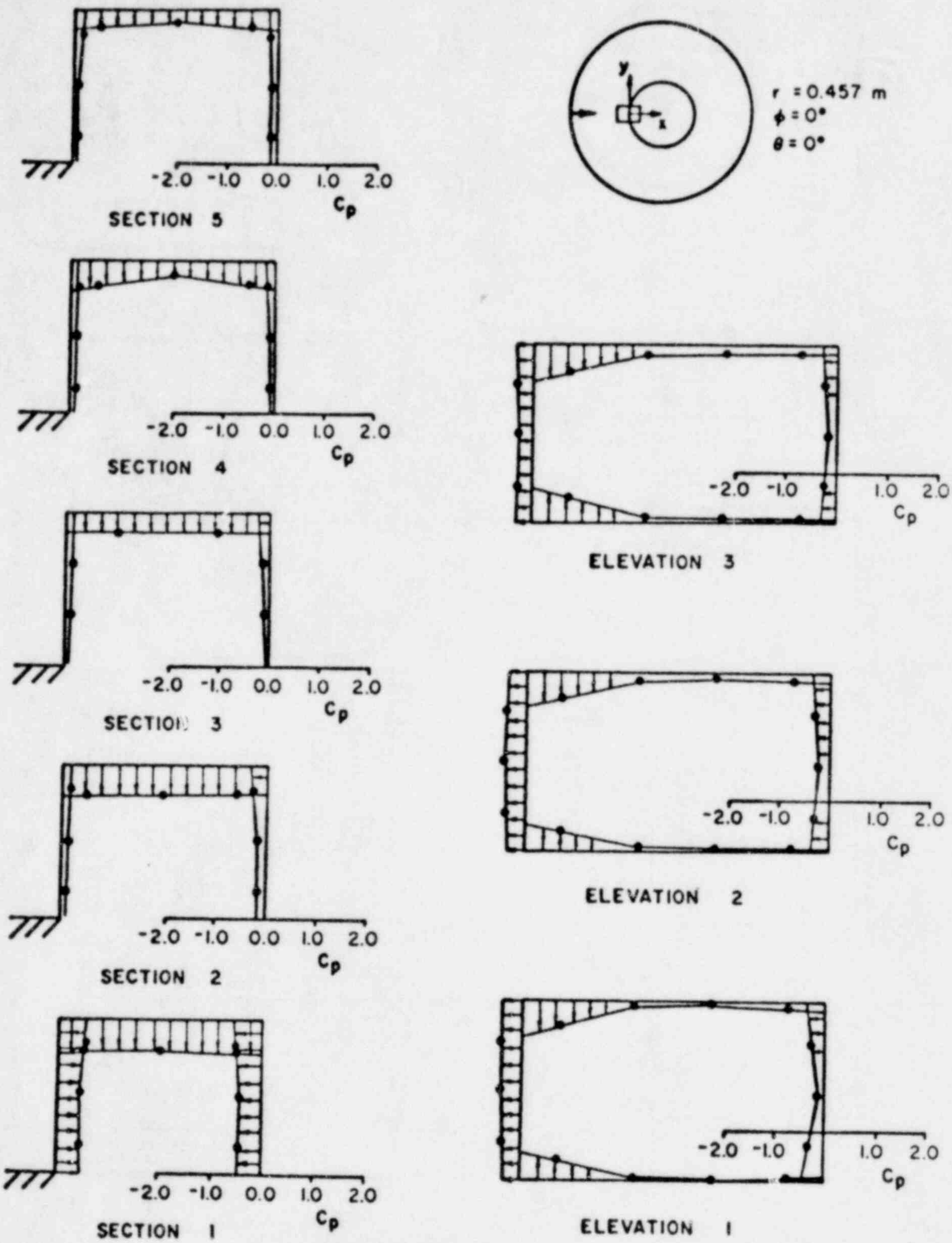

Figure 18a. Surface pressure coefficient on the rectangular model at the boundary of the convergent and convection zones (r = 0.457m) with imposed swirl angle of 0^0 (Case 4, orientation angle of 0^0).

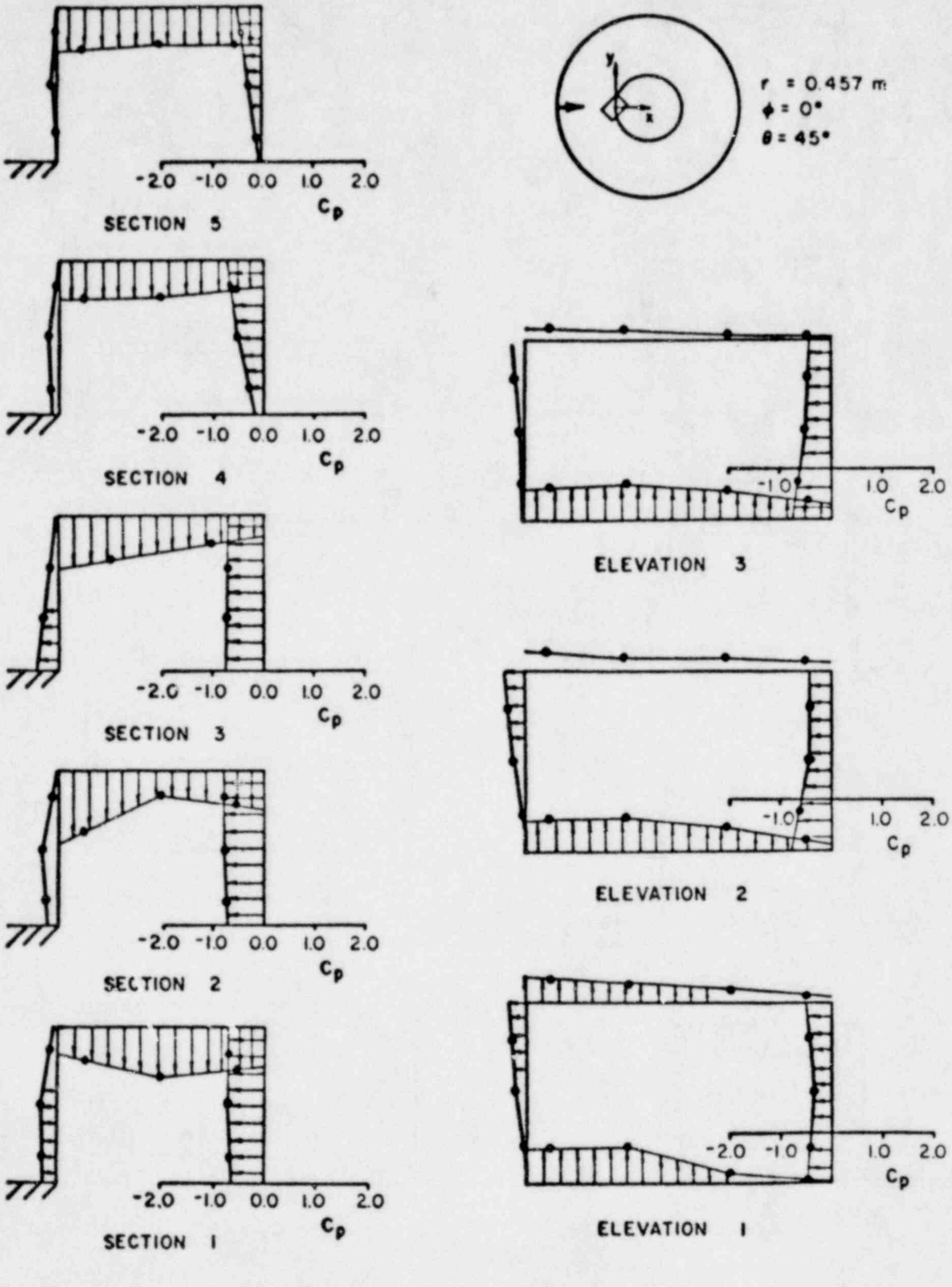

Figure 18b. Surface pressure coefficient on the rectangular model at the boundary of the convergent and convection zones (r = 0.457m) with imposed swirl angle of 0^0 (Case 5, orientation angle of 45^0).

1746 106

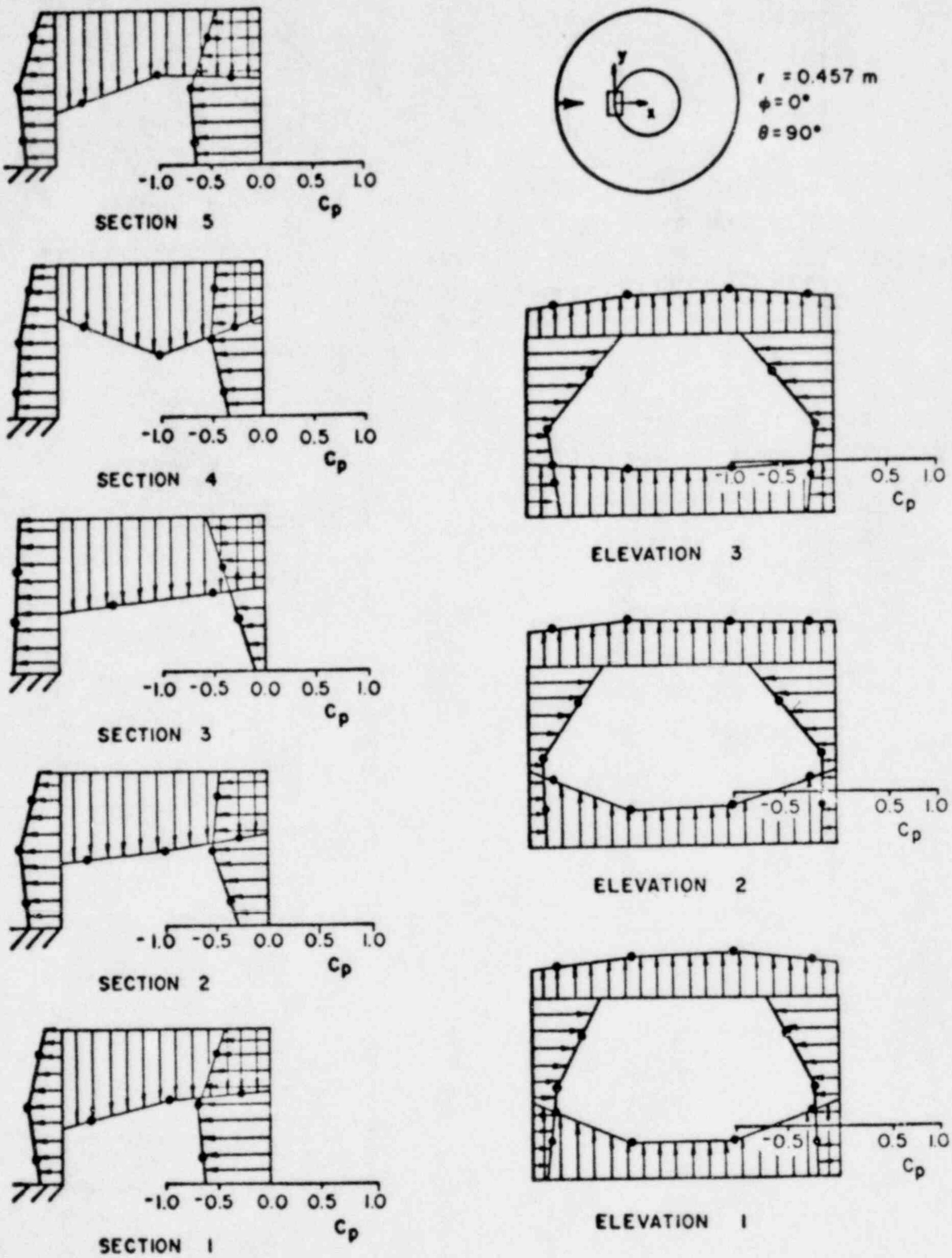

Figure 18c. Surface pressure coefficient on the rectangular model at the boundary of the convergent and convection zones (r = 0.457m) with imposed swirl angle of 0^0 (Case 6, orientation angle of 90^0).

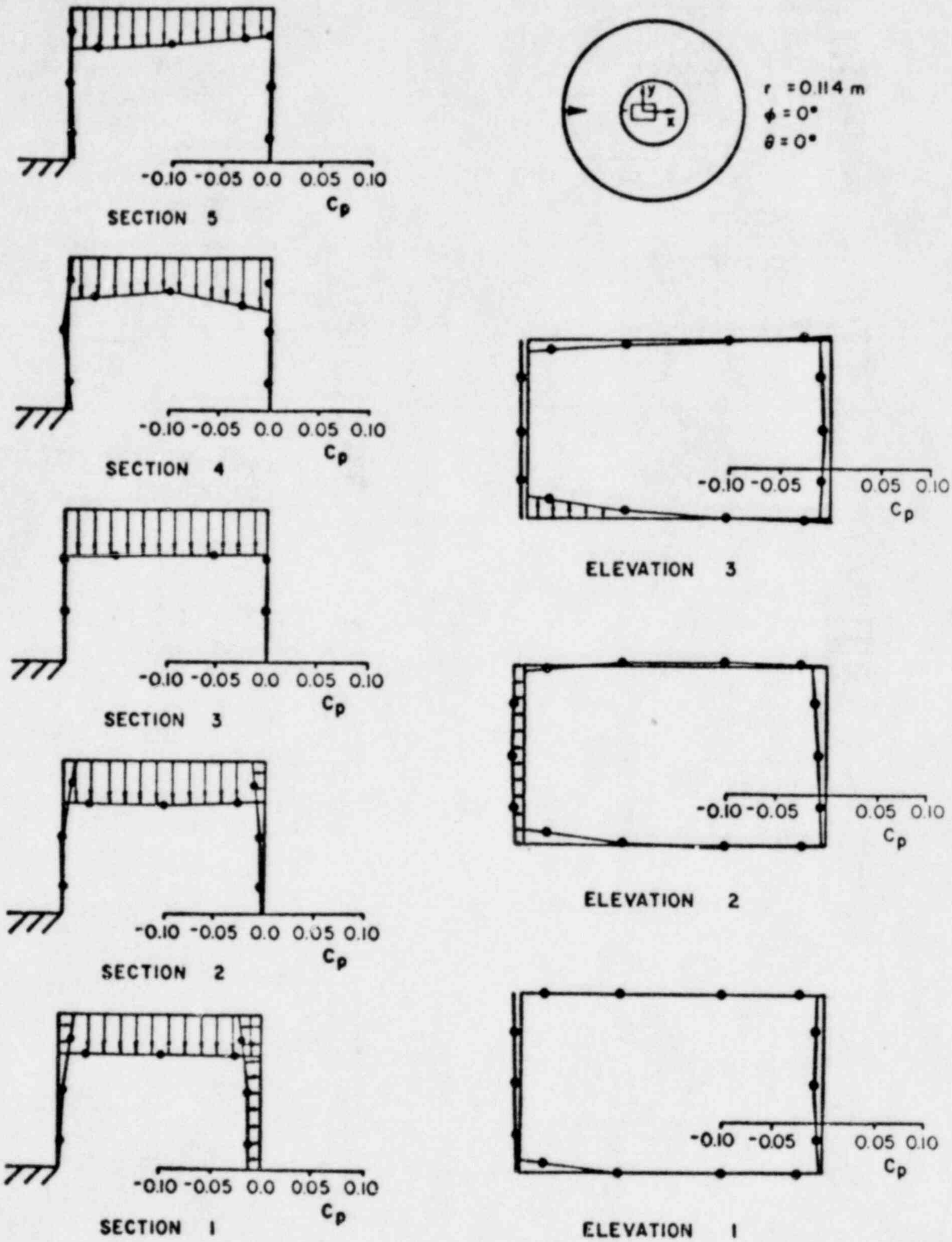

Figure 19a. Surface pressure coefficient on the rectangular model in the convection zone (r = 0.114m) with imposed swirl angle of 0^0 (Case 7, orientation angle of 0^0).

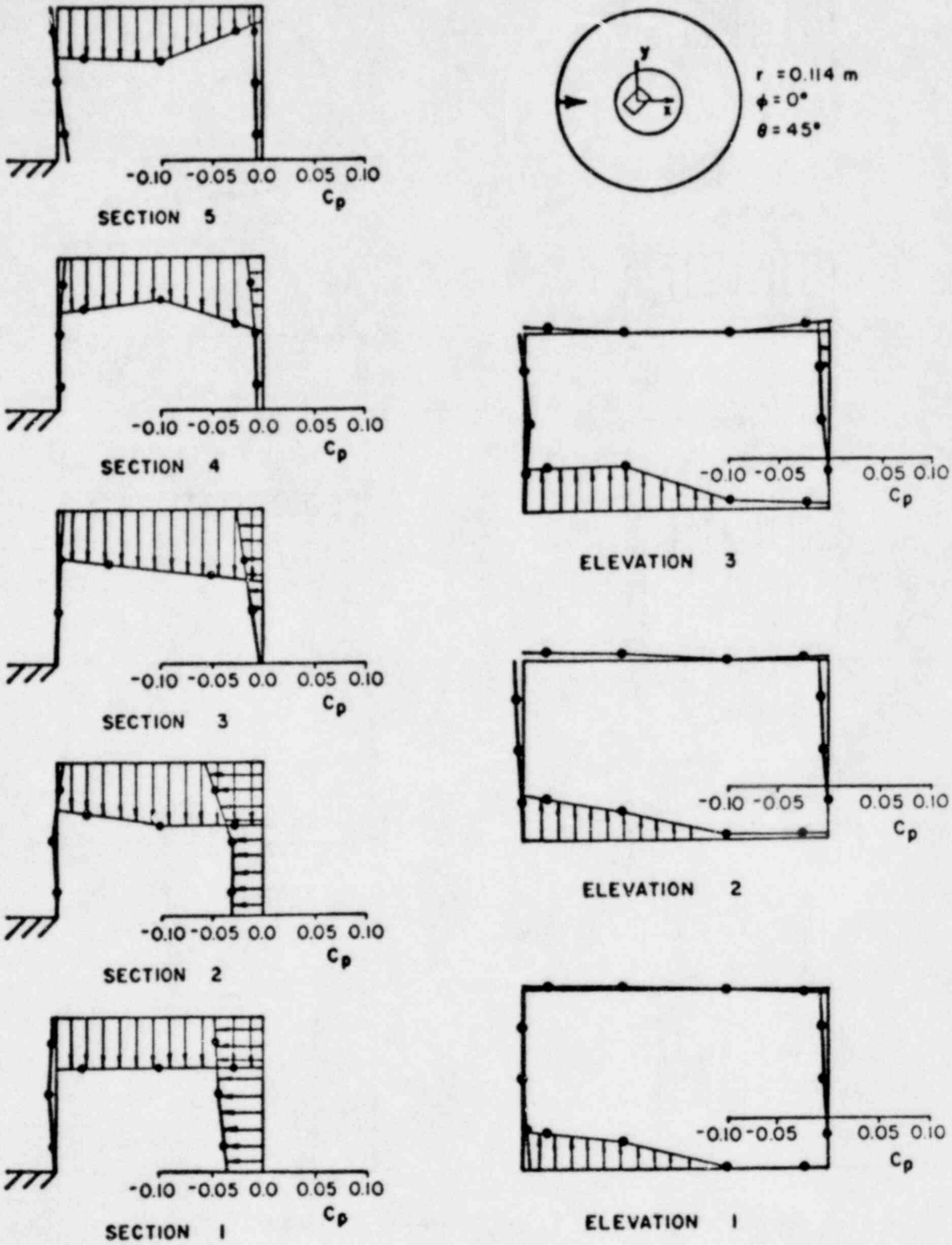

Figure 19b. Surface pressure coefficient on the rectangular model in the convection zone ($r = 0.114m$) with imposed swirl angle of 0^0 (Case 8, orientation angle of 45^0).

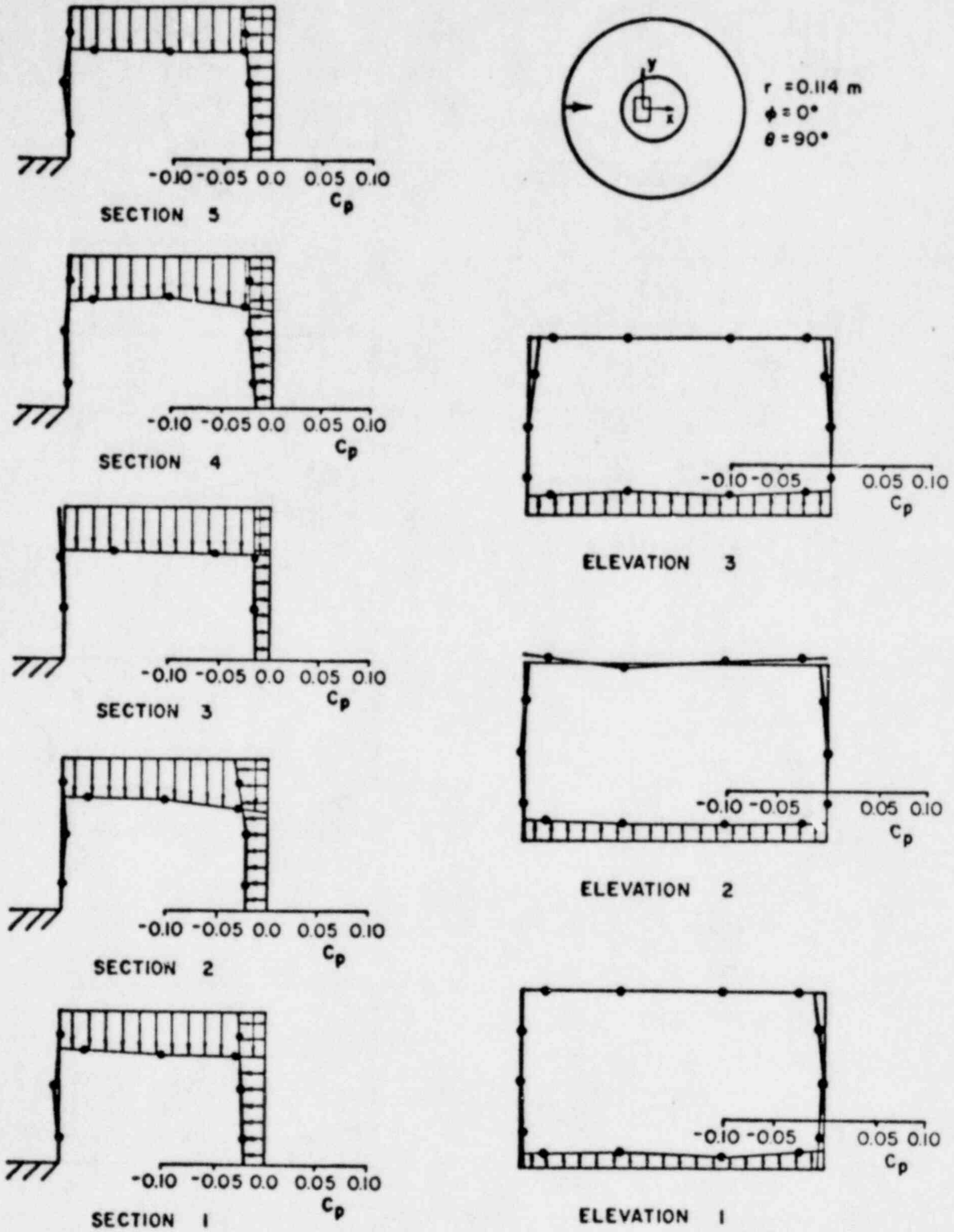

Figure 19c. Surface pressure coefficient on the rectangular model in the convection zone (r = 0.114m) with imposed swirl angle of 0^0 (Case 9, orientation angle of 90^0).

1746 110

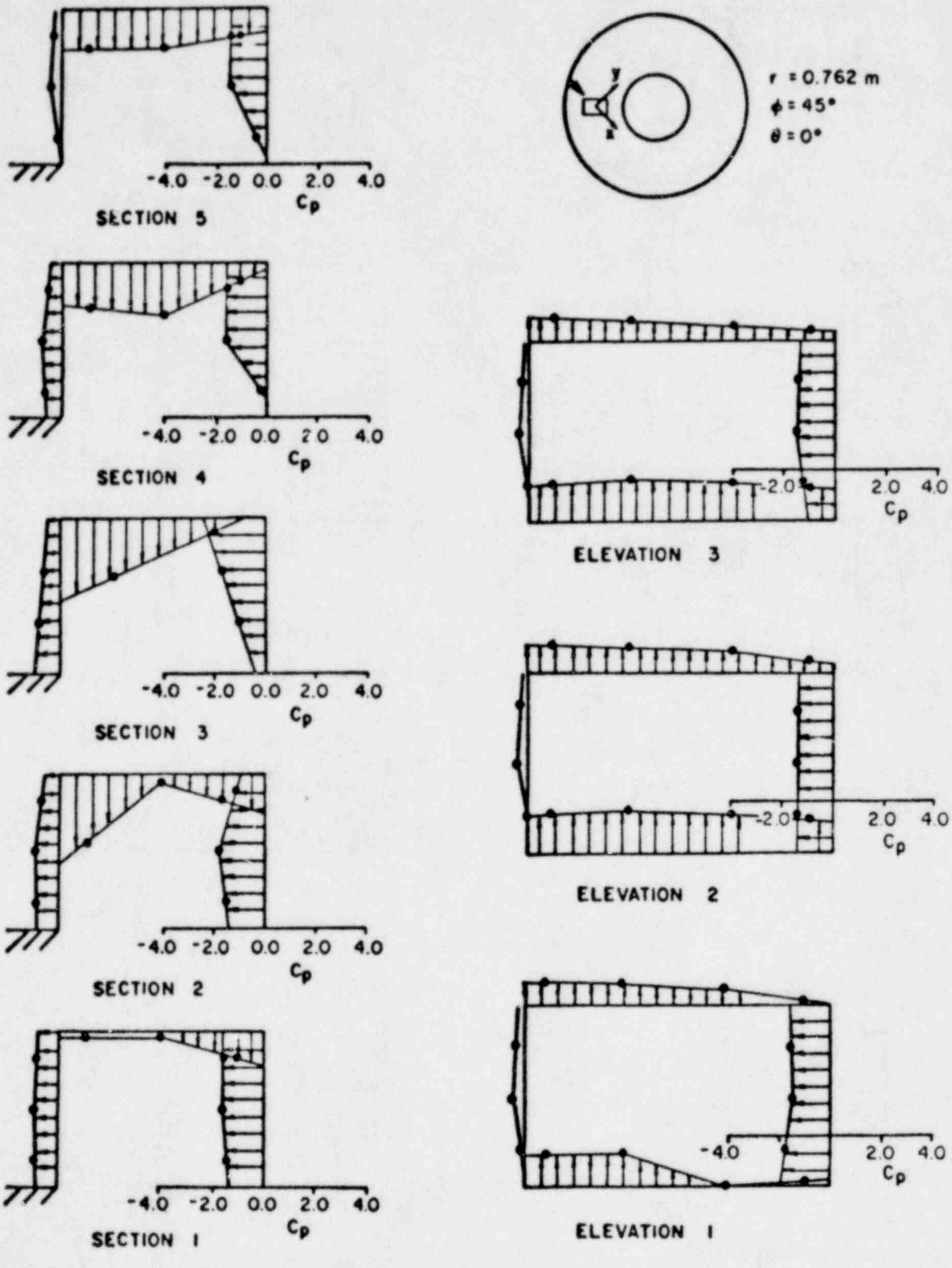

Figure 20a. Surface pressure coefficient on the rectangular model in the convergent zone (r = 0.762m) with imposed swirl angle of 45^0 (Case 10, orientation angle of 0^0).

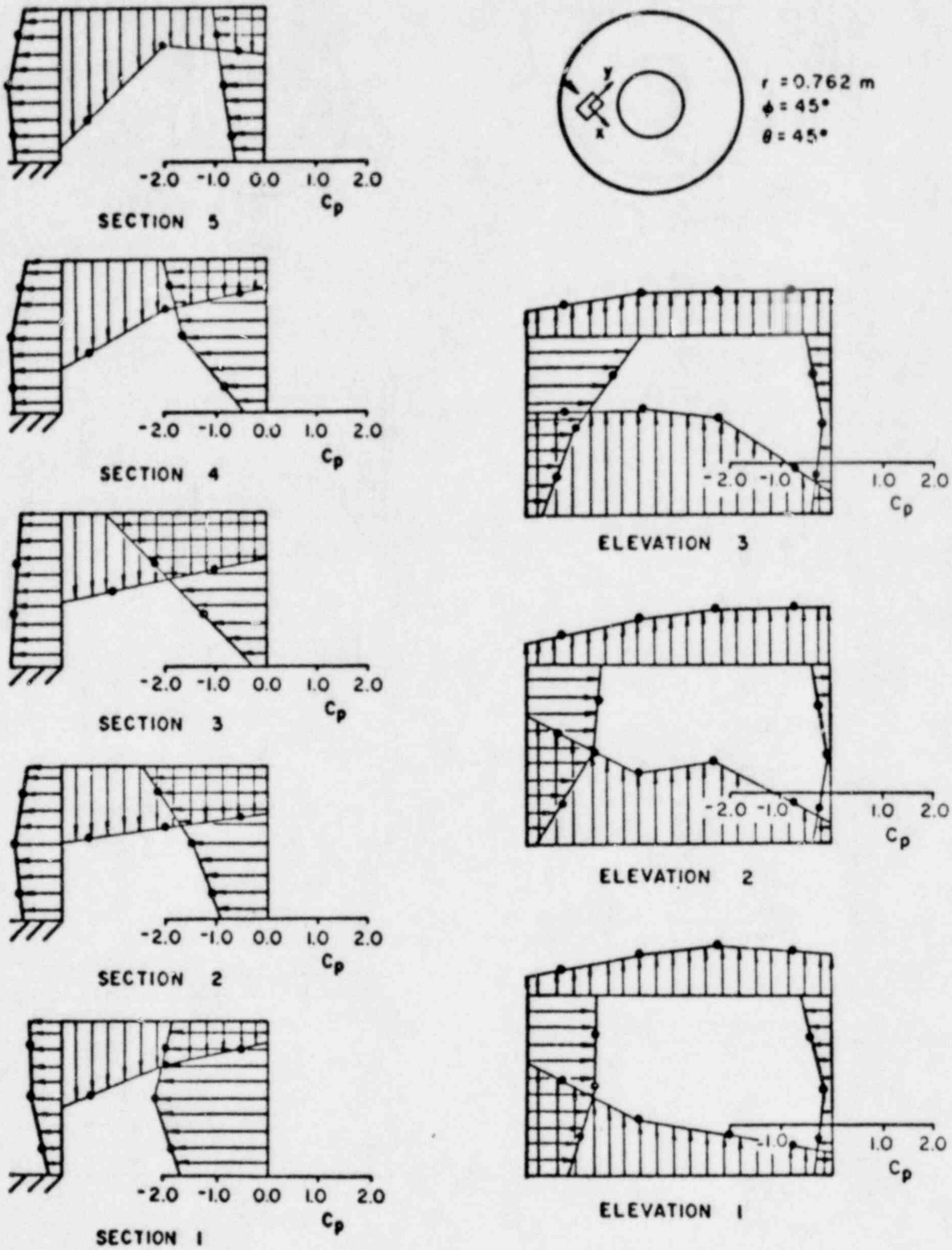

Figure 20b. Surface pressure coefficient on the rectangular model in the convergent zone (r = 0.762m) with imposed swirl angle of 45^0 (Case 11, orientation angle of 45^0).

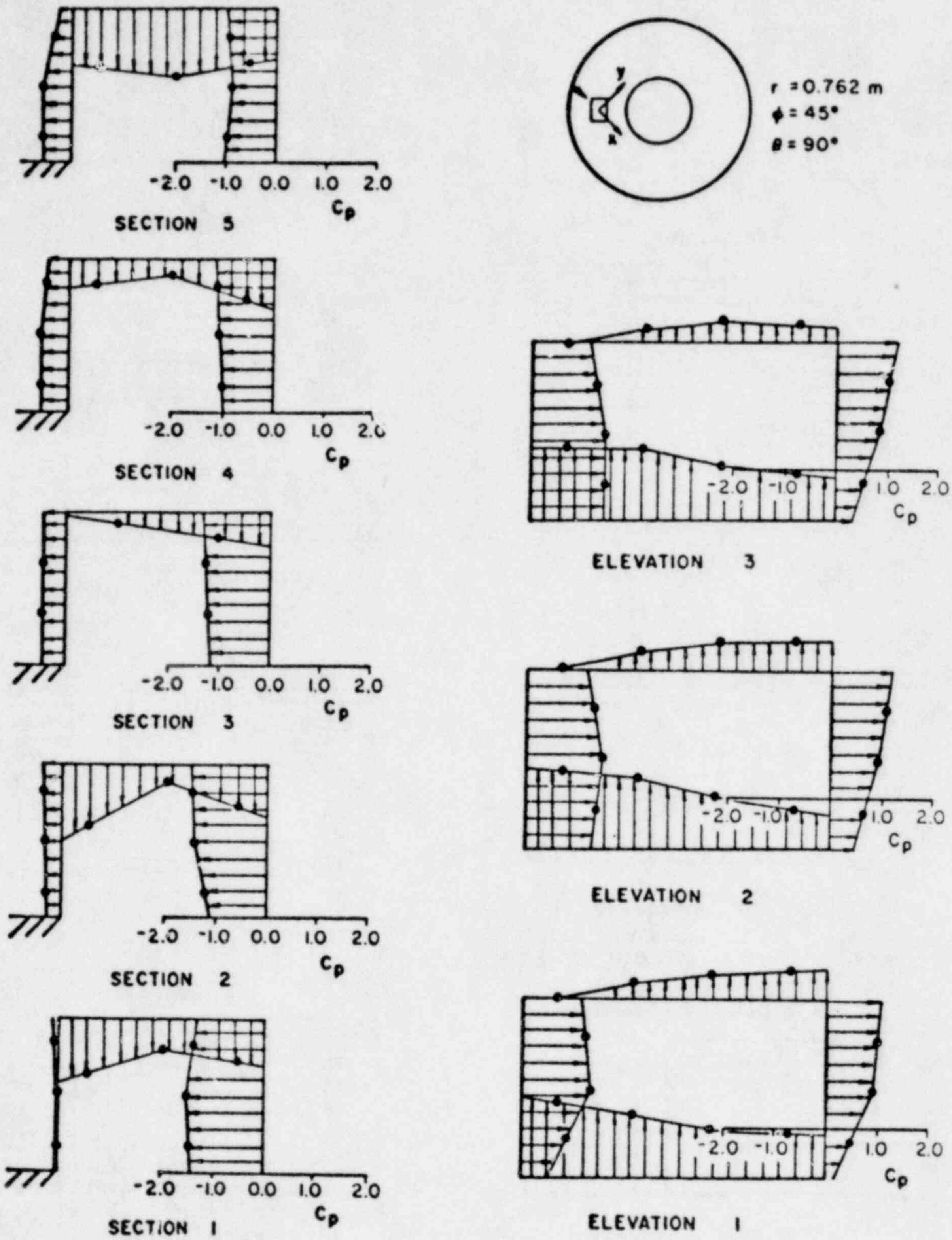

Figure 20c. Surface pressure coefficient on the rectangular model in the convergent zone (r = 0.762m) with imposed swirl angle of 45^0 (Case 12, orientation angle of 90^0).

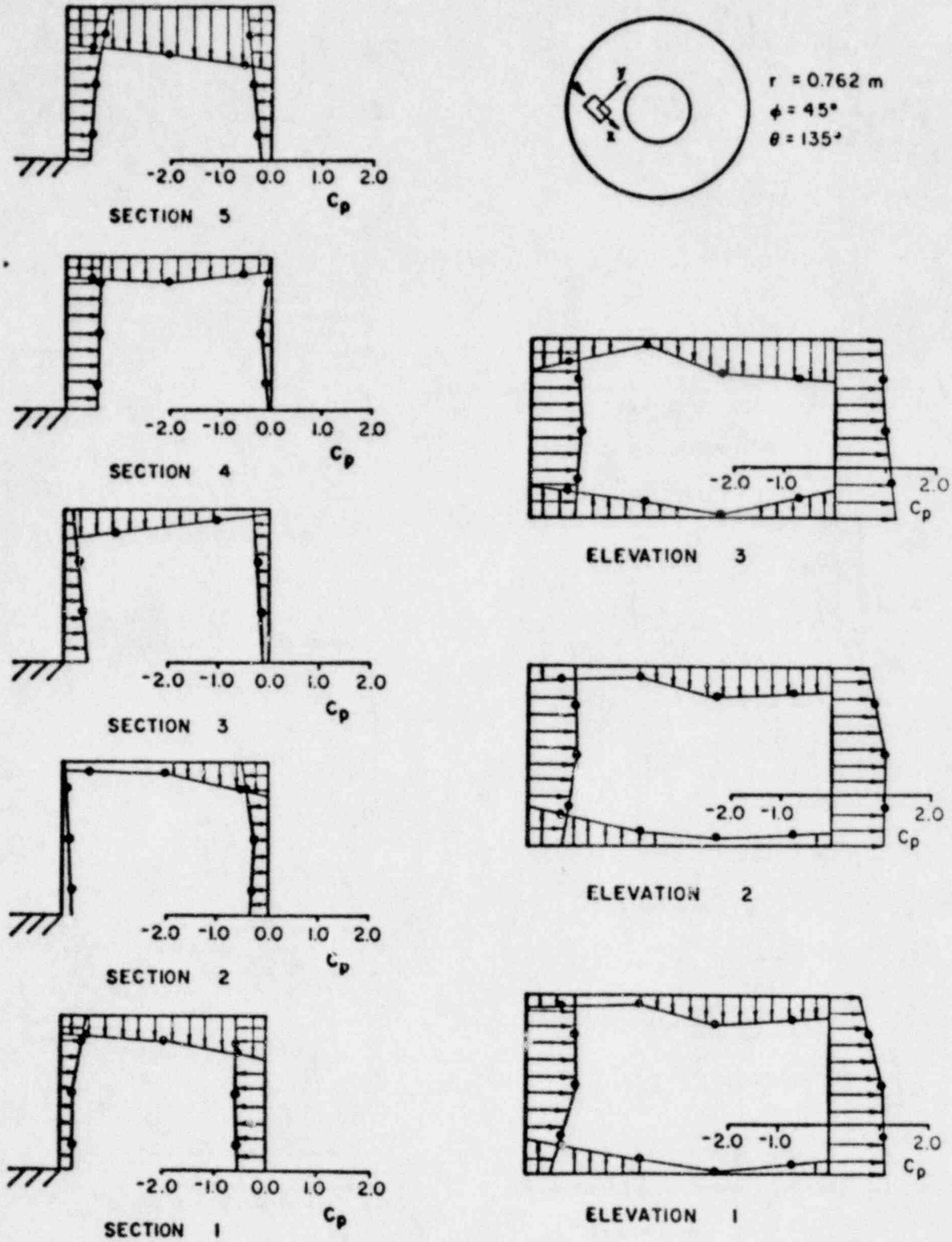

Figure 20d. Surface pressure coefficient on the rectangular model in the convergent zone ($r = 0.762$m) with imposed swirl angle of 45^0 (Case 13, orientation angle of 135^0).

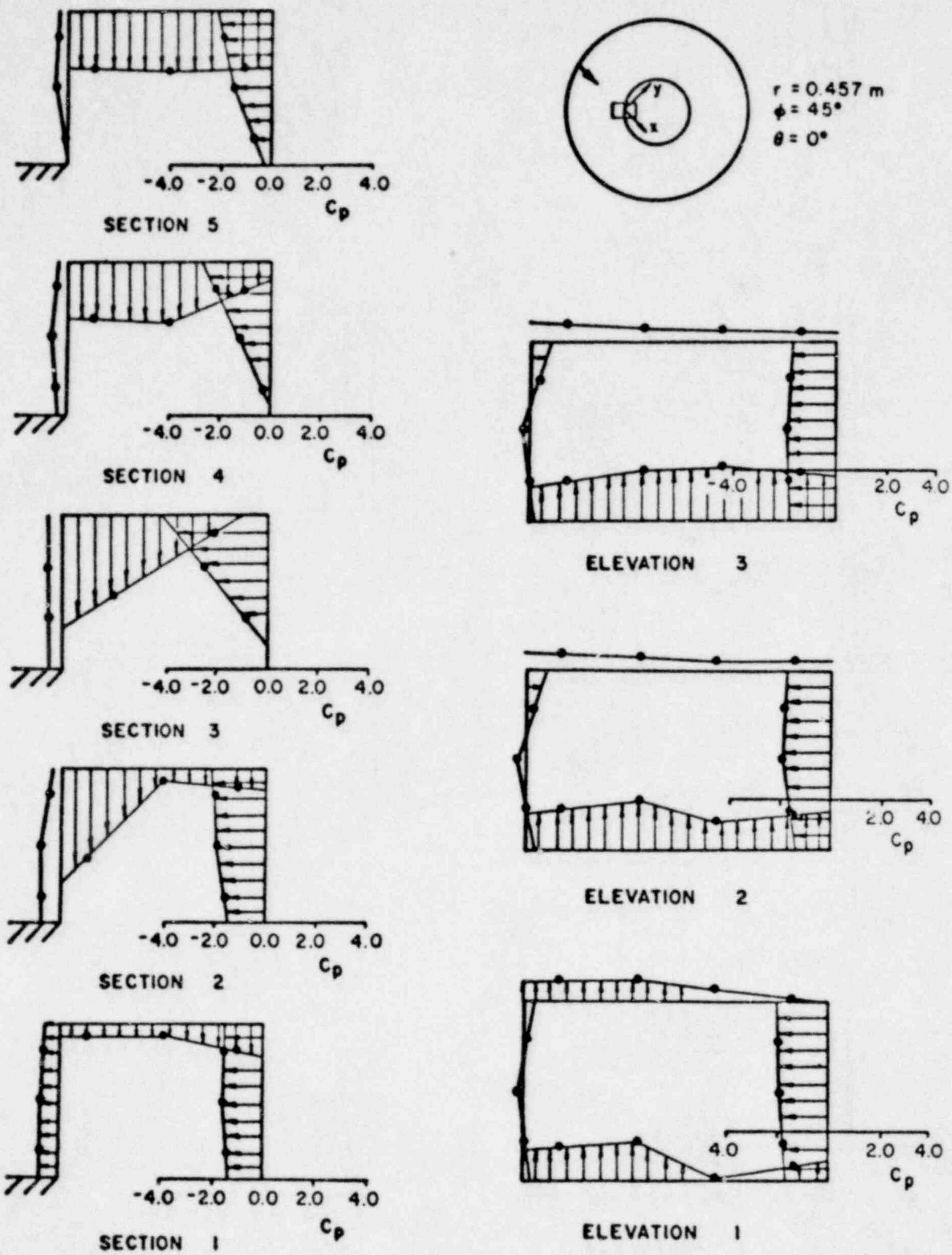

Figure 21a. Surface pressure coefficient on the rectangular model at the boundary of the convergent and convection zones (r = 0.457m) with imposed swirl angle of 45^0 (Case 14, orientation angle of 0^0).

1746 115

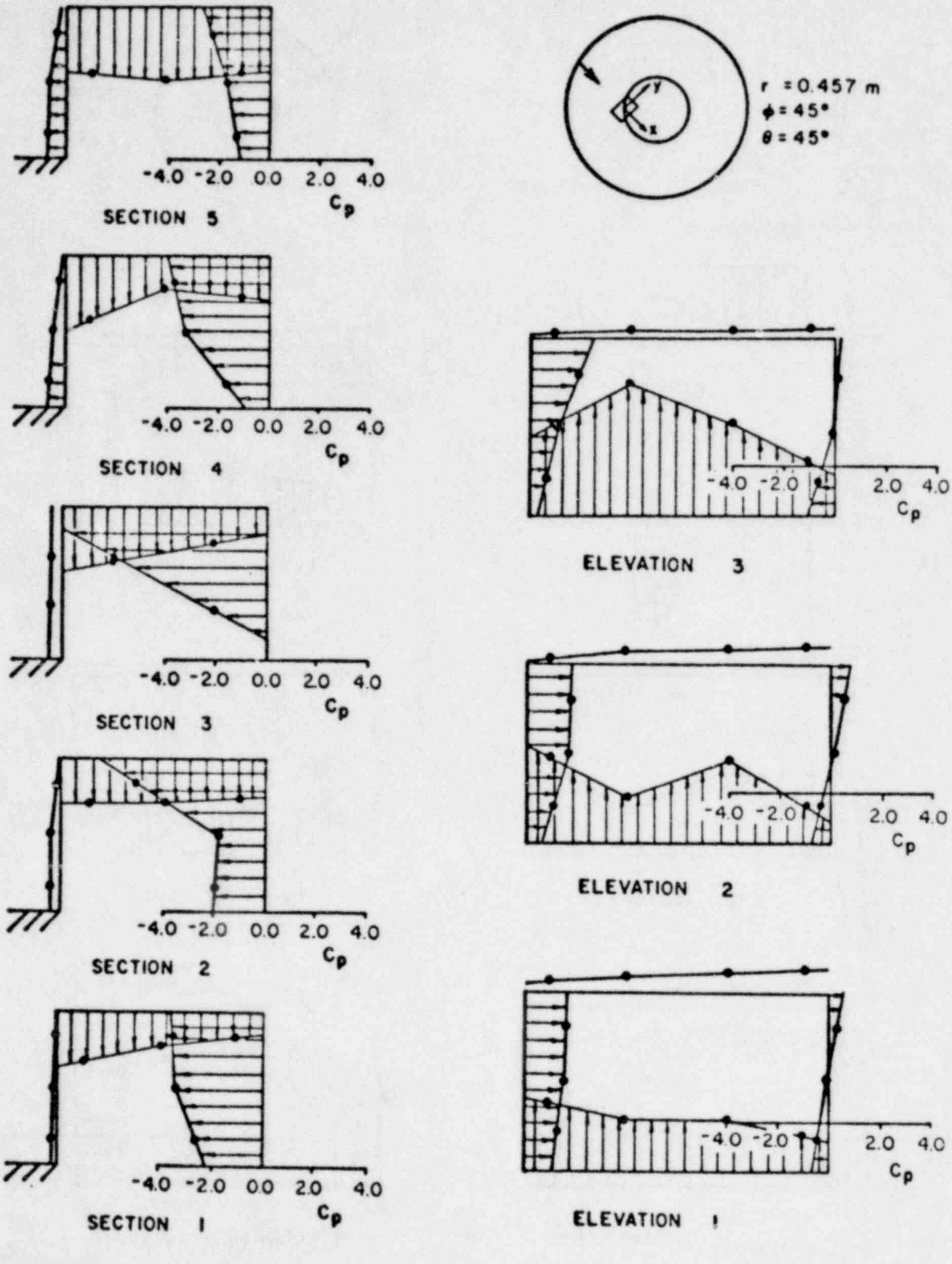

Figure 21b. Surface pressure coefficient on the rectangular model at the boundary of the convergent and convection zones (r = 0.457m) with imposed swirl angle of 45^0 (Case 15, orientation angle of 45^0).

1746 116

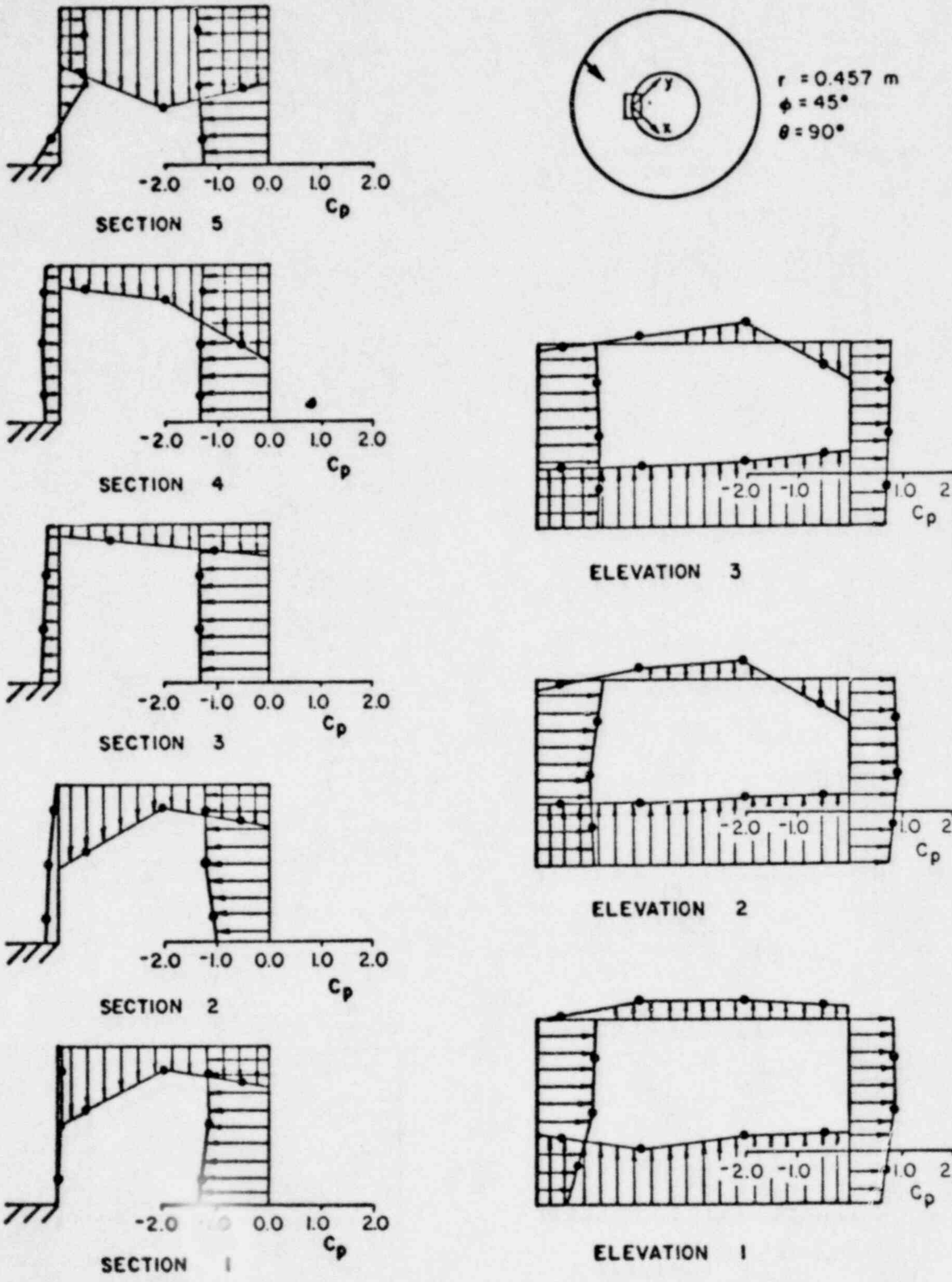

Figure 21c. Surface pressure coefficient on the rectangular model at the boundary of the convergent and convection zones (r = 0.457m) with imposed swirl angle of 45^0 (Case 16, orientation angle of 90^0).

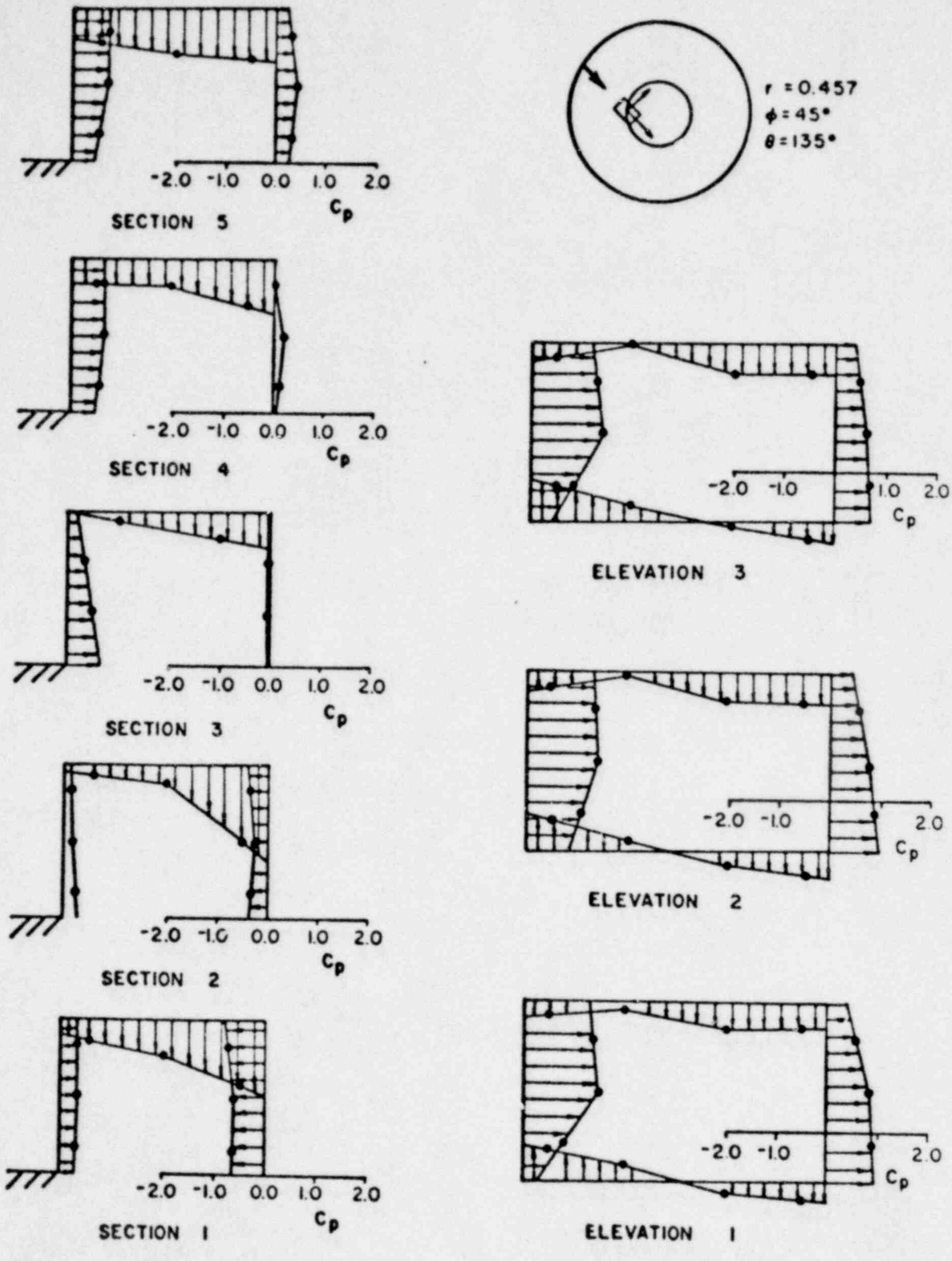

Figure 21d. Surface pressure coefficient on the rectangular model at the boundary of the convergent and convection zones (r = 0.457m) with imposed swirl angle of 45^0 (Case 17, orientation angle of 135^0).

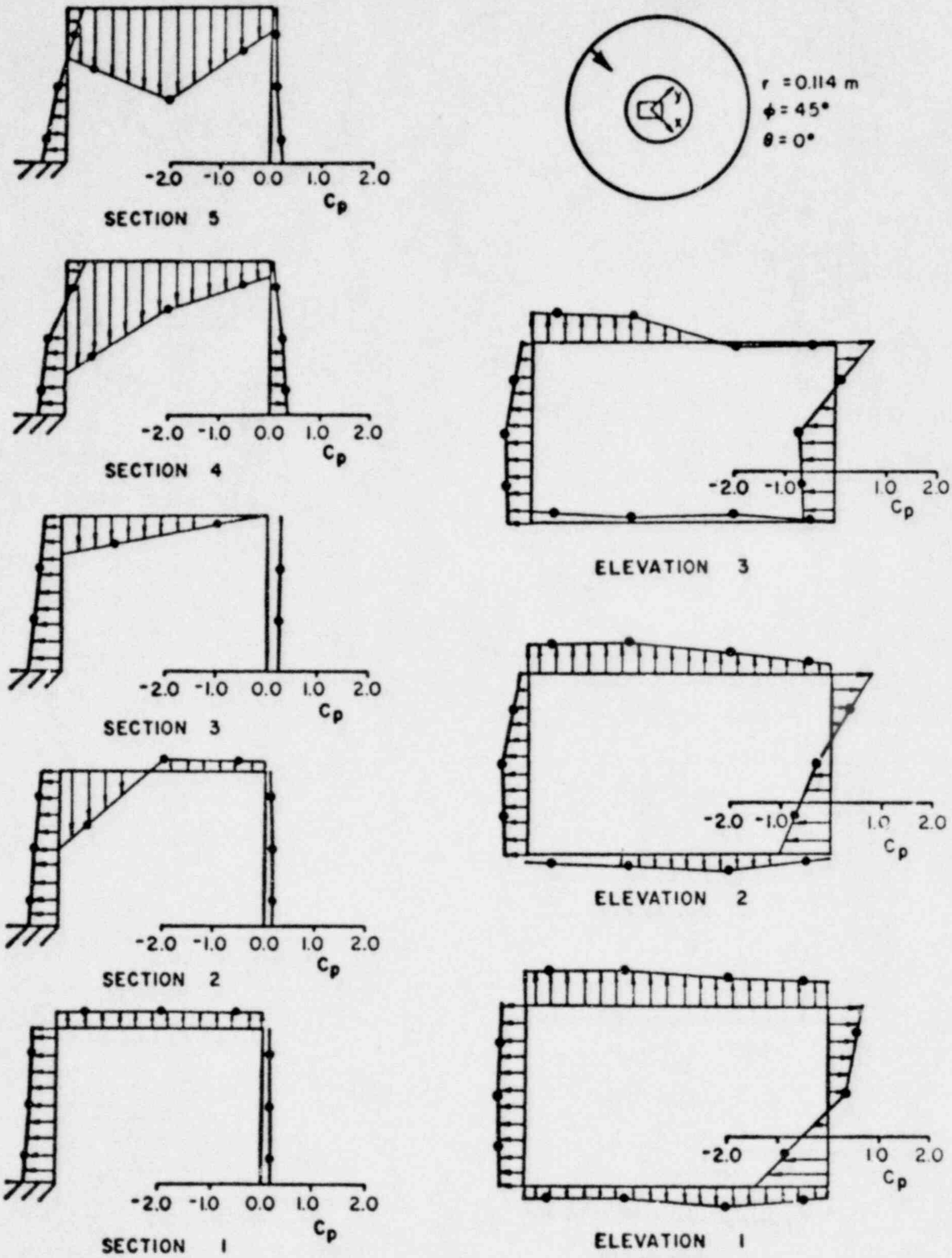

Figure 22a. Surface pressure coefficient on the rectangular model in the convection zone (r = 0.114m) with imposed swirl angle of 45^0 (Case 18, orientation angle of 0^0).

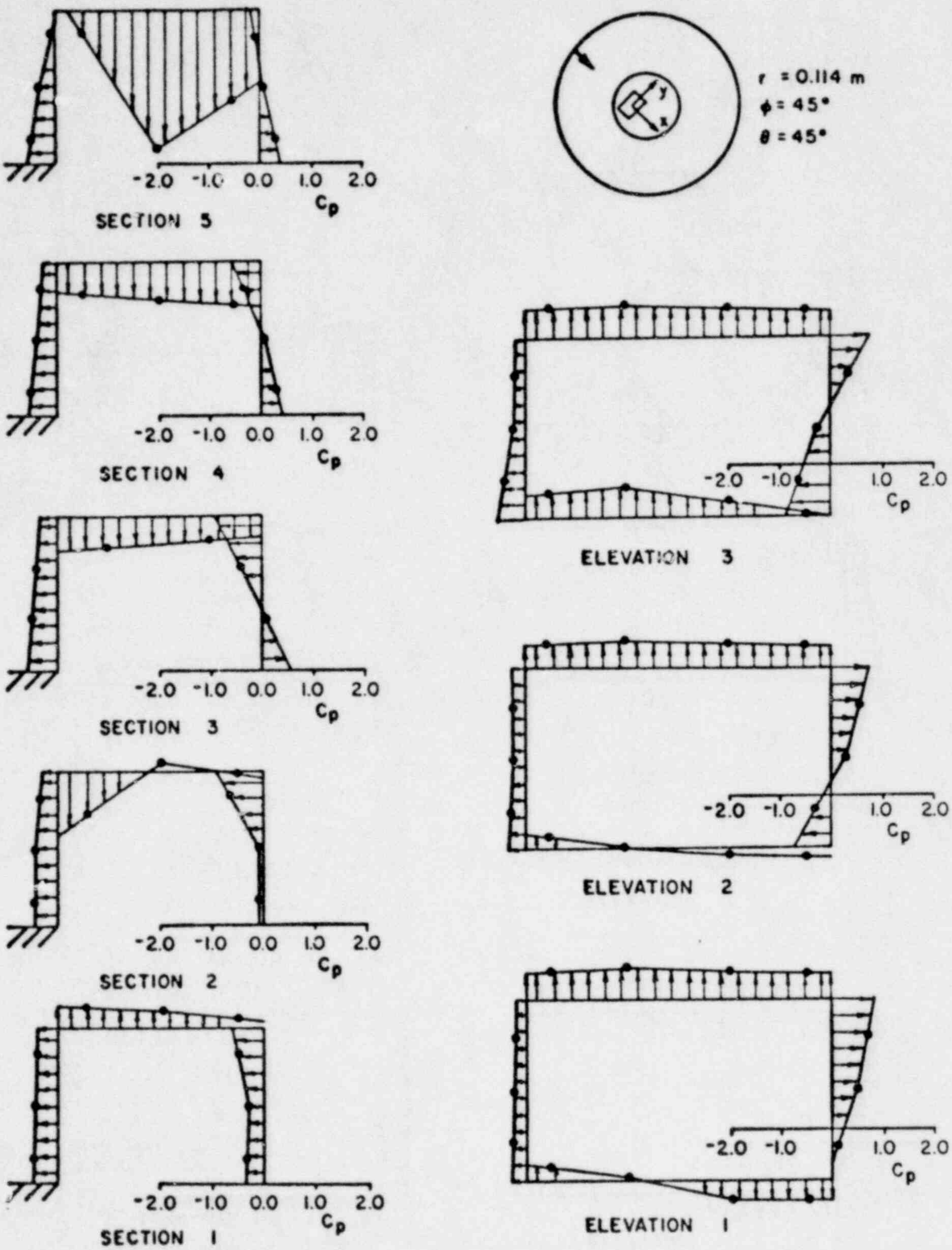

Figure 22b. Surface pressure coefficient on the rectangular model in the convection zone (r = 0.114m) with imposed swirl angle of 45^0 (Case 19, orientation angle of 45^0).

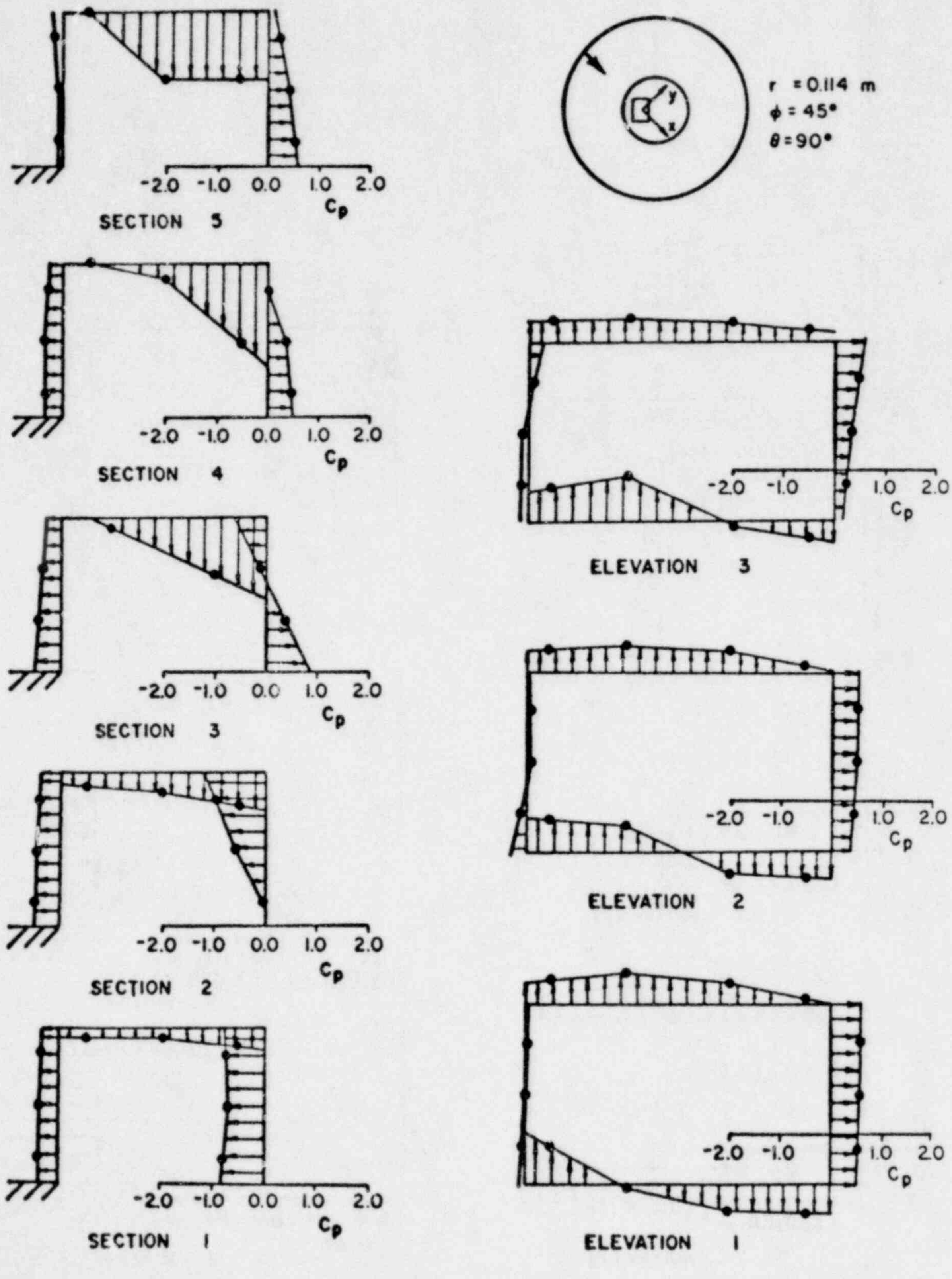

Figure 22c. Surface pressure coefficient on the rectangular model in the convection zone (r = 0.114m) with imposed swirl angle of 45^0 (Case 20, orientation angle of 90^0).

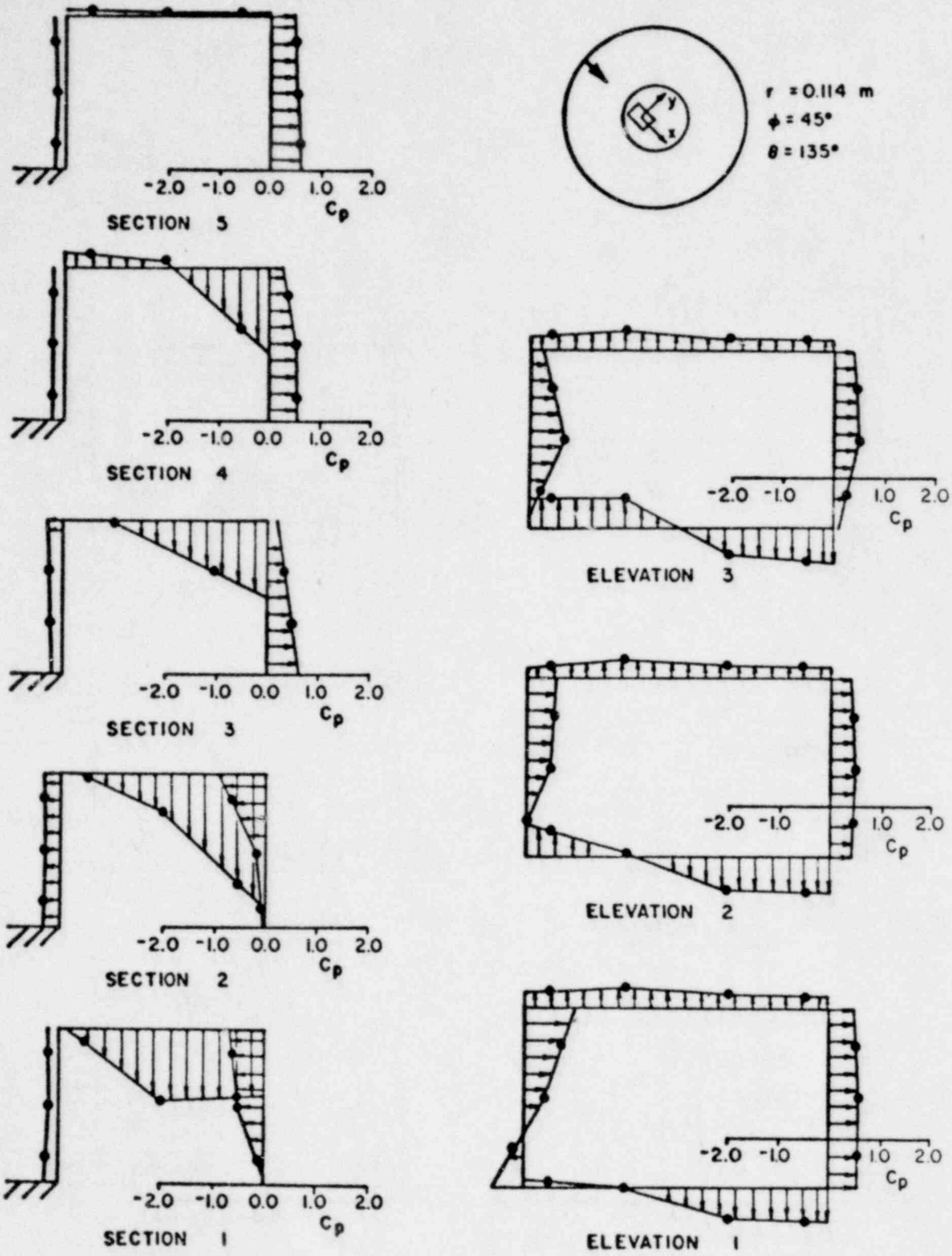

Figure 22d. Surface pressure coefficient on the rectangular model in the convection zone (r = 0.114m) with imposed swirl angle of 45^0 (Case 21, orientation angle of 135^0).

1746 121

CHAPTER VI

CONCLUDING REMARKS

These measurements indicate that the swirling winds induced by a tornado vortex can change the forces and moments experienced by both cylindrical and rectangular structures when compared with ordinary boundary-layer-type wind loads. The effects are most dramatic for the rectangular structure. In the case of the cylindrical model, the vortical tornadic flow induces a side force on the model and increases the vertical force on the model. The change in the horizontal force coefficient, however, is small. If the model is tangent to the edge of the undisturbed vortex, vortex attachment occurs, the pressure distribution becomes more symmetric and the pressure coefficient becomes large and negative. This suggests a change in the failure mode from a "blown-over" mode to a "bursting" mode as the distance possible between the model and vortex decreases.

The critical location of the rectangular structure in the tornadic flow appears to be at the boundary between the convergent and convection zones where the imposed updraft alters the flow about the structure in a fashion so as to increase the forces and moments significantly. The origins of these increases appear to lie in the interaction of the flow about the building with the vorticity created at the sharp corners of the structure. The resulting vortex intensification due to vortex stretching lowers the local pressure creating large suction forces. Thus, not only must one design structures for the total force due to tornadic winds, but one must ensure that the structure can withstand the large local forces measured in these experiments. If this is not the case, it then becomes possible for a structure to first fail locally with, for example, a corner of a roof lifting off after which the changing geometry of the structure allows a large scale failure to occur. The failure sequence suggested by this example has, in fact, been observed in naturally occurring tornadoes.

REFERENCES

1. Kim, S.I. and Mehta, K.C., "Full Scale Measurements on a Flat Roof Area", Proceedings Fifth International Conference on Wind Engineering, Fort Collins, Colorado, 1979.

2. Dalgliesh, W.A., Templin, J.T., and Cooper, K.R., "Comparison of Wind Tunnel and Full-Scale Building Surface Pressures with Emphasis on Peaks", Proceedings Fifth International Conference on Wind Engineering, Fort Collins, Colorado, 1979.

3. Cermak, J.E., "Laboratory Simulation of the Atmospheric Boundary Layer", J. American Institute of Aeronautics and Astronautics, Vol. 9, pp. 1746-54, 1971.

4. Whitbread, R.E., "Model Simulation of Wind Effects on Structures", Proceedings Conference on Wind Effects on Structures, Teddington, England, 1963.

5. Golden, J.H., "An Assessment of Windspeeds in Tornadoes", Proceedings of the Symposium on Tornadoes, Lubbock, Texas, 1976.

6. Mehta, K.C., "Windspeed Estimates: Engineering Analysis", Proceedings of the Symposium on Tornadoes, Lubbock, Texas, 1976.

7. Hoecker, W.H., "Windspeed and Airflow Patterns in the Dallas Tornado of April 2, 1957", Monthly Weather Review, Vol. 88, pp. 167-180, 1960.

8. Hoecker, W.H., "Three-Dimensional Pressure Pattern of the Dallas Tornado and Some Resultant Implications", Monthly Weather Review, Vol. 89, pp. 533-542, 1961.

9. Golden, J.H., and Purcell, D., "Photogrammetric Velocities for the Great Bend, Kansas Tornado: Accelerations and Asymmetries", Ninth Conference on Severe Local Storms, Norman, Oklahoma, 1975.

10. Dinwiddie, F.C., "Waterspout-Tornado Structure and Behavior at Nags Head, N.C., August 12, 1952", Monthly Weather Review, pp. 239-250, 1959.

11. Brown, R.A. (editor), "The Union City, Oklahoma Tornado of 24 May, 1973", NOAA Technical Memorandum ERL NSSL-80, December, 1976.

12. Ward, N.B., "The Exploration of Certain Features of Tornado Dynamics Using a Laboratory Model", J. Atmospheric Sciences, Vol. 29, pp. 1194-1204, 1972.

13. Turner, J.S., and Lilly, D.K., "The Carbonated Water Tornado Vortex", J. Atmospheric Science, Vol. 20, pp. 468-471, 1963.

14. Chang, C.C., "Tornado Wind Effects on Buildings and Structures with Laboratory Simulation", Third International Conference on Wind Effects on Buildings and Structures, Tokyo, Japan, 1971.

15. Mehta , K.C., Minor, J.E., and McDonald, J.R., "The Tornadoes of April 3,4, 1974: Windpseed Analyses", ASCE National Structural Engineering Conference, New Orleans, Louisiana, 1975.

16. McDonald, J.R., "The Hereford Tornado of April 19, 1971", Institute of Disaster Research Report, Texas Tech University, Lubbock, Texas, 1971.

17. Davies-Jones, R.P. and Kessler, E., "Tornadoes"in Weather and Climate Modification, Chapter 16, W.N. Hess (ed.), Wiley and Sons, New York, 1974.

18. Pearson, A., "Tornado Prediction", Proceedings of the Symposium on Tornadoes, Lubbock, Texas, 1976.

19. Schaefer, J.T., Kelly, D.L., and Abbery, R.F. Jr., "Tornado Track Characteristics and Hazard Probabilities", Proceedings Fifth International Conference on Wind Engineering, Fort Collins, Colorado, 1979.

20. Goldman, J.L., "The Illinois Tornadoes of 17 and 22 April 1963", SMRP Research Paper No. 39, University of Chicago, Chicago, Illinois, 1965.

21. Jischke, M.C. and Parang M., "Properties of Simulated Tornado-Like Vortices", J. Atmospheric Sciences, Vol. 31, pp. 506-512, 1974.

22. Church, C.K., Snow, J.T., and Agee, E.M., "Tornado Vortex Simulation at Purdue University", Bulletin of the American Meteorological Society, Vol. 58, pp. 900-908, 1977.

23. Jischke, M.C. and Parang, M., "Fluid Dynamics of a Tornado-Like Vortex Flow", University of Oklahoma AMNE Report, 1975.

24. Davies-Jones, R.P., "The Dependence of Core Radius on Swirl Ration in a Tornado Simulator", J. Atmospheric Sciences, Vol. 30, pp. 1427-1430, 1973.

25. Cermak, J.E., "Aerodynamics of Buildings", Annual Reviews of Fluid Mechanics, Vol. 8, pp. 75-106, 1976.

26. Cockrell, D.J. and Lee, B.E., "Production of Shear Profiles in a Wind Tunnel by Cylindrical Rods Placed Normal to the Stream", J. Royal Aeronautical Society, Vol. 80, pp. 724-725, 1966.

27. Sachs, P., Wind Forces in Engineering, Pergamon Press, 1978.

NRC FORM 335 (7-77) U.S. NUCLEAR REGULATORY COMMISSION **BIBLIOGRAPHIC DATA SHEET**	1. REPORT NUMBER (Assigned by DDC) NUREG/CR-1183
4. TITLE AND SUBTITLE (Add Volume No., if appropriate) Laboratory Simulation of Steady Tornadic Wind Loads on Structures	2. (Leave blank)
	3. RECIPIENT'S ACCESSION NO.
7. AUTHOR(S) Martin C. Jischke and Bruce D. Light	5. DATE REPORT COMPLETED MONTH November YEAR 1979
9. PERFORMING ORGANIZATION NAME AND MAILING ADDRESS (Include Zip Code) School of Aerospace, Mechanical and Nuclear Engineering University of Oklahoma Norman, Oklahoma 73019	DATE REPORT ISSUED MONTH December YEAR 1979
	6. (Leave blank)
	8. (Leave blank)
12. SPONSORING ORGANIZATION NAME AND MAILING ADDRESS (Include Zip Code) Site Safety Research Branch Division of Reactor Safety Research Office of Nuclear Regulatory Research U.S. Nuclear Regulatory Commission Washington, D.C. 20555	10. PROJECT/TASK/WORK UNIT NO. FIN B6241
	11. CONTRACT NO. NRC-04-78-207
13. TYPE OF REPORT topical report	PERIOD COVERED (Inclusive dates) November 1977 - October 1979
15. SUPPLEMENTARY NOTES	14. (Leave blank)

16. ABSTRACT (200 words or less)

Utilizing the University of Oklahoma modified tornado simulator, the interaction of tornadic flowfields with structures has been examined empirically. Measurements with and without swirl have been made of the pressure on the surface of a cyclindrical model and a rectangular model placed in the simulator. Results are presented for the surface pressure coefficient and the total force moments coefficients for imposed swirl angles of 0° and 45°, with the models placed at three locations within the simulator: 1) the convergent zone, 2) the boundary of the convergent zone and convection zone, 3) the convection zone. The measurements on the cyclindrical model show that in the swirling flow case, the nonuniform flow due to the tornado-like vortex induces a side-force, reckoned with respect to the local wind direction, that increases as the distance between the model and vortex decreases. The magnitude of both the force coefficients and overturning moment on the structure increase with swirl. The data for the rectangular model shows that the effects of the imposed swirl can be dramatic and important. Increases in the horizontal force coefficient and overturning moment coefficient by a factor of four over the zero swirl values can occur when the model is at the boundary of the convergent and convection zones. The vertical force on the roof can more than double. These results show that the tornadic windloads on structures cannot always be accurately estimated from the loads caused by boundary-layer-type winds.

17. KEY WORDS AND DOCUMENT ANALYSIS

17a. DESCRIPTORS

17b. IDENTIFIERS/OPEN-ENDED TERMS

18. AVAILABILITY STATEMENT	19. SECURITY CLASS (This report)	21. NO. OF PAGES
	20. SECURITY CLASS (This page)	22. PRICE $

NRC FORM 335 (7-77)

1746 127

UNITED STATES
NUCLEAR REGULATORY COMMISSION
WASHINGTON, D. C. 20555

OFFICIAL BUSINESS
PENALTY FOR PRIVATE USE, $300

POSTAGE AND FEES PAID
U.S. NUCLEAR REGULATORY
COMMISSION

U.S. MAIL

POOR ORIGINAL

016

120555031837 2 ANRBR6
US NRC
SECY PUBLIC DOCUMENT ROOM
BRANCH CHIEF
HST LOBBY
WASHINGTON DC 20555

1746 128